

SC-RR-66-376

AEROSPACE
NUCLEAR
SAFETY

E2



SC-RR-66-376

July 1966

**DYNAMIC PENETRATION OF SELECTED
PROJECTILES INTO PARTICULATE
MEDIA**

L. J. Thompson, 9327
Sandia Laboratory, Albuquerque

*File in Blast h.t.
Bomber
J*

**Reproduced From
Best Available Copy**

DISTRIBUTION STATEMENT A
Approved for Public Release
Distribution Unlimited

20011019 080

SANDIA CORPORATION



PRIME CONTRACTOR TO THE U.S. ATOMIC ENERGY COMMISSION | ALBUQUERQUE, NEW MEXICO; LIVERMORE, CALIFORNIA; TONOPAH, NEVADA

LOVELACE FOUNDATION
DOCUMENT LIBRARY

24207

APR 26 1967

SC-RR-66-376

DYNAMIC PENETRATION OF SELECTED
PROJECTILES INTO PARTICULATE
MEDIA

L. J. Thompson, 9327
Sandia Laboratory, Albuquerque

July 1966

Approved by:

R. C. Maydew
R. C. Maydew, 9320

Alan Pope
A. Y. Pope, 9300

ABSTRACT

This is an overall study of the whole process of projectile penetration into soil. The governing differential equations for the soil target medium are developed using the equations of motion and the continuity condition. Constitutive relationships are derived from Mohr-Coulomb theory for a rigid plastic material and from viscosity theory. The other necessary equations are generated from an experimental investigation of the penetration mechanism.

ACKNOWLEDGEMENTS

The author is grateful for the ideas, the assistance, and the criticism provided by John L. Colp, William N. Caudle, Walter Taylor, Walter Dalby, Lewis Thigpen, Ronald Hultgren, and David Kitzinger of Sandia Laboratory, H. G. Larew of the University of Virginia, and Dean Fred J. Benson of Texas A & M University.

Issued by Sandia Corporation,
a prime contractor to the
United States Atomic Energy Commission

LEGAL NOTICE

This report was prepared as an account of Government sponsored work. Neither the United States, nor the Commission, nor any person acting on behalf of the Commission:

A. Makes any warranty or representation, expressed or implied, with respect to the accuracy, completeness, or usefulness of the information contained in this report, or that the use of any information, apparatus, method, or process disclosed in this report may not infringe privately owned rights; or

B. Assumes any liabilities with respect to the use of, or for damages resulting from the use of any information, apparatus, method, or process disclosed in this report.

As used in the above, "person acting on behalf of the Commission" includes any employee or contractor of the Commission, or employee of such contractor, to the extent that such employee or contractor of the Commission, or employee of such contractor prepares, disseminates, or provides access to, any information pursuant to his employment or contract with the Commission, or his employment with such contractor.

Printed in USA. Price \$6.00. Available from the Clearinghouse for
Federal Scientific and Technical Information,
National Bureau of Standards, U. S. Department of
Commerce, Springfield, Virginia

SUMMARY

Recognizing that aerospace power supplies (both reactor and isotope types) can be subjected to earth impact as a result of circumstances that may occur with a reasonable degree of probability, Sandia Corporation early became concerned with the study of earth impact. More recently, with the increasing interest in the philosophy of intact reentry and disposal by penetration into the earth's surface, Sandia's investigations were amplified to include earth penetration.

One of the objectives of the current investigation is to develop an equation, utilizing dynamic properties of earth materials, that will predict, with a reasonable degree of accuracy, the depth of penetration achieved by a projectile with a known trajectory impacting any given point on the earth's surface.

This report describes the work that has been done to date in the development of an analytical expression which describes the earth penetration process.

TABLE OF CONTENTS

CHAPTER		PAGE
I.	STATEMENT OF PROBLEM AND HISTORICAL	
	BACKGROUND.	1
	Introduction	1
	Historical Background	8
II.	THE ANALYTICAL APPROACH	18
	Introduction	18
	General Continuum Equations	21
	Equations of motion of the soil target	
	medium.	21
	Continuity equation.	26
	The equation of motion of the projectile after	
	it has entered the soil	28
	Energy equation or equation of state	29
	<hr style="width: 60%; margin-left: 0;"/> Summary of equations available from	
	continuum mechanics and requirements	
	for a solution	29
	Constitutive Relationships for Soil	31
	State of stress on an oblique line in the	
	r-z plane	31
	Mohr-Coulomb yield condition.	34
	The flow conditions for the soil	42

CHAPTER	PAGE
Changes in density during shear	52
Relation between the angle of flow and the velocity components	54
The radial normal stress assumption . . .	56
Summary of constitutive equations	57
III. EXPERIMENTAL INVESTIGATION	59
Introduction	59
Type of Experiments	60
Description of Experiments	64
Two-dimensional laboratory tests	64
Three-dimensional laboratory tests	102
Full-scale tests	129
Summary and Results of Experimental Observations	153
IV. SUMMARY OF GOVERNING DIFFERENTIAL EQUATIONS AND REQUIRED BOUNDARY CONDITIONS	179
Summation of Equations	179
Boundary and Initial Conditions	182
Combination of Equations	185
V. CONCLUSIONS AND RECOMMENDATIONS . . .	190
SELECTED BIBLIOGRAPHY	192

LIST OF FIGURES

FIGURE	PAGE
1. Target and Projectile Trajectory Geometry	5
2. Dynamic Free Body of Projectile After It Has Entered the Soil	10
3. Bearing Capacity Factors vs Angle of Internal Friction	20
4. Cylindrical Coordinate System for the Soil Space . .	23
5. Coordinate System and Sign Convention for Stresses .	32
6. Mohr Circle Representation of State of Stress in r-z Plane	35
7. Typical Density- Stress-Deformation Relationships for Soils	37
8. Yield Line Plotted in Mohr Circle Frame	39
9. State of Stress at Yield	41
10. Shear Resistance vs Rate of Deformation for a Visco- plastic Material with a Stress Dependent Yield Limit	45
11. Mohr Circle Plot for Yield Condition and Flow Condition	47
12. Dimensionless Stress vs Angle of Yield Direction (β).	50
13. Setup of Two-Dimensional Constant Velocity Penetration Test Into a Simulated Granular Cohesionless Medium	65
14. Initial Sequence Photo of a Needle Bearing Roller Penetration Test at Constant Velocity	69

FIGURE

viii
PAGE

15.	Second Sequence Photo of a Needle Bearing Roller	
	Penetration Test at Constant Velocity.	70
16.	Third Sequence Photo of a Needle Bearing Roller	
	Penetration Test at Constant Velocity.	71
17.	Final Sequence Photo of a Needle Bearing Roller	
	Penetration Test at Constant Velocity.	72
18.	Unit Resistance vs Nose Shape for the Constant	
	Velocity Two-Dimensional Tests	75
19.	Test Setup for High Speed Penetration Test Into	
	Steel Roller Target	77
20.	Light Gas Gun Projectile After Impact Into Two-	
	Dimensional Steel Roller Target	79
21.	High Speed Movie Frame of Dynamic Penetration	
	Into Steel Roller Target - Time 0.0006 Second	
	After Impact	81
22.	High Speed Movie Frame of Dynamic Penetration	
	Into Steel Roller Target - Time 0.0036 Second	
	After Impact	82
23.	High Speed Movie Frame of Dynamic Penetration	
	Penetration Into Steel Roller Target - Time	
	0.0066 Second After Impact	83

FIGURE

x
PAGE

32.	Laboratory Test Setup for Dynamic Penetration Into Ottawa Sand	93
33.	Initial Frame of High Speed Movie Showing Dynamic Penetration Into Dry Ottawa Sand	95
34.	Final Frame of High Speed Movie Showing Dynamic Penetration Into Dry Ottawa Sand	96
35.	Laboratory Test Setup for Penetration Test Into Gelatin	97
36.	Initial Frame of High Speed Movie of Dynamic Penetration Into Gelatin as Seen Through the Polariscope	99
37.	Intermediate Frame from High Speed Movie of Dynamic Penetration Into Gelatin as Seen Through the Polariscope	100
38.	Final Frame from the High Speed Movie of Dynamic Penetration Into Gelatin as Seen Through the Polariscope	101
39.	Motion-Time and Motion-Penetration Relations for Water Test No. 2	104
40.	Frame from High Speed Movie Showing Dynamic Penetration Into Water	105

FIGURE

PAGE

41.	Motion-Time and Motion-Penetration Relations for Test No. (SO)G-IV-10A	108
42.	Motion-Time and Motion-Penetration Relations for Test No. (SO)G-IV-11C	109
43.	Motion-Time and Motion-Penetration Relations for Test No. (SO)G-IV-12A	110
44.	Motion-Time and Motion-Penetration Relations for Test No. (SO)G-IV-60	111
45.	Motion-Time and Motion Penetration Relations for Test No. (SO)G-IV-40A	112
46.	Motion-Time and Motion-Penetration Relations for Test No. 37A	113
47.	Motion-Time and Motion Penetration Relations for Test No. 38A	114
48.	Motion-Time and Motion-Penetration Relations for Test No. 39A	115
49.	Motion-Time and Motion-Penetration Relations for Test No. 8M	116
50.	Motion-Time and Motion-Penetration Relations for Test No. 9F	117

FIGURE	xii PAGE
51. Motion-Time and Motion-Penetration Relations for Test No. (SO)G-IV-3D	118
52. Photograph of Projectiles After Impact Showing Nose Distress.	120
53. Plan and Side Views of Soil Nose Formed on 1-1/2 inch Blunt Nosed Projectile Fired Into Ottawa Sand	121
54. Three Different Views of Soil Nose that Formed on Hemispherical Nose of 1-1/2 inch Projectile. Ottawa Sand Target	122
55. 1-1/2 inch Projectile and Soil Nose Remains After Penetration Into Ottawa Sand	123
56. Motion-Time and Motion-Penetration Relations for Horizontal Test No. 277-109	125
57. Motion-Time and Motion-Penetration Relations for Horizontal Test No. 277-110	126
58. Blunt Nosed Projectile Flying Out Rear of Horizontal Target	127
59. Image Motion Photograph of Blunt Nosed Projectile Exiting from Pseudo Soil Target	128
60. Description of Soil Strata for Test 120-57	134

FIGURE

PAGE

61. Log of Borings for Tests 120-89 and 120-97.	135
62. Photograph of Surface of Playa Lake Bed After Penetration of 9-inch Blunt Nosed Projectile	136
63. Photograph of Playa Surface with Radial Cracks Marked After Penetration of 9-inch Blunt Nosed Projectile.	137
64a. Side View of Soil Nose Taken from 9-inch Blunt Nosed Projectile After 13.5 feet of Penetration Into Playa.	138
64b. Side View of Soil Nose Taken from 9-inch Blunt Nosed Projectile After 13.5 feet of Penetration Into Dry Lake Playa	139
64c. Plan View of Soil Nose Taken from 9-inch Blunt Nosed Projectile After Penetration Into Playa.	140
65a. Photograph of 9-inch Blunt Nosed Projectile Before Removal from Playa	141
65b. Soil Nose Being Recovered from Playa After Projectile was Removed	141
66. Photographs of Blunt Nosed Projectiles After Penetration Into Dry Lake Playa.	142

FIGURE

PAGE

67.	Motion-Time and Motion-Penetration Relations for Test No. 120-7	145
68.	Motion-Time and Motion-Penetration Relations for Test No. 120-9	146
69.	Motion-Time and Motion-Penetration Relations for Test No. 120-11	147
70.	Motion-Time and Motion-Penetration Relations for Test No. 120-5	149
71.	Photograph of 9.25 Caliber Projectile Before Penetration Into Sand	150
72.	9.25 Caliber Projectile After Sand Penetration . . .	151
73.	Crater in Eglin Sand After Penetration of 9-inch Diameter Projectile	152
74.	State of Stress and Velocity at Soil Nose	156
75.	Assumed Direction of Flow Lines at an Instant of Time	166
76.	Assumed Direction of Flow of Soil	174

CHAPTER I

STATEMENT OF PROBLEM AND HISTORICAL BACKGROUND

I. INTRODUCTION

The basic problem in penetration studies is to determine whether the total force on a given projectile can be calculated at an instant of time when it is at some depth, moving at a given velocity in a given target by using real parameters that describe the mechanical behavior of the target during penetration.

The purpose of this study is to formulate a complete set of equations that might realistically describe the behavior of the soil target and the projectile during the penetration event by using equations from continuum mechanics and soil mechanics and by studies that will delineate the mechanism of penetration and the boundary conditions that those equations must satisfy. The simplest case of a vertical penetration of a rigid right circular cylinder into a half space of homogeneous isotropic soil was used in this study. Some consideration will be given to other projectile configurations. The projectile is considered to be a rigid body moving at a subsonic velocity with respect to the target medium in free flight with its cylindrical axis parallel to the direction of gravity.

Current interest in soil penetration problems stems from the following types of questions:

1. How thick must an embankment be or how much soil cover is required to protect forces and equipment from artillery fire?
2. What forces are exerted upon a projectile as it impacts into soil, water, and soil water air mixtures? How can the projectile be designed structurally to withstand these forces?
3. When a space nuclear power supply is returned from orbit, what will be the depth of penetration? How can the projectile be designed structurally to withstand these forces? so as to keep it intact and achieve the required depth of penetration?
4. When a penetrator impacts into an unknown soil and an acceleration-time signature is transmitted, is it possible to determine the physical properties of the soil and make an estimate of its bearing capacity and mobility?

These are only a few of the problems that can be posed, but these will serve to illustrate the current interest in the phenomenon of penetration. If the basic problem can be solved, many subsidiary

problems can be resolved, and it will be possible to predict the terminal trajectory and depth of penetration.

Penetration may be defined as the forced movement of an object into a larger object. The problem may be classified according to the amount of penetration and the deformation of the projectile.

1. The projectile may hit the target and bounce back, conserving its energy. This is a perfectly elastic impact with no deformation of target or projectile.
2. The projectile may dent the target or form a small crater, then bounce back, and the projectile may be deformed.
3. The projectile may impact and continue its terminal trajectory until all its energy is used and it stops or comes to terminal velocity as in a fluid target.

The problem may be classified according to the forcing function moving the projectile at the time of impact.

1. The forcing function $G(t)$ may be zero—free flight caused by some previous input of energy.
2. The $G(t)$ might be a vibratory load—in the case of driving a pile or vibrating a footing on soil.

3. The $G(t)$ might be a single transient load—such as an object placed on a target and hit with a hammer or even a nuclear blast shock wave passing over the object.
4. The $G(t)$ might be a continuously increasing force with time—as in the case of a rocket being thrust at the time of impact or in the case of a man forcing a spade into the ground.

The problem may be classified according to the angle between the trajectory and the direction of gravity, the angle between the face of the target and the direction of gravity and the angle between the trajectory and the face of the target. The mechanical strength of the target influences the mechanism of penetration in soils because the strength is stress dependent. Therefore, the configuration of the target and restraints to movement at the boundary of the target influence the soil strength and the mechanism of penetration. For example, shooting a projectile into the side of a bank is different from vertical penetration into a half space of soil. See Figure 1.

Thus there are many types of penetration, and in some instances the mechanisms of penetration are similar. However the earth penetration problem is unique in that no other type of penetration completely duplicates it. The penetration of armor plate by a projectile is a shock wave phenomenon and a different problem from penetration into

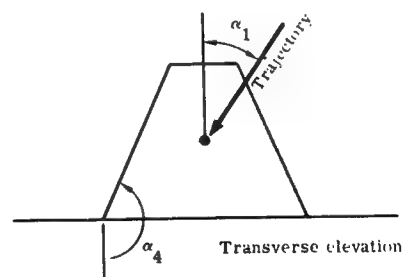
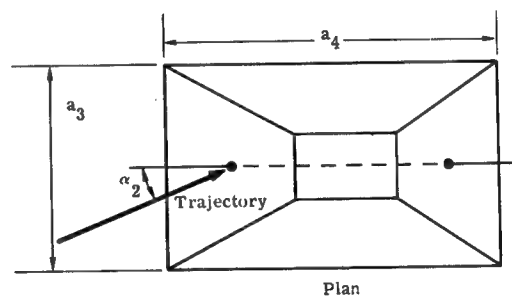
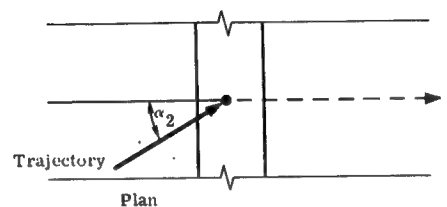
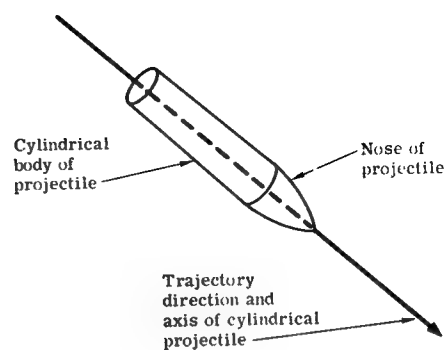
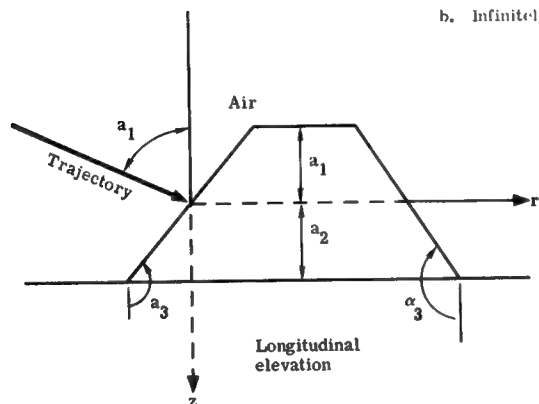
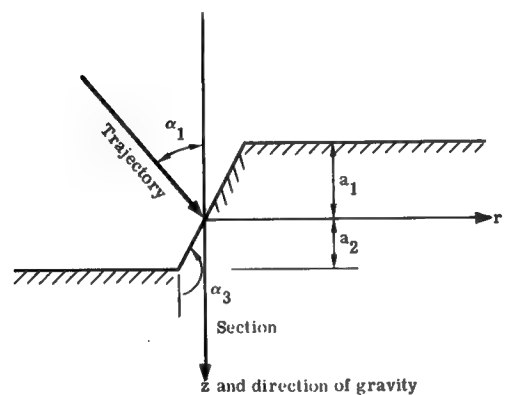
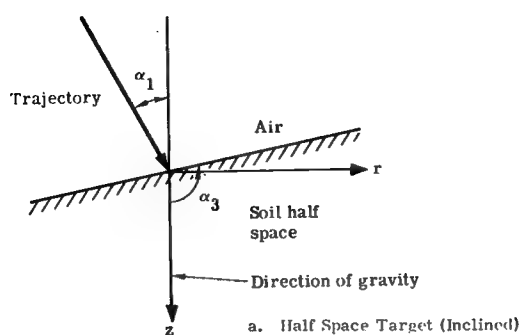


Figure 1. Target and Projectile Trajectory Geometry

a half space. Hypersonic impact of a meteor into metal probably is not the same problem as impact of a .22 caliber bullet into metal even though there may be similarities in the phenomena.

The mechanism of earth penetration is extremely complicated; in the past it has received little attention. Even for the simplest case of vertical penetration into a half space, the velocity regime at impact undoubtedly plays a dominant role in determining the mechanism by which the soil is displaced as the projectile passes from air into soil. Consequently, it cannot be expected that a single comprehensive theory can be readily evolved which will predict the penetration process in its totality for all materials, impact velocities, and collision geometries.¹

In the past, most investigators have concentrated on developing theoretical relations. Some of these relationships are rational, but most of them are empirical, deduced from available data and dimensional analysis and presumed to apply only within definite limits of initial velocity. Target geometry has essentially been ignored. A rational description of the phenomenon of penetration can not be obtained if only the depth of penetration and initial velocity are measured and the target perhaps examined after the event has occurred. The divergent results obtained by different investigators from experimental

¹Werner Goldsmith, Analytical Versions of Penetration Processes, NAVWEPS Report 7812, NOTS TP 2811, February 1962, p. 1.

evidence of supposedly virtually identical tests are due to lack of knowledge of the mechanism of penetration. Also, it is very difficult to build identical targets of soil or to hit the same target area in full-scale tests. Recently it has become possible to measure acceleration or position of the projectile during terminal trajectory in soil, but the response of this instrumentation is limited, and many problems are yet to be solved if exact records are to be obtained.

In this study, equations were formulated in an attempt to describe realistically the behavior of the target during the penetration event. Two-dimensional tests were performed so that the penetration mechanism could be recorded with high-speed photography. Later, three-dimensional tests were performed. These tests led to a description of the boundary conditions and the effects of target geometry and target constraints. Equations were then formulated and assumptions were made which contribute to the solutions of the equations.

It must be remembered that the terminal trajectory penetration is a nonsteady-state problem with one force-free boundary. Even in the case of fluids, few, if any, nonsteady problems have ever been solved.

II. HISTORICAL BACKGROUND

The problem of earth penetration by a projectile received attention as early as 1742 in Robins, New Principles of Gunnery.² The great mathematician Euler considered the problem in his Neue Grundsätze Der Artillerie in the year 1745. Poncelet studied the problem in 1835; Petry's analysis was made in 1910.² From 1910 to 1943, Peres, Probert, Morin and Didion, H. P. Robertson, Nobile de Giorgi and others reported work which evaluated the constants in the formulas previously developed.³ All were concerned with the thickness of embankments required to protect facilities and personnel from artillery fire. The significant findings of each will be summarized in the paragraphs which follow.

All of the above investigators assumed the soil target to be homogeneous and isotropic, with a horizontal surface extending to infinity in every direction and infinitely deep; i. e., a homogeneous soil half space. They also assumed that the projectile or missile impacts

²H. P. Robertson, Terminal Ballistics, National Research Council, 2101 Constitution Avenue, Committee on Passive Protection Against Bombing, Washington, D. C., January 1941.

³Anonymous, Terminal Ballistics and Explosive Effects, National Research Council, Committee on Passive Protection Against Bombing, Washington, D. C., Vol. 2, Appendix to Final Report, 1943.

normal to the half space and that its axis is tangent to the trajectory. The penetration path was considered to be vertical. Tumbling of the projectile was not considered. The missile's shape was assumed to remain undistorted.

Newton's equation of motion is the starting point for all these theories,

$$M g - F = M a_p \quad (I-1)$$

which must hold when the projectile is at any depth and moving at any velocity, where

M = mass of projectile (M_p) plus the soil moving with the projectile (M_c)

g = acceleration due to gravity

F = soil resistance to movement

a_p = acceleration of projectile.

The free body for this equation is shown in Figure 2.

Gravity forces on the projectile are small compared to the soil resistance force; thus, Equation I-1 was rewritten

$$-F = M_p V_p \frac{dV_p}{dz} \quad (I-2)$$

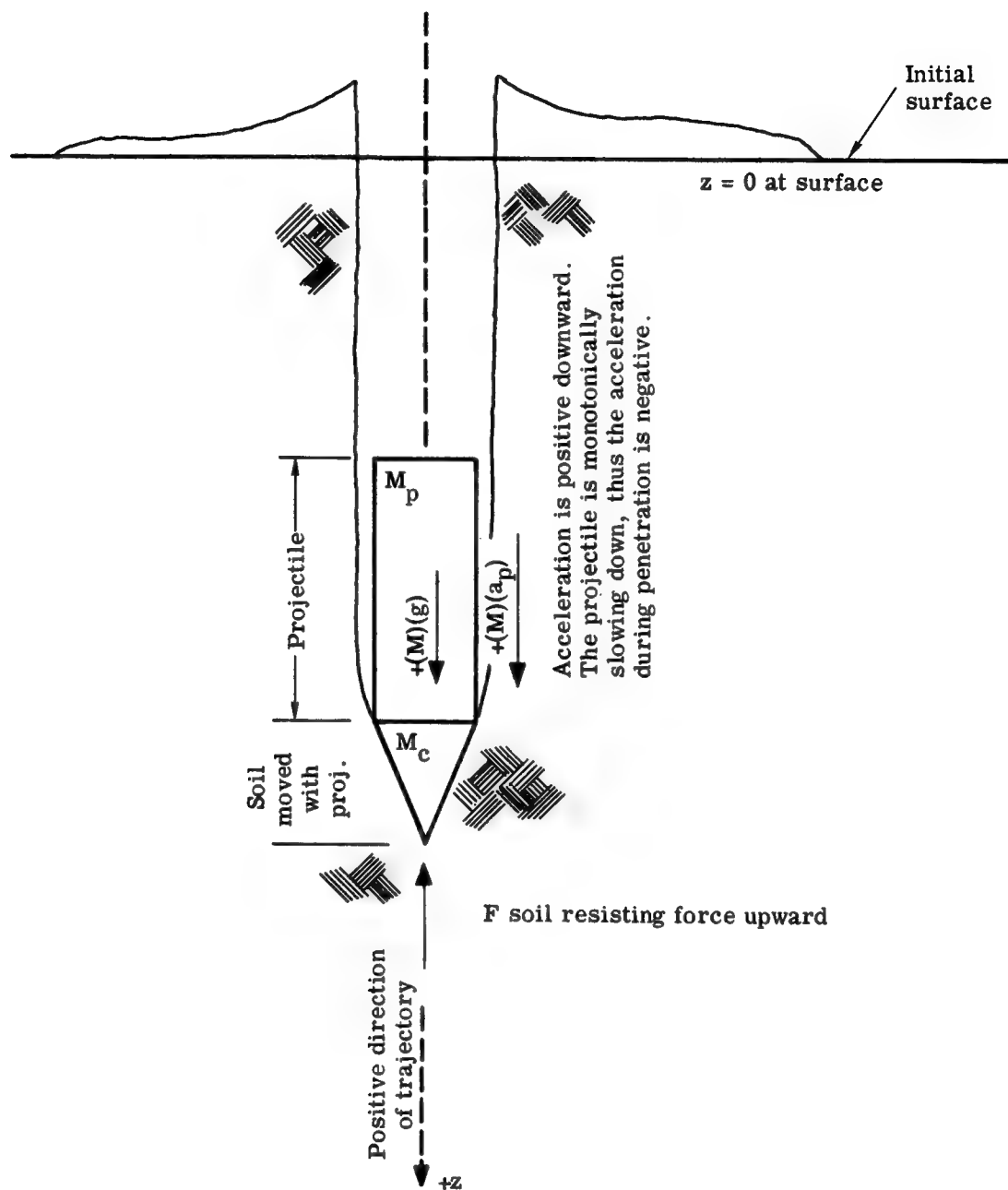


Figure 2. Dynamic Free Body of Projectile After It Has Entered the Soil

where V_p is the velocity of the projectile and z is the distance measured from the surface downward along the trajectory. If no soil is considered to be moving with the projectile, M becomes M_p or the mass of the projectile only.

Euler, Robins and Peres assumed that the soil resistance or drag on the projectile was independent of velocity and depth at any instant of time and proportional to the maximum cross-sectional area of the projectile. Therefore, $F = C A$ where $C =$ a constant and $A =$ maximum area of the projectile. Equation I-2 can then be rewritten

$$- C A dz = M_p V_p dV_p \quad (I-3)$$

when $z = 0$, $V_p = V_i$ or the velocity at impact.

When $z = d$, $V_p = 0$ where d is the depth of penetration. Integrating Equation I-3

$$- C A \int_0^d dz = M_p \int_{V_i}^0 V_p dV_p$$

one obtains

$$- C A d = M_p \frac{V_p^2}{2} \bigg|_{V_i}^0 \quad (I-4)$$

or

$$C A d = M_p \frac{V_i^2}{2}$$

Therefore, in the Euler equation the depth of penetration is

$$d = \frac{W_p}{2 A C g} V_i^2 \quad (I-5)$$

where W_p is the weight of the projectile

The Euler equation assumes a constant deceleration (a linear relationship between velocity and time) and a parabolic relationship between displacement of the projectile and time. Since the soil resistance force is assumed to be independent of velocity, it must be equal to the static resistance to movement. But this static resistive force is now known to be a nonlinear function of depth and area of the projectile. If d is measured in feet, W_p in pounds, A in square inches, g in ft/sec^2 and V_i in ft/sec , Euler's C is 1900 lb/in.^2 . Using data from French and American artillery units in 1932, Peres gave C as 2100.0 lb/in.^2 .

Poncelet assumed that the soil resistance force $F = f_1(z) f_2(V_p)$ where $f_2(V_p)$ is a function only of the velocity of the projectile at any instant of time and $f_1(z)$ is a function only of depth at the same time. Reasoning that the fluid drag on a body is proportional to the square of the velocity, he assumed

$$\left. \begin{aligned} f_2(V_p) &= a + b V_p^2 \\ f_1(z) &= j A \end{aligned} \right\} \quad (\text{I-6})$$

where a , b , and j are constants. Substituting these relationships into Equation I-2, one obtains

$$\begin{aligned} -j A (a + b V_p^2) dz &= M_p V_p d V_p \\ -j A dz &= M_p \frac{V_p}{a + b V_p^2} d V_p \end{aligned}$$

Integrating as before, using the boundary conditions $z = 0$ when $V_p = V_i$ at impact and $z = d$ when $V_p = 0$ and when the total depth of penetration is reached and the projectile is at rest,

$$j A d = M_p \frac{1}{2b} \ln \left(1 + \frac{b V_i^2}{a} \right)$$

or

$$d = \frac{W_p}{2 A j b} \ln \left(\frac{1 + b V_i^2}{a} \right) \quad (\text{I-7})$$

Probert, Morin and Didion tried to evaluate the a and b parameters of Poncelet's equation. The j was ignored or considered to be equal to one. H. P. Robertson reviewed their data and decided that

$$f(V_p) = a + \frac{\gamma k V_p^2}{2g} \quad (I-8)$$

where k is a new constant and γ is the unit weight of the soil. Thus Poncelet's

$$b = \frac{\gamma k}{2g}$$

and Robertson's formula is

$$d = \frac{W_p g}{A \gamma k} \ln \left(1 + \frac{\gamma k}{2g} V_i^2 \right) \quad (I-9)$$

In 1910, Petry called $\frac{W_p}{A} = \sigma$, the frontal loading of the projectile in pounds per square inch, and changed the formula somewhat to obtain

$$d = \sigma k \log_{10} \left(1 + \frac{V_i^2}{215,000} \right) \quad (I-10)$$

If σ is expressed in pounds per square inch, d in feet and V_i in ft/sec., then the k is in ft. in.²/pound. Values given for k were

5.30 for a "sandy soil"

6.95 for a "soil containing vegetation"

10.6 for a "clay soil"

0.775 for limestone

The Petry formula is simple. A nomogram can be prepared relating

- a. frontal loading (weight of projectile / frontal area)
- b. impact velocity
- c. depth of penetration
- d. constant of proportionality

The procedure was to perform a test measuring the first three parameters, then to calculate "k." The k is a variable "constant" which depends on many parameters. Therefore, to make a prediction of the depth of penetration, it is almost necessary to have performed a similar test before, using the same projectile, soil and impact velocity. In the absence of a formula based on theory and utilizing the proper soil parameters, prediction will still have to be made this way. This is the empirical approach.

In summary, for all of these penetration formulas it is assumed that the soil resistance is independent of depth and directly proportional to the area of the projectile. In Euler's formula, the soil resistance is independent of velocity; and in all the others, the soil resistance force is a linear function of the square of the velocity. The Euler formula contains one parameter which is independent of velocity; therefore, it must be equal to the static resistance. But it is now known that the static resistance of soil is a nonlinear function of area

and depth. It is even doubtful that there is any simple relationship between static resistance and dynamic resistance, even if inertial resistance of the soil is taken into account. In the "static" case, the soil is essentially at rest or moving with a very small velocity. In the dynamic case, the soil particles have considerable velocity which can affect the mechanism of penetration.

In the Poncelet formula there are two constants. The "a" is considered to be the static resistance independent of velocity and depth, and the "b" a multiplier for the velocity square term. The same objections would hold true for the Poncelet "a" as were given above for the Euler constant. The drag on a body moving through a fluid is a linear function of the velocity squared; but this applies to the steady-state case only where the velocity is constant, where the body is submerged in a full space, and where target body forces are unimportant. These are certainly not the conditions in the penetration event where the projectile is slowing down in a half space and the target body forces due to gravity probably make one of the most important contributions to the resistance, since the soil's strength is stress dependent.

In all of these earlier attempts, a solution for the soil force resisting movement has been assumed for use in the one differential equation of motion of the projectile. This equation is integrated

5 between the limits of initial velocity at zero depth and zero velocity at final depth. By performing tests where the initial velocity and final depth could be measured when the projectile properties were known, it was possible to compute the "constants" which satisfied the equation. If the assumed solution is correct, it should hold for all soils, projectiles, and initial velocities.

This was the only possible approach to the problem in the past since (1) velocities, displacements and accelerations could not be measured during the penetration event which would immediately allow the checking of the assumed force solution; (2) there was no knowledge of the mechanism of penetration—i. e. , how the soil was displaced from in front of the projectile and how this mechanism was affected by the physical boundary restraints on the target and target geometry; and (3) there were no constitutive equations to describe the relationship between forces imposed by the projectile and the amount of deformation and/or the rate of deformation of the soil medium.

CHAPTER II

THE ANALYTICAL APPROACH

I. INTRODUCTION

Numerous attempts have been made to solve the basic earth penetration problem by using the one equation of motion of the projectile, Equation I-1. There are three unknowns in this equation: F the force on the projectile, V_p the velocity of the projectile and M_c the mass of the soil that moves with the projectile. Thus, two additional equations are needed.

The static (very slow) resistance to penetration of a rigid body such as a pile or footing into a half space has never been rigorously solved. However good approximations are available for shallow penetrations and were developed primarily by Prandtl and extended by Terzaghi⁴ and others. In this slow steady-state solution, the force P required to move a circular plate slowly downward is given by

$$P = \pi R^2 [1.3 C N_c + \gamma d N_q + 0.3 \gamma R N_\gamma] \quad (\text{II-1})$$

⁴Karl Terzaghi, Theoretical Soil Mechanics, (New York: John Wiley & Sons, 1943), Chap. VIII.

where N_c , N_q and N_γ are nonlinear functions of the angle of internal friction ϕ only⁵

C is the cohesive strength of the soil

d is the depth of soil measured from the soil surface
to the bottom of the loaded plate

γ is the effective unit weight of the soil

R is the radius of the loaded circular plate and

ϕ is the angle of internal friction of the soil.

The bearing capacity factors N_c , N_q , and N_γ are shown in Figure 3.

In light of the complexity of even the static case, it seems hopeless to assume the soil resistance function F for even one set of conditions in the dynamic case. The solution of the dynamic penetration problem requires the same general type of analysis that Prandtl used for the static case. The problem, however, is much more complicated because inertial and viscous effects must be considered. One must recognize that the dynamic penetration problem involves the nonsteady case. The projectile is slowing down in proportion to the force exerted on the projectile.

If high response accelerometers can be devised, it may be possible to obtain the trends in the function F for various weights of projectiles,

⁵G. G. Meyerhof, "The Ultimate Bearing Capacity of Foundations," Geotechnique, II (1951), p. 301.

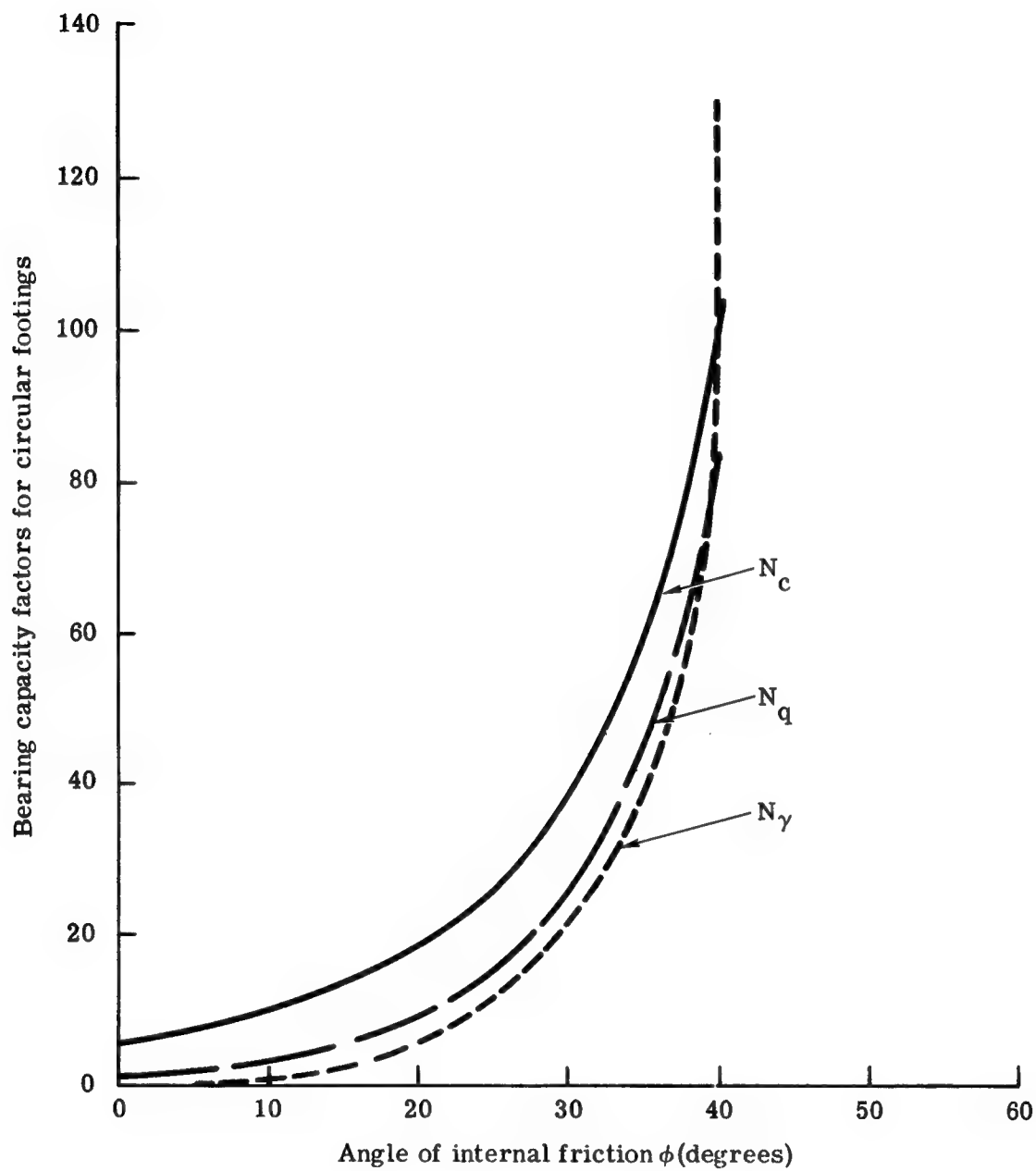


Figure 3. Bearing Capacity Factors vs Angle of Internal Friction

areas, nose shapes, entrance velocities into various targets with different geometries and mechanical properties. These accelerometers are just now being developed, but still the amount of testing required for an empirical solution to the basic problem will be monumental. Therefore, it seemed reasonable to use available continuum equations for the target medium and constitutive equations for soil media to generate equations, the solution of which may be helpful in the reduction of the monumental testing program otherwise required.

II. GENERAL CONTINUUM EQUATIONS

Equations of Motion of the Soil Target Medium

First, consider Newton's second law written for the soil particles for the three spatial orthogonal directions. The simple and elegant equation of motion for any continuous medium was first discovered by Cauchy.⁶ It is given by

$$\rho \frac{d\bar{V}}{dt} = \rho \bar{B} + \text{div } \bar{T} \quad (\text{II-2})$$

where ρ = the soil density function

\bar{V} = the velocity vector

\bar{B} = the body force vector

⁶A. -L. Cauchy; Ex. de Math. 3 (1828), Oeuvres (2) 8, pp. 195-226.

div = the divergence operator

$\overline{\overline{T}}$ = the stress tensor

This equation is valid independent of the mechanical properties of the material and the form the stress tensor may take.

Cylindrical coordinates have been adopted for the inertial space, and the Eulerian or spatial form employed is shown in Figure 4. The body force vector is equal to the acceleration due to gravity acting downward in the positive z direction or parallel to the trajectory of the missile. Thus Cauchy's equation in the three cardinal directions becomes the commonly known equations of motion in cylindrical coordinates⁷

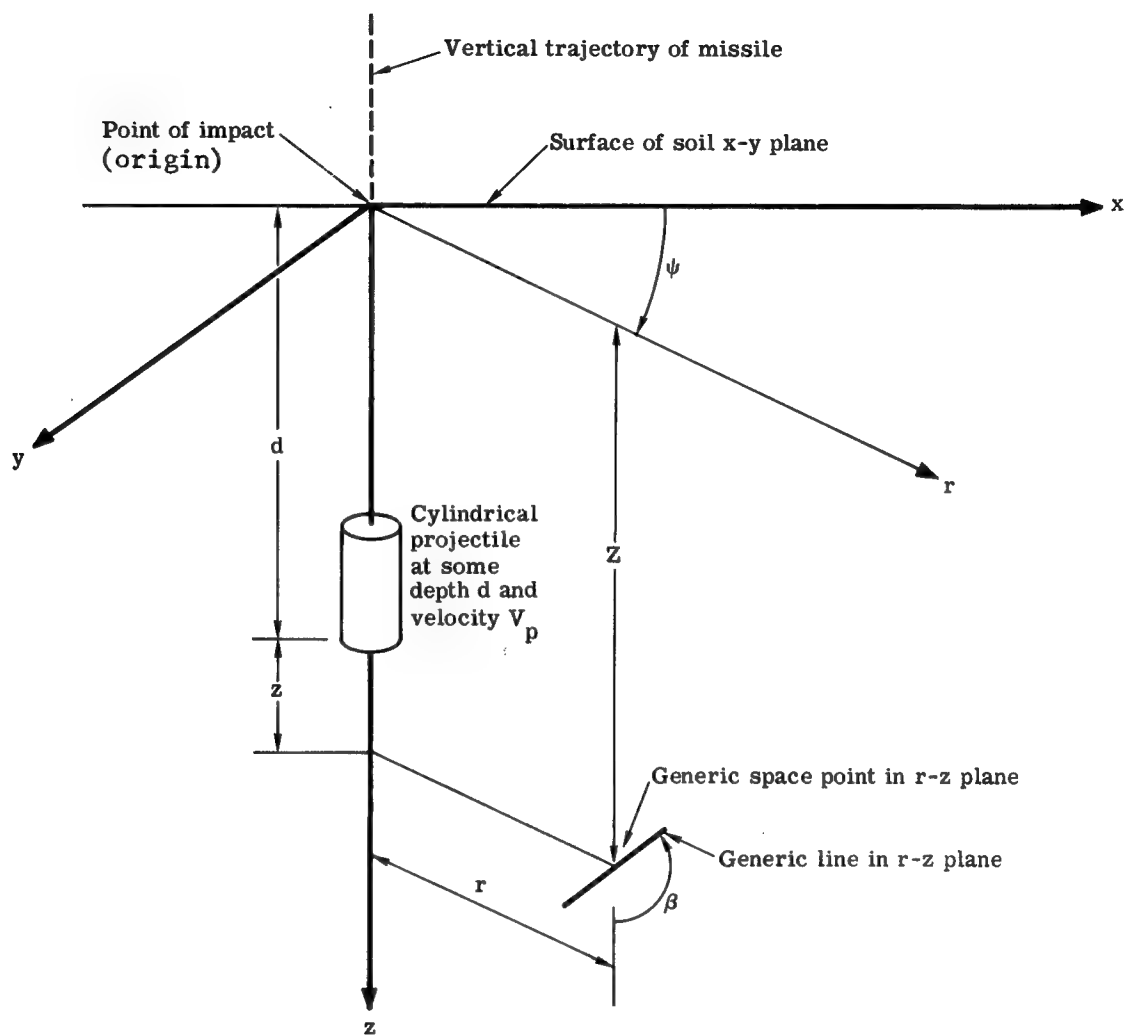
$$-\frac{\partial \sigma_r}{\partial r} - \frac{1}{r} \frac{\partial \tau_{r\psi}}{\partial \psi} - \frac{\partial \tau_{rz}}{\partial z} - \frac{1}{r} (\sigma_r - \sigma_\psi) = \left(\frac{dV_r}{dt} \right) \rho \quad (\text{II-3})$$

$$-\frac{\partial \tau_{\psi r}}{\partial r} - \frac{1}{r} \frac{\partial \sigma_\psi}{\partial \psi} - \frac{\partial \tau_{\psi z}}{\partial z} - \frac{2}{r} (\tau_{r\psi}) = \left(\frac{dV_\psi}{dt} \right) \rho \quad (\text{II-4})$$

$$-\frac{\partial \tau_{zr}}{\partial r} - \frac{1}{r} \frac{\partial \tau_{z\psi}}{\partial \psi} - \frac{\partial \sigma_z}{\partial z} - \frac{1}{r} \tau_{zr} + \rho g = \left(\frac{dV_z}{dt} \right) \rho \quad (\text{II-5})$$

where compressive stresses are taken as positive. The equations are valid for any point in the target space where

⁷J. S. Sokolnikoff, Mathematical Theory of Elasticity (New York: McGraw-Hill Co., 1956), p. 184.



Gravity in z direction

t_o = time of surface impact

t = any time after t_o

$$d = \int_{t_o}^t V_p dt \quad V_p = \text{velocity of projectile}$$

$$z = Z - d$$

Figure 4. Cylindrical Coordinate System for the Soil Space

σ_r = normal stress in the r direction

σ_ψ = normal stress in the ψ direction

σ_z = normal stress in the z direction

V_r = velocity component in the r direction

V_ψ = velocity component in the ψ direction

V_z = velocity component in the z direction

ρ = density of the medium which is function of space
and time

g = acceleration due to gravity

It is specifically assumed that the stress tensor is symmetric; this is true when no extraneous couples are present as in the case of a polarized medium. Thus,

$\tau_{rz} = \tau_{zr}$ = shear stress in the r-z plane

$\tau_{r\psi} = \tau_{\psi r}$ = shear stress in the r- ψ plane

$\tau_{\psi z} = \tau_{z\psi}$ = shear stress in the z- ψ plane

The case considered here is axisymmetric, thus $\tau_{\psi z} = \tau_{\psi r} = 0$, and $V_\psi = 0$, and any derivative with respect to ψ is zero.⁸

Thus, Equation II-3 reduces to

$$-\frac{\partial \sigma_r}{\partial r} - \frac{\partial \tau_{rz}}{\partial z} - \frac{1}{r}(\sigma_r - \sigma_\psi) = \left(\frac{dV_r}{dt}\right)\rho \quad (\text{II-6})$$

⁸S. Timoshenko and J. N. Goodier, Theory of Elasticity, (New York: McGraw-Hill Book Co., 1951), p. 343.

Equation II-4 reduces to the identity $0 = 0$.

Equation II-5 reduces to

$$-\frac{\partial \tau_{rz}}{\partial r} - \frac{\partial \sigma_z}{\partial z} - \frac{1}{r} \tau_{rz} + \rho g = \left(\frac{dV_z}{dt} \right) \rho \quad (\text{II-7})$$

The acceleration terms in the two remaining equations of motion can be expanded by the chain rule to obtain⁹

$$\frac{dV_r}{dt} = \frac{\partial V_r}{\partial t} + V_r \frac{\partial V_r}{\partial r} + V_z \frac{\partial V_r}{\partial z} \quad (\text{II-8})$$

$$\frac{dV_z}{dt} = \frac{\partial V_z}{\partial t} + V_r \frac{\partial V_z}{\partial r} + V_z \frac{\partial V_z}{\partial z} \quad (\text{II-9})$$

since V_r and V_z are both functions of (r, z, t) .

Therefore, the equations of motion can now be rewritten as

$$-\frac{\partial \sigma_r}{\partial r} - \frac{\partial \tau_{rz}}{\partial z} - \frac{1}{r} (\sigma_r - \sigma_\psi) = \left(\frac{\partial V_r}{\partial t} + V_r \frac{\partial V_r}{\partial r} + V_z \frac{\partial V_r}{\partial z} \right) \rho \quad (\text{II-10})$$

$$-\frac{\partial \tau_{rz}}{\partial r} - \frac{\partial \sigma_z}{\partial z} - \frac{1}{r} \tau_{rz} + \rho g = \left(\frac{\partial V_z}{\partial t} + V_r \frac{\partial V_z}{\partial r} + V_z \frac{\partial V_z}{\partial z} \right) \rho \quad (\text{II-11})$$

⁹Salamon Eskinazi, Principles of Fluid Mechanics, (Boston: Allyn and Bacon, Inc., 1962), p. 143.

Continuity Equation

The soil possesses a density function $\rho = \rho(r, z, t)$ which is given by the formula

$$M = \int_{\nu} \rho \, d\nu \quad (\text{II-12})$$

where M = the mass of the soil particles enclosed within a certain region ν with the physical dimensions of mass per unit volume

ν = the volume enclosing these particles and is not necessarily a constant

ρ = mass density of the soil—not necessarily a constant during the event

The physical significance of the concept of mass is given by the principle of conservation of mass:¹⁰ the mass of the soil particles in a material volume ν does not change as ν moves with the soil particles being displaced by the projectile. Thus the principle of conservation of mass is otherwise stated by the expression

$$\frac{d}{dt} \int_{\nu} \rho \, d\nu = 0 \quad (\text{II-13})$$

¹⁰James Serrin, "Mathematical Principles of Classical Fluid Mechanics," Handbuch der Physik, (Berlin: Springer Verlag, 1959), VIII, pp. 125-263.

Since the transport theorem is valid,

$$\frac{d}{dt} \int_{\nu} G d\nu = \int_{\nu} \left(\frac{dG}{dt} + G \operatorname{div} \bar{V} \right) d\nu \quad (\text{II-14})$$

where G is any scalar or vector function

\bar{V} is the vector displacement function

div is the divergence operator

Equation II-13 becomes

$$\int_{\nu} \left(\frac{d\rho}{dt} + \rho \operatorname{div} \bar{V} \right) d\nu = 0 \quad (\text{II-15})$$

Since ν is arbitrary, this implies

$$\frac{d\rho}{dt} + \rho \operatorname{div} \bar{V} = 0 \quad (\text{II-16})$$

in Eulerian or spatial form and

$$\frac{\partial \rho}{\partial t} + \operatorname{div} (\rho \bar{V}) = 0 \quad (\text{II-17})$$

in Lagrangian or material form.

Using the Eulerian form and cylindrical coordinates, the continuity equation becomes

$$\frac{d\rho}{dt} + \rho \left(\frac{\partial V_r}{\partial r} + \frac{V_r}{r} + \frac{\partial V_z}{\partial z} \right) = 0 \quad (\text{II-18})$$

and this equation is valid for any continuous medium.

If $\rho = \text{a constant}$, the equation becomes

$$\frac{\partial V}{\partial r} \frac{r}{r} + \frac{V}{r} + \frac{\partial V}{\partial z} \frac{z}{z} = 0 \quad (\text{II-19})$$

The derivation given above is substantially due to Euler.¹

The Equation of Motion of the Projectile After the Projectile
Has Entered the Soil

$(M_p + M_c) g - F = (M_p + M_c) \frac{dV}{dt}$ (Equation I-1) is the equation of motion of the projectile as it moves through the soil where F is the sum of all forces exerted by the soil upward on the projectile. This force F must also be the sum of all forces exerted by the projectile downward on the soil except the weight. The term M_p is the mass of the projectile, and M_c is mass of soil that might be carried along with the projectile. But

$$F = \int_{\mathcal{S}} \bar{p} \, da \quad (\text{II-20})$$

where \mathcal{S} is the closed surface of the projectile and any soil carried along with it, da is the differential area of the closed surface, and \bar{p} is the stress vector which depends, at any given time, on the position and orientation of the surface element da making up \mathcal{S} . If \bar{n} denotes the outward directed normal to \mathcal{S} , then $\bar{p} = \bar{p}(r, z, t; \bar{n})$. Thus, if the stress field is known at any instant, then \bar{p} can be calculated if \mathcal{S} is known.

¹¹L. Euler, *Principes General due Movement des Fluids*, Hist. Acad. Berlin 1755 (opera omnia II 12), pp. 54-92.

Energy Equation or Equation of State

Most of the work done in deforming the soil medium is transformed into heat, and it is recognized that there will be an increase in temperature of the soil medium during the penetration process. It is assumed that thermal stresses are small in comparison with stresses producing plastic flow, and that temperature changes do not affect the density or mechanical properties of the soil. Interaction between mechanical and thermal processes will not be considered in this study. Thus, the energy equation or an equation of state will not be used as an additional equation.¹²

Summary of Equations Available From Continuum Mechanics and Requirements for a Solution

From continuum mechanics, one obtains the following equations

1. Equation of motion of the projectile

$$(M_p + M_c)g - F = (M_p + M_c) \frac{dV_p}{dt}$$

(Equation I-1)

¹²William Prager, Introduction to Mechanics of Continua, (New York: Ginn and Company, 1961), pp. 87, 88.

2. The vertical resisting force on the projectile is the sum of the forces exerted by the projectile on the soil

$$F = \int_{\mathcal{A}} \bar{p} \, da \quad (\text{Equation II-20})$$

where $\bar{p} = \bar{p}(r, z, t; \bar{n})$ for the axisymmetric case.

3. The two equations of motion of the target medium, which are independent of target mechanical properties

$$\text{a.} \quad -\frac{\partial \sigma_r}{\partial r} - \frac{\partial \tau_{rz}}{\partial z} - \frac{(\sigma_r - \sigma_\psi)}{r} = \left(\frac{\partial V_r}{\partial t} + V_r \frac{\partial V_r}{\partial r} + V_z \frac{\partial V_r}{\partial z} \right) \rho$$

(Equation II-10)

$$\text{b.} \quad -\frac{\partial \tau_{rz}}{\partial r} - \frac{\partial \sigma_z}{\partial z} - \frac{\tau_{rz}}{r} + \rho g = \left(\frac{\partial V_z}{\partial t} + V_r \frac{\partial V_z}{\partial r} + V_z \frac{\partial V_z}{\partial z} \right) \rho$$

(Equation II-11)

4. The continuity equation, which also is independent of target mechanical properties

$$\frac{d\rho}{dt} + \rho \left(\frac{\partial V_r}{\partial r} + \frac{V_r}{r} + \frac{\partial V_z}{\partial z} \right) = 0$$

(Equation II-18)

The independent variables are r, z, t . The dependent variables are $M_c, F, V_p, \sigma_r, \tau_{rz}, \sigma_z, \sigma_\psi, V_r, V_z$ and ρ . Initially, there are available five independent equations with ten unknowns. It is also

required that the surface \mathcal{S} be described as well as the initial conditions (depth of penetration zero) of velocity and stress. The boundary conditions on the stress and velocity fields must also be available if F is to be calculated or the basic problem solved.

Thus, five additional equations are required. These equations must be obtained from constitutive relationships and assumed relationships between the unknown parameters. The constitutive equations relate stresses to strain and strain rate. By taking advantage of the body of knowledge relating stress to yield strain in soil mechanics and using theory from rheology, constitutive equations can be postulated. The additional required equations and boundary conditions must be developed and justified in the mechanism of penetration studies.

III. CONSTITUTIVE RELATIONSHIPS FOR SOIL

State of Stress on an Oblique Line in the r - z Plane

By equating forces on an element of soil using cylindrical coordinates as shown in Figure 5, it is possible to determine the normal stress σ_s and the shear stress τ_s on the line inclined to the z axis at angle β in terms of τ_{rz} , σ_r , σ_z and the angle β . As shown by calculations on page 33, the stresses on an oblique line in the

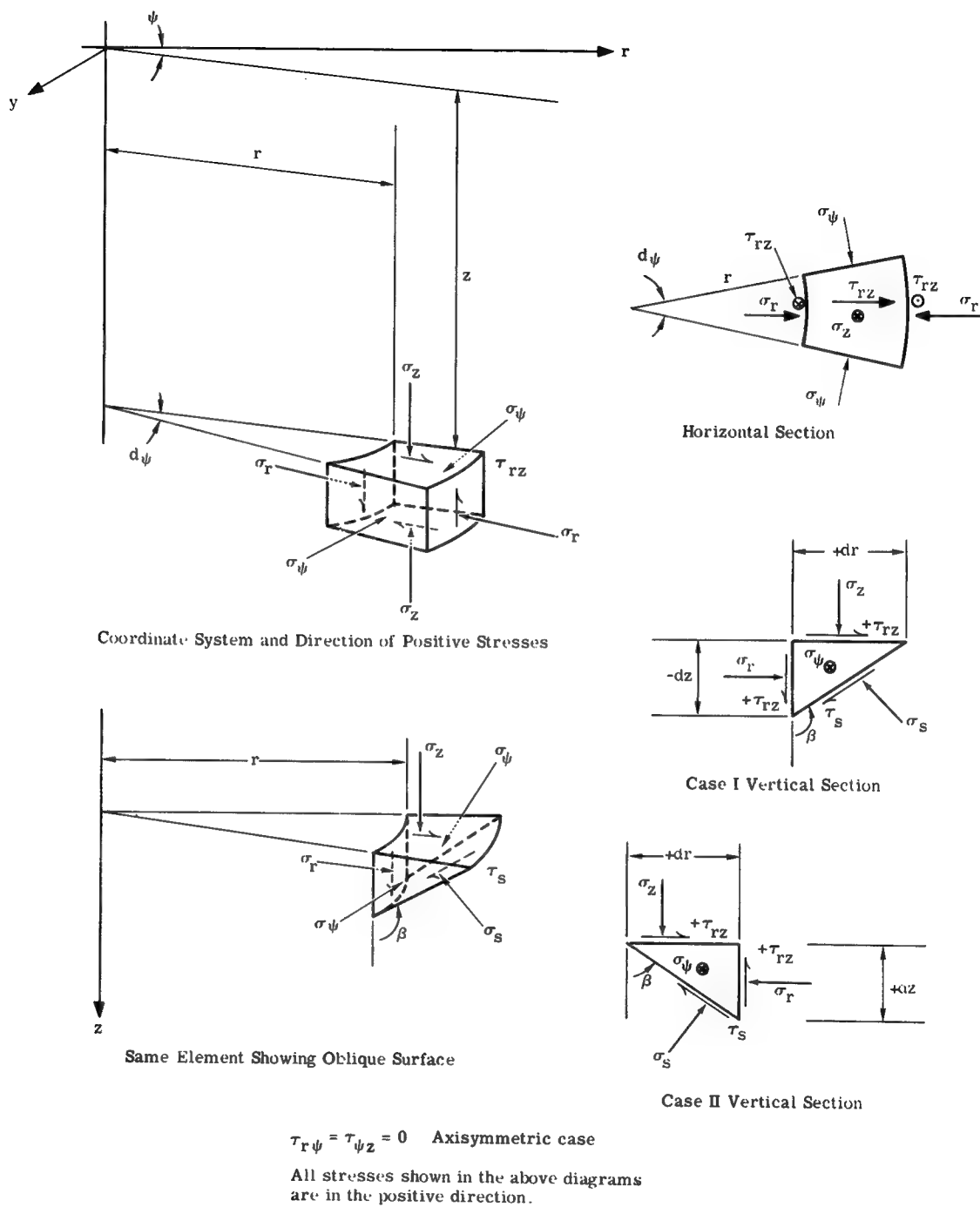


Figure 5. Coordinate System and Sign Convention for Stresses

Consider Case I of Figure 5.

$$\text{Area of top surface of element} = r \, dr \, d\psi$$

$$\text{Area of vertical surface of element} = r \, d\psi \, dz$$

$$\text{Area of side of element} = \frac{dr \, dz}{2}$$

$$\text{Area of oblique surface} = \frac{r \, dr \, d\psi}{\sin(\pi - \beta)} = \frac{r \, d\psi \, dz}{\cos(\pi - \beta)}$$

Equating Forces in r Direction

$$\begin{aligned} & \sigma_r \, r \, d\psi \, dz + \tau_{rz} \, r \, dr \, d\psi + 2 \sigma_\psi \left(\frac{dr \, d\psi}{2} \right) \sin \frac{d\psi}{2} \\ & - \tau_s \left(\frac{r \, dr \, d\psi}{\sin(\pi - \beta)} \right) \sin(\pi - \beta) - \sigma_s \left(\frac{r \, dz \, d\psi}{\cos(\pi - \beta)} \right) \cos(\pi - \beta) = 0 \end{aligned}$$

$$\sigma_r - \tau_{rz} \tan \beta + \tau_s \tan \beta - \sigma_s = 0$$

since the σ_ψ term is of higher order

Equating Forces in z Direction

$$\sigma_z \, r \, dr \, d\psi + \tau_{rz} \, r \, d\psi \, dz + \tau_s \frac{r \, d\psi \, dz \cos(\pi - \beta)}{\cos(\pi - \beta)}$$

$$- \sigma_s \frac{r \, d\psi \, dr}{\sin(\pi - \beta)} \sin(\pi - \beta) = 0$$

$$\sigma_z - \tau_{rz} \cot \beta - \tau_s \cot \beta - \sigma_s = 0$$

Solving Simultaneously

$$\sigma_s = \frac{\sigma_r + \sigma_z}{2} + \left(\frac{\sigma_r - \sigma_z}{2} \right) \cos 2\beta - \tau_{rz} \sin 2\beta$$

$$\tau_s = \frac{\sigma_z - \sigma_r}{2} \sin 2\beta - \tau_{rz} \cos 2\beta$$

Figure 5 (cont). Calculations for the State of Stress on an Oblique Plane in the Axisymmetric Cylindrical Coordinates

r-z plane do not depend on the azimuthal normal stress σ_ψ for the axisymmetric case. Thus the equations

$$\sigma_s = \frac{\sigma_r + \sigma_z}{2} + \frac{\sigma_r - \sigma_z}{2} \cos 2\beta - \tau_{rz} \sin 2\beta \quad (\text{II-21})$$

$$\tau_s = \frac{\sigma_z - \sigma_r}{2} \sin 2\beta - \tau_{rz} \cos 2\beta \quad (\text{II-22})$$

are exactly the same for σ_s and τ_s in the two dimensional plane strain state of stress.¹³ Thus the two-dimensional Mohr circle can be used to represent the state of stress if it is kept in mind that σ_ψ can exist but does not influence the normal and shear stresses on the oblique line in the r-z plane. The Mohr circle representation of this state of stress is shown in Figure 6. These equations are independent of the material's mechanical properties.

Mohr-Coulomb Yield Condition

The Mohr-Coulomb assumption which is used to explain the behavior of soil at failure has been repeatedly verified for so-called "static" equilibrium states of stress. Essentially this is a stress-dependent "law" giving the combination of shear and normal stress for which the soil yields plastically. The formula is a linear representation

¹³A. R. Jumikis, Mechanics of Soils, (Princeton, N. J.: D. Van Nostrand Co., 1964), p. 14.

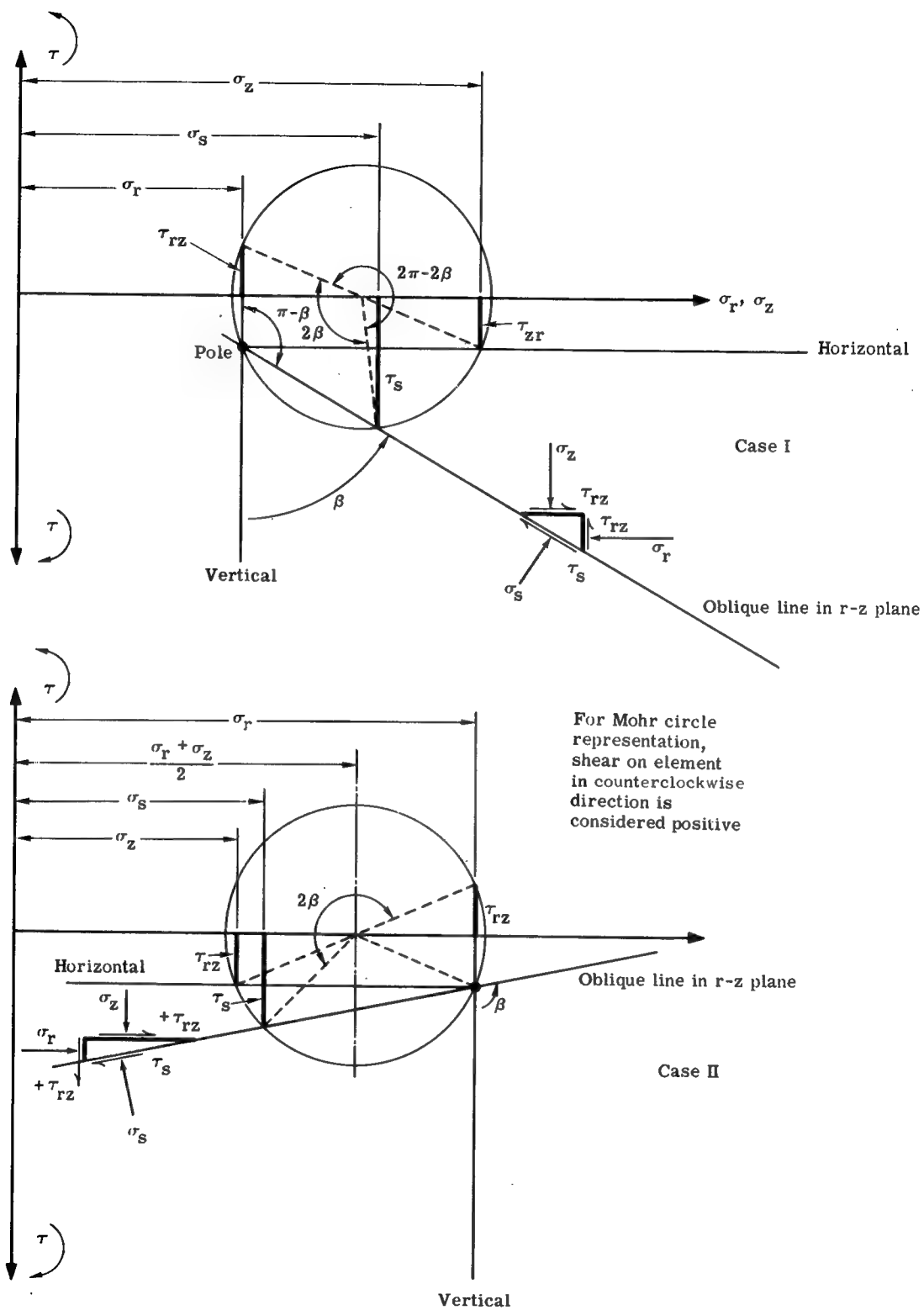


Figure 6. Mohr Circle Representation of State of Stress in r-z Plane

of the failure conditions and is normally satisfactory for practical work where failure by shear or rupture is involved.

$$\tau_s = C + \sigma_s \tan \phi \quad (\text{II-23})$$

where τ_s = shear stress on the surface of failure (sometimes called the slip, yield or failure surface) at the time of failure

C = cohesive strength which is dependent on the past stress (history and moisture content of the soil

σ_s = normal effective stress on the surface of failure at time of failure

$$\sigma_s = \sigma_s - \mu$$

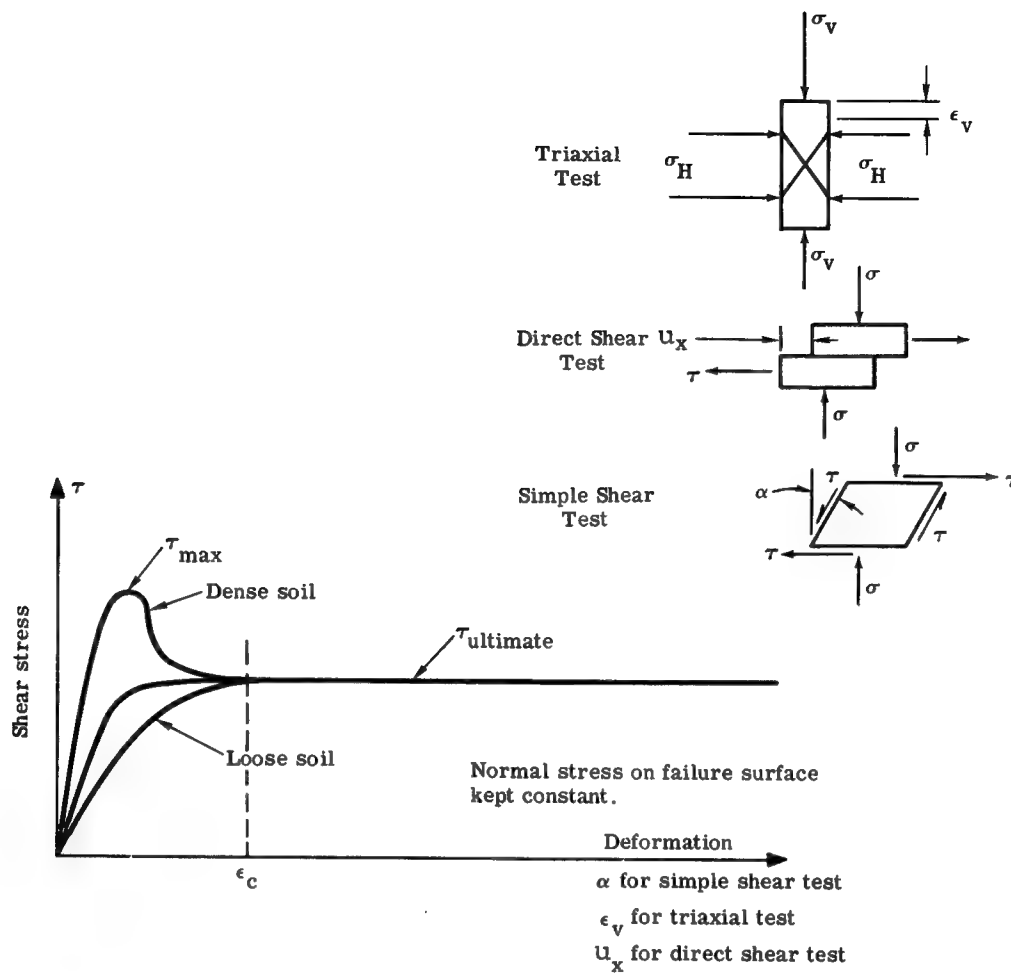
where σ_s = total normal stress on the failure or yield surface

μ = force pressure in the fluid filling the voids within the soil at the point in question

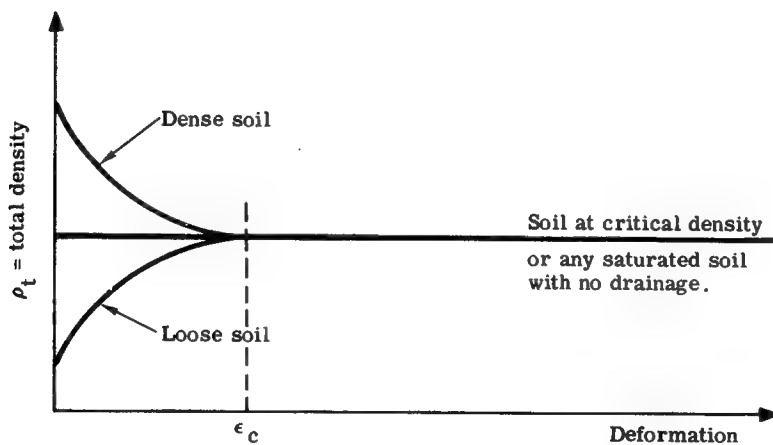
and

ϕ = angle of internal friction (nearly constant for a given soil with a given density)

In Figure 7a some typical plots of the shearing resistance versus shearing deformation are shown. Henceforth all stresses will be considered as effective stresses.



a. Typical Stress-Deformation Relationships for Soils



b. Typical Density-Deformation Relationships for Soils

Figure 7. Typical Density- Stress-Deformation Relationships for Soils

If the soil is dense, its peak strength is greater than its ultimate strength.¹⁴ Since large deformation probably occurs during the penetration event, it will be the ultimate strength that is the important parameter and should be used in determining the angle of internal friction. By performing several tests and then plotting the shearing strength τ_s ultimate versus the effective normal stress σ_s on the plane of failure at the time of failure, the Mohr-Coulomb failure envelope is obtained and C and ϕ ultimate can be determined. A typical plot is shown in Figure 8. Typical plots of density versus deformation are shown in Figure 7b and indicate that volume changes normally occur during at least the early phase of the shearing process. If the stress given by Mohr-Coulomb failure criterion is taken as the yield stress of an ideally plastic medium, the nonhorizontal part of stress-deformation curve of Figure 7a is ignored. The deformation ϵ_c required to reach ultimate strength is normally small so the assumption above seems justified.¹⁵ The deformation which develops in the nonhorizontal part of the shear resistance deformation curve is also usually nonrecoverable when the load is removed.

¹⁴Donald Taylor, Fundamentals of Soil Mechanics, (New York: John Wiley & Sons, 1948), pp. 329-338.

¹⁵D. C. Drucker and W. Prager, "Soil Mechanics and Plastic Analysis or Limit Design," Q. Appl. Math., X (1952), p. 157.

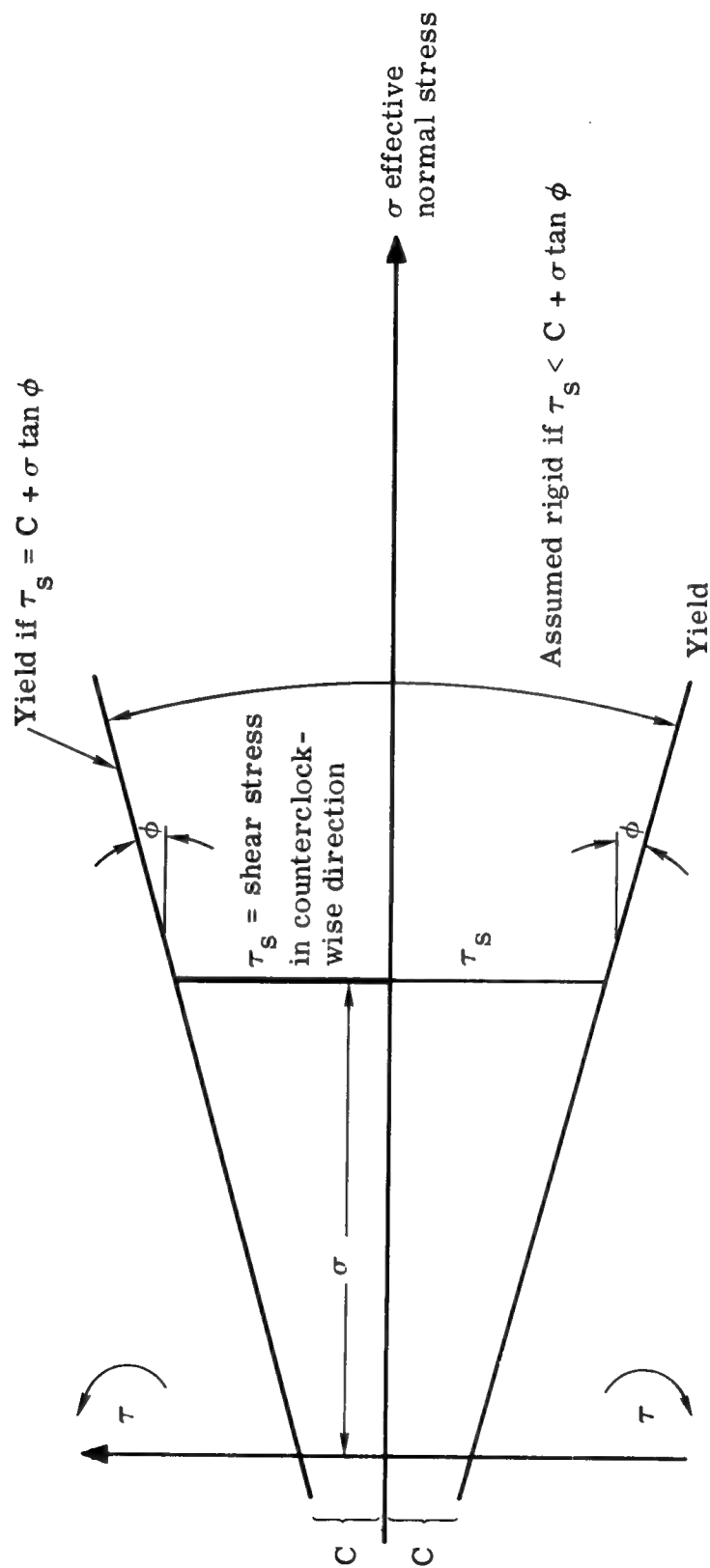


Figure 8. Yield Line Plotted in Mohr Circle Frame

The Mohr-Coulomb yield condition Equation II-23 can be combined with Equations II-21 and II-22 if the stresses τ_s and σ_s are taken as the stresses on the yield or failure surface; thus the angle β designates the direction of the yield surface.

From Figure 9 it can be seen that the Mohr stress circle representing the state of stress at a point must always touch the line of limiting equilibrium given by Equation II-23 if yielding is to occur. If the stresses on the bottom side of the element are always considered positive, i. e., the yielding is always in the positive r direction, then the yield line must pass through the lower point of tangency. From Figure 9 it can be seen that, at yield,

$$\sigma_{z_y} = \sigma_s + \tau_s \tan \phi + \tau_{\max} \cos \alpha \quad (\text{II-24})$$

$$\sigma_{r_y} = \sigma_s + \tau_s \tan \phi - \tau_{\max} \cos \alpha \quad (\text{II-25})$$

$$\tau_{rz_y} = \tau_{\max} \sin \alpha. \quad (\text{II-26})$$

But

$$\tau_{\max} = \frac{\tau_s}{\cos \phi}, \quad (\text{II-27})$$

from Equation II-22

$$\tau_s = C + \sigma_s \tan \phi$$

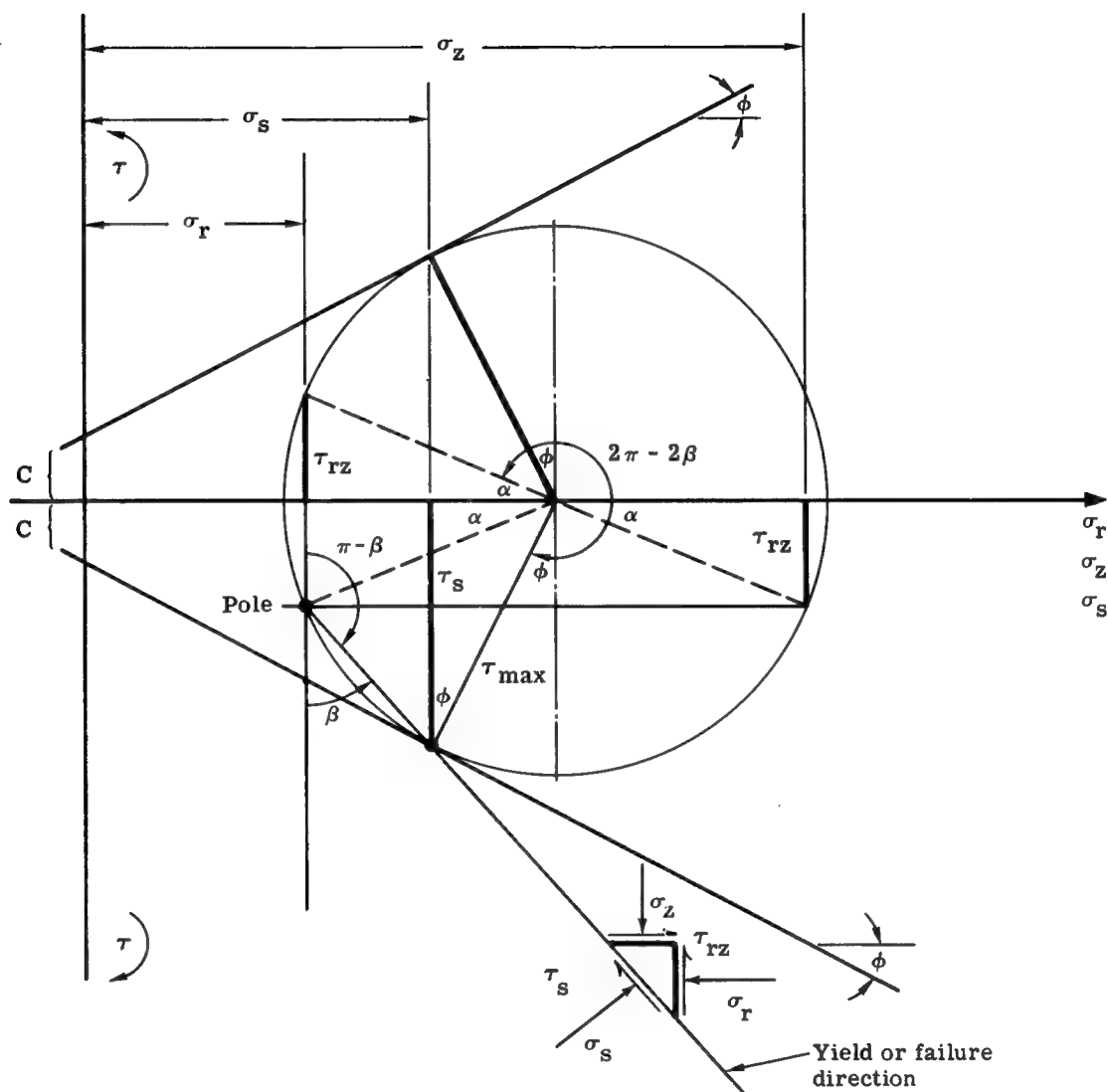


Figure 9. State of Stress at Yield

and

$$\alpha = 2\beta + \phi - \frac{\pi}{2} \quad (\text{II-28})$$

Then

$$\sigma_{z_y} = \sigma_s + (C + \sigma_s \tan \phi) \left[\frac{2 \cos \beta \sin(\beta + \phi)}{\cos \phi} \right] \quad (\text{II-29})$$

$$\sigma_{r_y} = \sigma_s - (C + \sigma_s \tan \phi) \left[\frac{2 \sin \beta \cos(\beta + \phi)}{\cos \phi} \right] \quad (\text{II-30})$$

and

$$\tau_{rz_y} = - (C + \sigma_s \tan \phi) \left[\frac{\cos(2\beta + \phi)}{\cos \phi} \right]. \quad (\text{II-31})$$

Thus σ_r , σ_z and τ_{rz} are written in terms of two new parameters, σ_s and β , for the yield condition. σ_s and β are both functions of r , z , t .

The Flow Conditions for the Soil

The Equations II-29, II-30, and II-31 given above apply to the so-called "static" rigid-plastic yielding case. For dynamic loading conditions to and beyond failure, as is the case for missile penetration,

not only will yielding occur but also viscous flow will be present. Recent tests have indicated that the angle of internal friction may not be influenced much by the rate of deformation, but the cohesion term appears to be highly influenced by the deformation rate.^{16,17,18} For this condition the Mohr-Coulomb envelope would be changed and expanded during a dynamic flow process in direct proportion to the change in the apparent cohesion term. If this increase in apparent cohesion is assumed to be proportional to the rate of shear deformation, as a first approximation, the following flow condition would be obtained.

$$\tau_{sf} = C + K \left(\frac{\partial V_r}{\partial z} + \frac{\partial V_z}{\partial r} \right) + \sigma_s \tan \phi \quad (\text{II-32})$$

where τ_{sf} = shear resistance on the flow surface

C = cohesion as defined before

¹⁶Kent A. Healy, Undrained Strength of Saturated Clayey Silt, M.I. T. Report, March 1963, No. 15, 63-19, Contract No. DA-22-079-Eng. -224 with U. S. Army Engineers Waterways Experiment Station, Dept. of Army.

¹⁷A. Casagrande and S. D. Wilson, "Effect of Rate of Loading on the Strength of Clays and Shales at Constant Water Content," Geotechnique, II (1951), pp. 251-263.

¹⁸Robert V. Whitman and Kent A. Healy, Shearing Resistance of Sands During Rapid Loading. M.I. T. Report, May 1962, No. 9, 62-113, Contract No. DA-22-79-Eng. -224 with U. S. Army Engineers Waterway Experiment Station, Dept. of Army.

σ_s = effective normal stress as defined before

ϕ = ultimate angle of internal friction as defined before

K = apparent soil viscosity coefficient

V_r = velocity in r direction

V_z = velocity in z direction

$$\frac{\partial V_r}{\partial z} + \frac{\partial V_z}{\partial r} = \text{rate of shear deformation}$$

If C' is called the apparent cohesion then

$$C' = C + K \left(\frac{\partial V_r}{\partial z} + \frac{\partial V_z}{\partial r} \right) \quad (\text{II-33})$$

The coefficient of soil viscosity K is in Equation II-31 multiplied by the rate of deformation rather than the velocity gradient.¹⁹ This is justified since the flow condition equation is actually a Bingham body-type flow formula²⁰ where the initial yield shear resistance is a function of the normal stress only. A plot of this "law" is shown in Figure 10

¹⁹Markus Reiner, Deformation, Strain and Flow, (London: H. K. Lewis & Co., Ltd., 1960), p. 20.

²⁰A. M. Freudenthal, The Inelastic Behavior of Engineering Materials and Structures, (New York: John Wiley & Sons, 1950), p. 402.

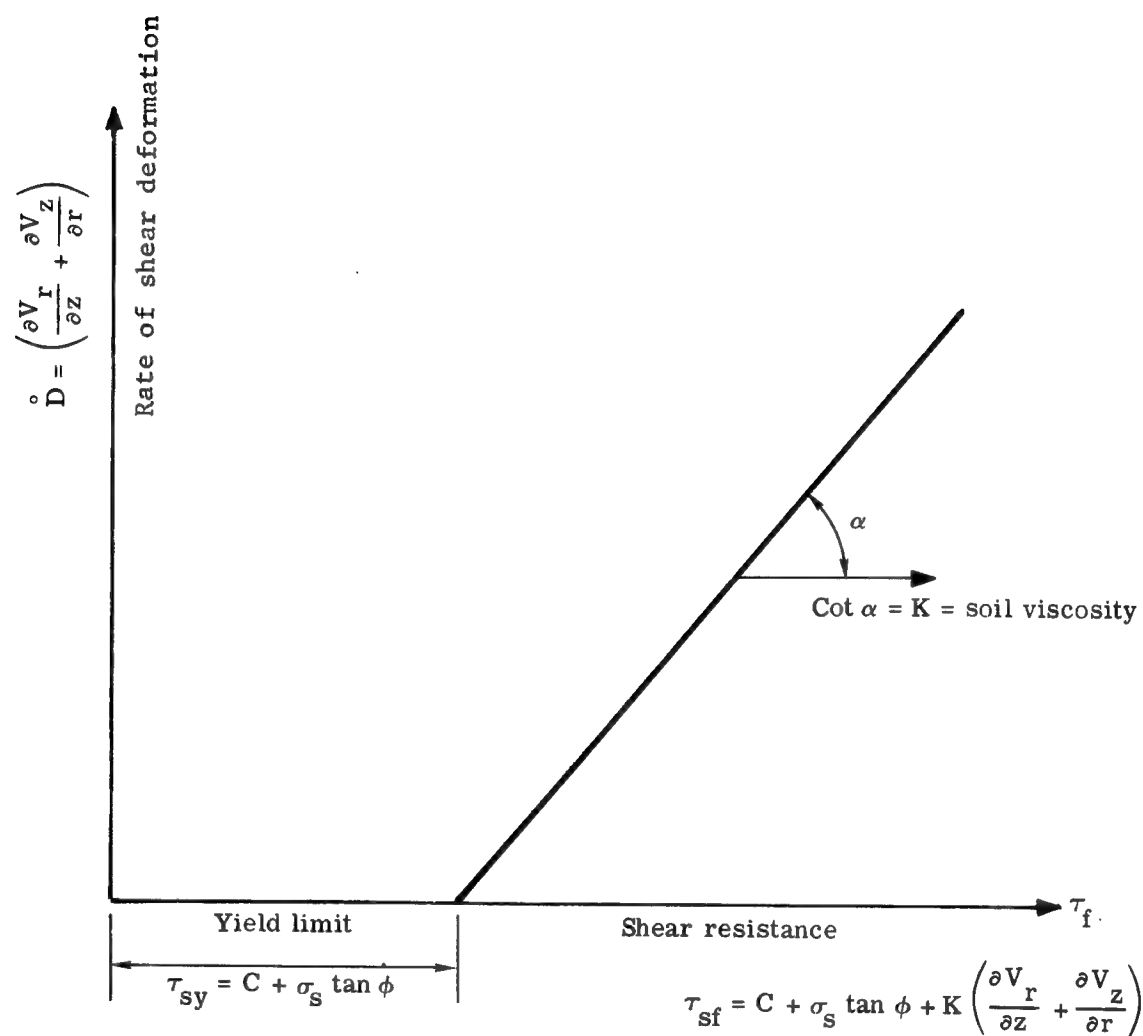


Figure 10. Shear Resistance vs Rate of Deformation for a Viscoplastic Material with a Stress Dependent Yield Limit

Substitution of the flow Equation II-32 into the Equations II-24 through II-26 obtained from the Mohr diagram yields a set of equations similar to the yield Equations II-29 through II-31

$$\sigma_{z_f} = \sigma_s + \left[C + \sigma_s \tan \phi + K \left(\frac{\partial V_r}{\partial z} + \frac{\partial V_z}{\partial r} \right) \right] \left[\frac{2 \cos \beta \sin(\beta + \phi)}{\cos \phi} \right] \quad (\text{II-34})$$

$$\sigma_{r_f} = \sigma_s - \left[C + \sigma_s \tan \phi + K \left(\frac{\partial V_r}{\partial z} + \frac{\partial V_z}{\partial r} \right) \right] \left[\frac{2 \sin \beta \cos(\beta + \phi)}{\cos \phi} \right] \quad (\text{II-35})$$

$$\tau_{rz_f} = - \left[C + \sigma_s \tan \phi + K \left(\frac{\partial V_r}{\partial z} + \frac{\partial V_z}{\partial r} \right) \right] \left[\frac{\cos(2\beta + \phi)}{\cos \phi} \right] \quad (\text{II-36})$$

A Mohr-Coulomb plot for both the yield and flow conditions is shown in Figure 11.

It will be noticed from the Mohr diagram that

1. τ is positive in the equation of motion when

$$\frac{\pi}{4} - \frac{\phi}{2} < \beta < \frac{3\pi}{4} - \frac{\phi}{2}$$

2. τ is negative in the same sense when

$$\frac{3\pi}{4} - \frac{\phi}{2} < \beta < \frac{5\pi}{4} - \frac{\phi}{2}$$

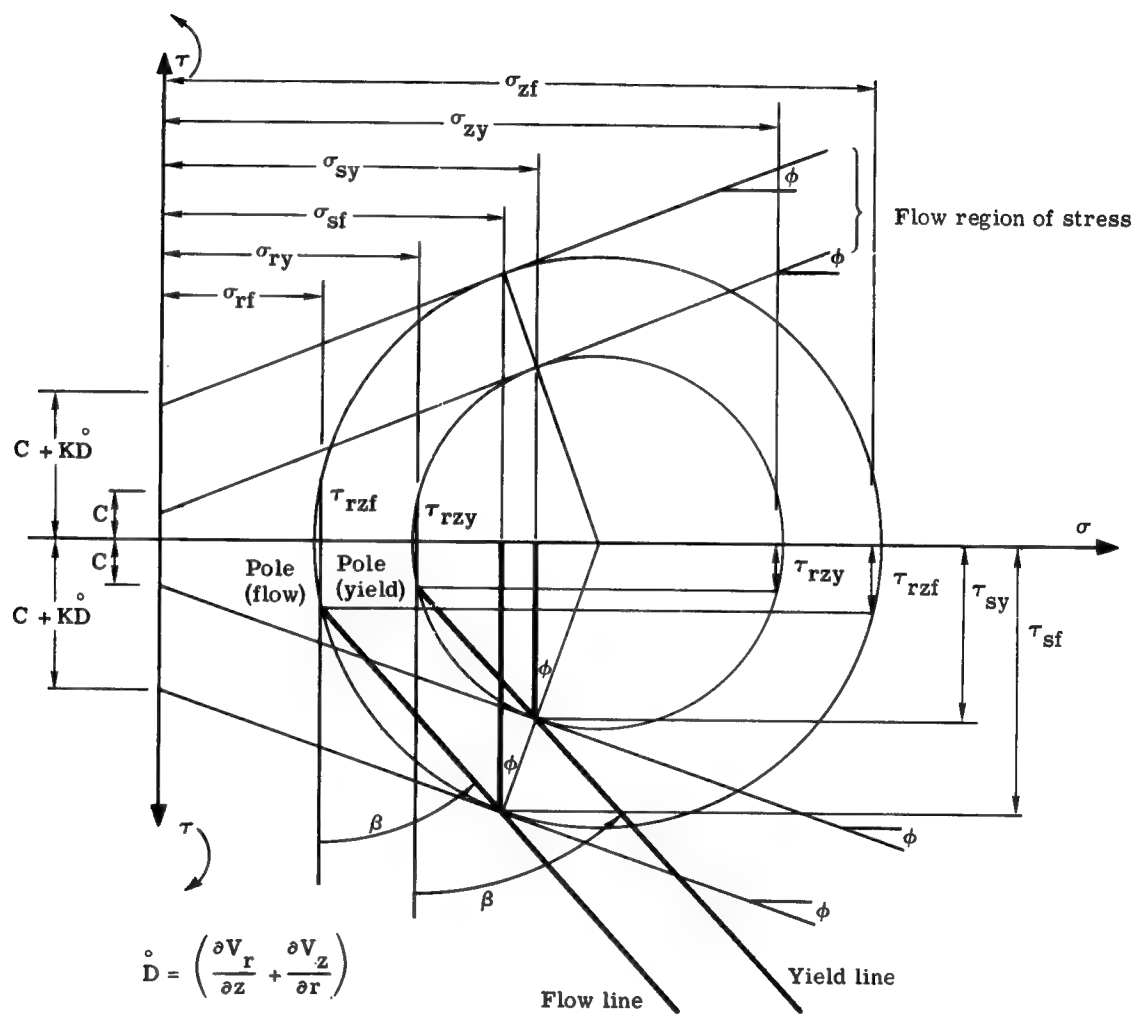


Figure 11. Mohr Circle Plot for Yield Condition and Flow Condition

3. $\sigma_z > \sigma_r$ when

$$\frac{\pi}{4} - \frac{\phi}{2} < \beta < \frac{\pi}{2} - \frac{\phi}{2}$$

and when

$$\pi - \frac{\phi}{2} < \beta < \frac{5\pi}{4} - \frac{\phi}{2}$$

4. $\sigma_r > \sigma_z$ when

$$\frac{\pi}{2} - \frac{\phi}{2} < \beta < \pi - \frac{\phi}{2}$$

For special angles of β the following conditions hold

$$\beta = \frac{\pi}{4} - \frac{\phi}{2} \quad \tau_{rz} = 0 \quad \sigma_z > \sigma_r$$

$$\beta = \frac{3\pi}{4} - \frac{\phi}{2} \quad \tau_{rz} = 0 \quad \sigma_r > \sigma_z$$

$$\beta = \frac{\pi}{2} - \phi \quad \sigma_z > \sigma_r = \sigma_s \quad \tau_{rz} = \tau_s$$

$$\beta = \pi \quad \sigma_z > \sigma_r = \sigma_s \quad -\tau_{rz} = \tau_s$$

$$\beta = \frac{\pi}{2} \quad \sigma_r > \sigma_z = \sigma_s \quad \tau_{rz} = \tau_s$$

$$\beta = \pi - \phi \quad \sigma_r > \sigma_z = \sigma_s \quad -\tau_{rz} = \tau_s$$

$$\beta = \frac{\pi}{2} - \frac{\phi}{2} \quad \sigma_r = \sigma_z \quad \tau_{rz} = \tau_{\max}$$

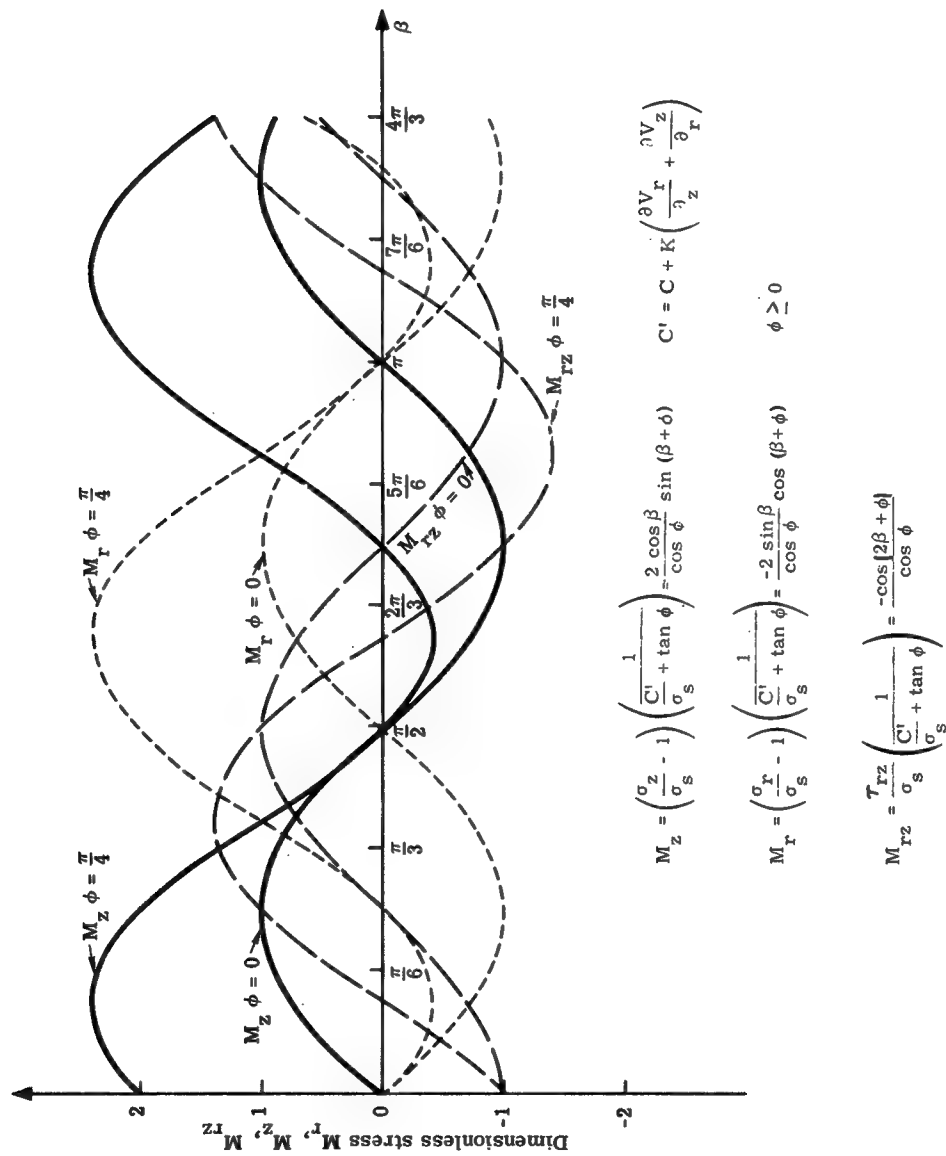
$$\beta = \pi - \frac{\phi}{2} \quad \sigma_r = \sigma_z \quad -\tau_{rz} = \tau_{\max}$$

By algebraic manipulation, formulas can be obtained for a non-dimensional form of Equations II-34 through II-36. Plots of these non-dimensional forms are shown in Figure 12, using the argument β .

The evaluation of the soil viscosity coefficient during dynamic loadings must be done experimentally. It is a basic material property. Research now is being conducted at the University of Virginia and Sandia Corporation to evaluate the changes in ϕ and C during dynamic loadings using a simple shear device.

The equations derived for the shear resistance during yielding and flow may be limited under certain conditions, because it is also possible, if all of the principal stresses are high and applied with a very high rise time, to break the grains and to increase the surface area of the soil particles. This is called comminution.²¹ The comminution effect is seen in the case where a piston is shot into a rigid pipe

²¹H. L. Morrison and W. A. Allen, Projectile Energy Expended in Comminution of the Target, NOTS 1181, NAVORD Report 4885, U. S. Naval Ordnance Test Station, China Lake, California, July 1955.

Figure 12. Dimensionless Stress vs Angle of Yield Direction (β)

filled with sand.²² It may be possible in such a test not only to unlock the structure of the soil, then break the grains,²³ but also if the energy is sufficient, the soil might even be liquified or vaporized. The energy required to comminute soil is high. During initial impact, comminution is known to occur in the velocity regime under study²⁴ when the target is composed of granular materials. Thus, the flow equations developed could not be expected to hold until the projectile has truly entered the soil and shear flow established. The time required to establish shear flow is a function of the velocity of wave propagation in soil.

In summary, it is doubtful that the yield and flow equations would hold when the soil were being comminuted, liquified or vaporized.

²²M. E. Backman and H. L. Morrison, The Fracture of Aggregates of Brittle Particles, NOTS TM No. 1582, U. S. Naval Ordnance Test Station, China Lake, California, November 1953.

²³A. J. Hendron, R. E. Fulton and Bijan Mohraz, The Energy Absorption Capacity of Granular Materials in One-Dimensional Compression, Air Force Special Weapons Center, Kirtland Air Force Base, New Mexico, January 1963.

²⁴Taylor, op. cit., p. 354.

Changes in Density During Shear

As soil is sheared, it expands or contracts in volume so that the density becomes nearly constant depending on the normal stress perpendicular to the surface of movement and stays approximately at this density as shear distortion is increased.²⁵ This ultimate density is called the critical density. Typical plots of density versus deformation are shown in Figure 7b. Critical density is not much influenced by the state of stress as long as the stresses are sufficient to cause movement along yield surfaces. Arthur Casagrande²⁶ was the first to investigate this phenomenon using the direct shear test; later Donald Taylor²⁵ expanded the work also using the triaxial test. K. H. Roscoe²⁷ has continued these investigations using a simple shear device.

For saturated soils, there can be no change in total density, since for high rates of shear deformation the soil does not have time to drain. The thwarted changes in volume of the soil result in a

²⁵Taylor, loc. cit.

²⁶Arthur Casagrande, "Characteristics of Cohesionless Soils Affecting the Stability of Slopes and Earth Fills," Contributions to Soil Mechanics, 1925-1940, Boston Society of Civil Engineers, p. 257.

²⁷K. H. Roscoe, A. N. Schofield and C. P. Wroth, "On the Yielding of Soils," Geotechnique, VIII (1958), p. 22.

corresponding rapid buildup of pore water pressure and a corresponding decrease in the effective normal stress. It would be expected that loose saturated soils would develop high positive (compressive) pore pressures during dynamic loading so liquifaction would result; correspondingly, dense saturated soils would develop high negative (tensile) pore pressures during shear deformation at high rates.

Dry and partially saturated soils are usually found in nature above critical density or below critical void ratio. An exception is loess and it may be that the deformation required to reach critical density is higher for loess than for other soils since it is so compressible. Nevertheless, some critical density should exist for loess after its structure has collapsed by deformation. The increase in volume for dry, dense granular materials is something like 10 percent,²⁸ but the decrease in volume of unsaturated loess and other loose soils may be somewhat higher.

If the initial changes in density are ignored, the density of the soil can be assumed to remain constant during the penetration event, but this density must be taken as the critical density rather than the in situ density. Then in the continuity equation, the density could be

²⁸Whitman and Healy, loc. cit.

considered constant, the material incompressible, and the changes in density due to shear deformation can be ignored. If the density in fact remains constant, it would be expected that the surface of soil half space around the point of impact would be raised and that the volume of the heave would be approximately equal to the hole in the half space caused by the penetrating missile.

Relation Between the Angle of Flow and the Velocity Components

In the flow Equations II-34, II-35, and II-36, τ_{rz} , σ_r , and σ_z are functions of σ_s and β at any instant of time. C , ϕ , and K are assumed constant for a given soil after yield conditions are reached. The angle β designates the direction of yield. The direction of maximum α at any space point in the field that has yielded must be related to the velocity components by

$$\tan \alpha = \frac{V_r}{V_z} \quad (\text{II-37})$$

where α is measured counter clockwise from the z axis. V_r and V_z are the components of the maximum velocity in the r and z directions. It has been shown that the direction of resultant velocity makes an

angle ϕ with the direction of the yield lines because plastic deformation must be accompanied by an increase in volume of the soil if $\phi > 0$.²⁹ This work has been extended³⁰ so as to calculate a velocity field for two dimensional plane strain problems using the concept of a plastic potential.³¹ But these velocity fields are for situations where the soil reaches a critical density when sheared through large deformations. The velocity solutions based on the plastic potential would probably hold for initial motion of soil particles;³² but with continued motion, it will be assumed that the direction of flow α is equal to β , the direction of yield. Then the maximum velocity vector is in the direction of active slip, and the maximum shear strain rate occurs in the direction of yield or active slip.

Thus

$$V_s = V_r \sin \beta + V_z \cos \beta \quad (\text{II-38})$$

$$\tan \beta = \frac{V_r}{V_z} \quad (\text{II-39})$$

²⁹Drucker and Prager, op. cit., p. 157.

³⁰R. T. Shield, "Mixed Boundary Value Problem in Soil Mechanics," Q. Appl. Math., XIV (1953), p. 61.

³¹R. V. Mises, "Mechanik der Plastischen Formaenderung von Krestallen," Z. Angew. Math. Mech., VIII (1928), pp. 161-185.

³²T. H. Wu, Soil Mechanics, (Boston: Allen and Bacon, Inc., 1966), p. 263.

where V_s = the magnitude of the velocity at a point in target space.

The Radial Normal Stress Assumption

The azimuthal normal stress σ_ψ has some influence on the acceleration of the soil as shown by the equation of motion (II-3). The σ_ψ normal stress however does not influence the stresses on the flow or yield surface as shown by the calculations on page 33. By considering the Boussinesq equation for a point load on an elastic half space, it is seen that σ_ψ is always zero or tensile.³³ When Poisson's ratio is one-half, as for an incompressible medium, the stress σ_ψ is zero. But σ_ψ cannot be considered equal to zero since soil is not an elastic material. The maximum and minimum principal stresses must lie in the r-z plane for the axially symmetrical state of stress since movement can only be in the r-z plane. Thus, σ_ψ the radial normal stress must be the intermediate principal stress. According to the Haar-von Karman hypothesis,³⁴ the limiting state of stress at yield is reached when two of the three principal stresses—that is, when two Mohr circles—are tangent to the limiting Mohr envelope. Then, σ_ψ must be

³³Terzaghi, op. cit., p. 374.

³⁴Zdenek Sobotka, "The Slip Lines and Slip Surfaces in the Theory of Plasticity and Soil Mechanics," Applied Mechanics Reviews, XIV (1961), p. 753.

equal to either the maximum principal stress or the minimum principal stress. If a radial soil element is being moved and strained so that the strain in the ψ direction is extension, as in the case of movement away from the center line or z axis, the radial normal stress then would have to equal the minimum principal stress. Then, from Figure 9 it can be seen that at yield or flow

$$\sigma_{\psi_f} = \frac{\sigma_r + \sigma_z}{2} - \tau_s \quad (\text{II-40})$$

$$\text{or} \quad \sigma_{\psi_f} = \sigma_s + (C' + \sigma_s \tan \phi) \left(\frac{\sin \phi - 1}{\cos \phi} \right) \quad (\text{II-41})$$

Summary of Constitutive Equations

The following six equations can now be added to the equations from continuum mechanics. The boundary conditions and initial conditions must still be defined, and also the equation of the surface \mathcal{S} of the projectile and the mass of soil carried by the projectile M_c must be determined, since two new parameters σ_s and β have been introduced. Henceforth, σ_r , σ_z , σ_ψ , σ_s , τ_s , and τ_{rz} will be considered the effective stresses at flow and/or yield, and the subscripts f and y will be dropped as well as the bar to denote effective stress.

$$\sigma_z = \sigma_s + \left[C + \sigma_s \tan \phi + K \left(\frac{\partial V_r}{\partial z} + \frac{\partial V_z}{\partial r} \right) \right] \left[\frac{2 \cos \beta \sin(\beta + \phi)}{\cos \phi} \right] \quad (\text{II-34})$$

$$\sigma_r = \sigma_s - \left[C + \sigma_s \tan \phi + K \left(\frac{\partial V_r}{\partial z} + \frac{\partial V_z}{\partial r} \right) \right] \left[\frac{2 \sin \beta \cos(\beta + \phi)}{\cos \phi} \right] \quad (\text{II-35})$$

$$\tau_{rz} = - \left[C + \sigma_s \tan \phi + K \left(\frac{\partial V_r}{\partial r} + \frac{\partial V_z}{\partial z} \right) \right] \left[\frac{\cos(2\beta + \phi)}{\cos \phi} \right] \quad (\text{II-36})$$

$$\tan \beta = \frac{V_r}{V_z} \quad (\text{II-39})$$

$$\rho = \text{constant} \quad (\text{II-42})$$

$$\sigma_\psi = \sigma_s + \left[C + \sigma_s \tan \phi + K \left(\frac{\partial V_r}{\partial z} + \frac{\partial V_z}{\partial r} \right) \right] \left[\frac{\sin \phi - 1}{\cos \phi} \right] \quad (\text{II-41})$$

If σ_z , σ_r , σ_ψ and τ_{rz} are less than the right hand side of Equations II-34, II-35, II-36, and II-41, respectively, then the material is considered to be rigid and no movement is occurring.

CHAPTER III

EXPERIMENTAL INVESTIGATION

I. INTRODUCTION

The basic purpose of the experimental program was (1) to establish the boundary and initial conditions which the governing differential equations must satisfy during the penetration event; (2) to study the mechanism of how the soil is displaced during penetration so that realistic assumptions concerning the velocity and stress fields at any instant of time could be made; and (3) to obtain evidence of the validity of the theoretical work.

The secondary purposes were (1) to study the effect of projectile dimensions, weights, and impact velocities upon the mechanism of penetration; (2) to consider the effect of target constraints and initial state of stress in targets; (3) to obtain some acceleration time signatures, using controlled laboratory experiments, that would give some indication of the gross expenditure of the projectile's energy at any instant of time; and (4) to conduct some full scale tests that would complement the laboratory experiments and permit correlation with laboratory tests.

II. TYPE OF EXPERIMENTS

There were two kinds of laboratory experiments—two dimensional and three dimensional. A two-dimensional test was one in which the target material was confined between two clear Plexiglass plates so that the whole event of penetration could be recorded using high speed photography. The thickness of the target medium was one sixteenth of an inch greater than the thickness of the projectile. A three-dimensional laboratory test was one in which the right circular cylinder was shot into a tank filled with the target medium.

Gelatin was used to model a cohesive soil in some of the two-dimensional tests. Dry Ottawa sand was used in both the two- and three-dimensional tests to model a noncohesive soil. Stacked steel needle bearing rollers were also used in some two-dimensional tests to model a noncohesive soil. Water was used in some three-dimensional tests as a lower bound on soils, since soils are composed of mixtures of soil particles, water, and air.

The full scale tests reported were conducted at (1) Sandia Corporation, Area III, Albuquerque, New Mexico; (2) Sandia Corporation, Tonopah Test Range, Nevada; and (3) at Eglin Air Force Base, Florida. The experiments conducted were as follows:

1. Two-dimensional laboratory tests:
 - a. Constant velocity tests into steel needle bearing rollers using different nose shapes, projectile widths and

velocities. Actually, 180 tests were conducted, but only a summary of typical tests is reported. All were tests in which the penetrator was moved down vertically.

- b. Dynamic penetration tests in which parallelepiped projectiles were shot into the various target media. The type of targets and number of tests are as follows:
 - 1. Steel needle bearing—two tests
 - 2. Moist bulked silt—four tests
 - 3. Dry sand—nineteen tests
 - 4. Gelatin—thirty-three tests

Results from only one of each of the above tests are presented in this study. Three of the dry sand tests and four of the gelatin tests were made in which the trajectory of the projectile was horizontal. A 250-pound pull mechanical actuator was used in the gelatin tests as a velocity generator. A light gas gun actuator was built to propel the projectile for all the other tests.

- 2. Three-dimensional laboratory tests:
 - a. Vertical tests into water using a right circular cylindrical projectile: High speed photography was used to

record the motion of the projectile and water. Eleven tests were performed, but results from only one test are presented in this study.

- b. Vertical tests into sand using right circular cylindrical projectiles: The diameter, weight and the initial velocity were varied as well as the density of the sand. One hundred and eleven tests were performed, but results from only eleven tests are reported. Microwave equipment was used to record the motion of the projectile.

Several other tests were performed using various nose shapes at high velocities generated by explosive-actuated devices. No motion time history could be obtained, but the results will be briefly discussed.

- c. Horizontal tests into cylinders of pseudo soils: These tests were conducted by other researchers in Division 9226 at Sandia Corporation. The cylinders of pseudo soil are about 24 inches in diameter, 24 inches long, and composed of various particles mixed with a plastic binder. The projectile was propelled by a rocket sled; projectile nose shape, length, and velocity were varied. The unconfined compressive strength and density of the

targets were varied. One hundred and twenty-one tests have been conducted, but only two tests will be discussed.

3. Full Scale Tests:

Essentially vertical tests into natural deposits of soil: The projectile parameters (velocity, weight, diameter, length and nose shape) have been varied and many different soils have been penetrated. Three blunt-nosed tests into a dry lake playa are part of this study and will be reported. Three sharp-nosed tests in the dry lake playa and one into clayey sand are reported, but these tests have been conducted by others at Sandia Corporation. Time vs. deceleration data are reported for these tests when the accelerometers and telemetering systems survived.

III. DESCRIPTION OF EXPERIMENTS

Two-Dimensional Laboratory Tests

a. Constant Velocity Penetration Tests -- A series of continuous vertical penetrations was performed using a blunt penetrator at various constant velocities into a uniform density granular target medium having no cohesion.

The equipment used for this investigation consisted of a mechanical linear actuator, a large target tank with a transparent face, an array of steel needle bearing rollers, a load measuring and recording system, and a sequence camera for recording optical data. See Figure 13. The linear actuator used was driven by a 28-volt constant speed electric motor. A pair of lead screws driven by the motor through a gear reduction system actuated a yoke. The penetrator was mounted on the yoke and was guided so that a reproducible vertical stroke was obtained.

The target tank was 46 inches wide by 36 inches high. It was 7/8-inch thick so that the 3/4-inch thick penetrator could enter without encountering any friction on its front or back. By making the thicknesses (z dimension) of both the target material and the penetrator the same, a true two-dimensional (x and y) test was achieved.

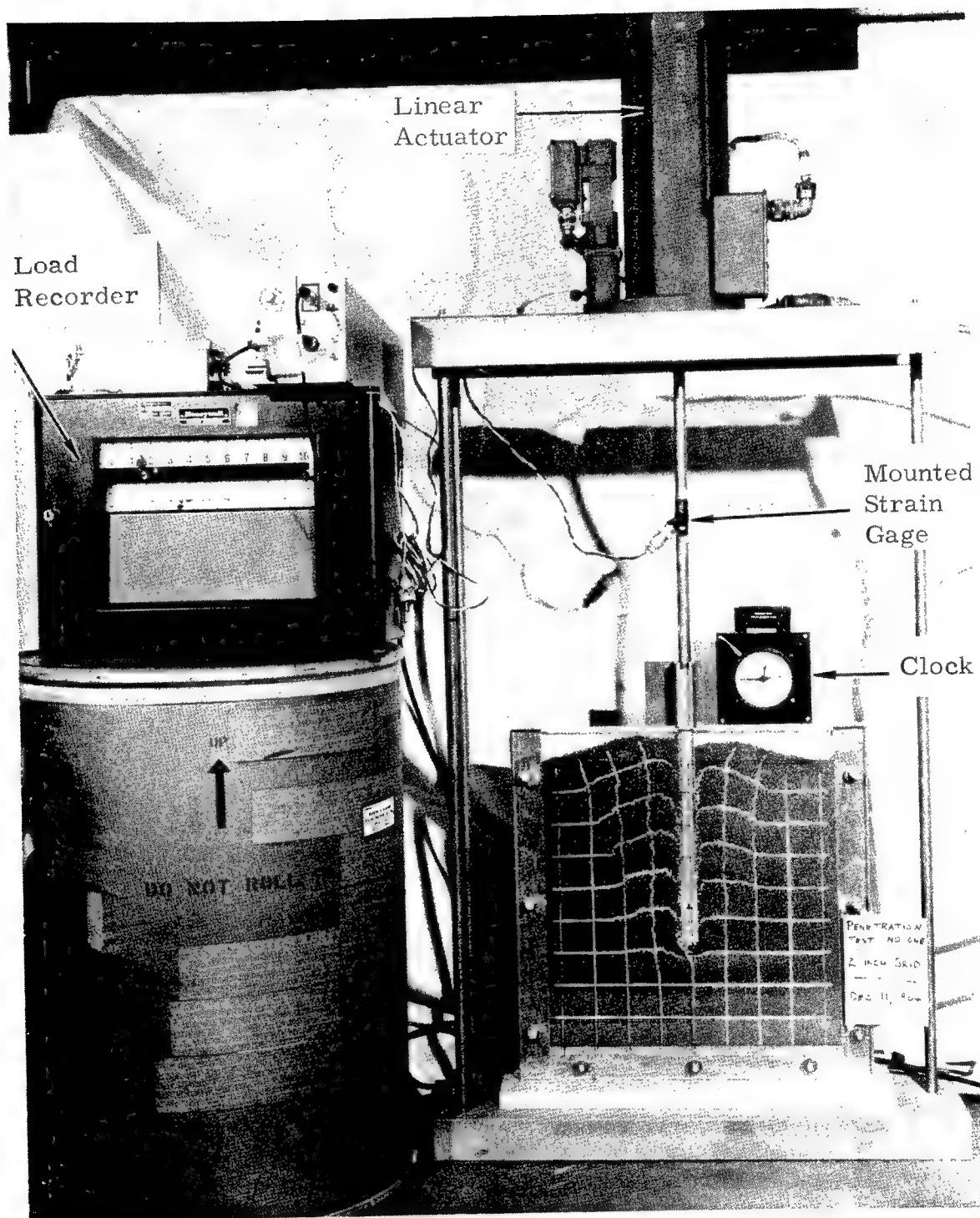


Figure 13. Setup of Two-Dimensional Constant Velocity Penetration Test Into a Simulated Granular Cohesionless Medium

The front face of the target tank was 1-inch thick Plexiglas to permit observation of the movement of the target material during penetration. By removing this front face, the target material could be restacked and returned to its original density, and a grid of lines could be repainted on it for the next test. Methods were developed for these operations so that they could be performed quickly and with reproducible results. The inside surface of the front face of the target tank has a grid of black lines painted over half of it.

The target material consisted of many thousands of precision-ground steel needle bearing rollers of three diameters, $1/16$ -inch, $3/32$ -inch and $1/8$ -inch; all were $3/4$ -inch long and had rounded ends. The three different diameters were randomly distributed throughout the array. They were stacked in the target tank so that the length dimension coincided with the thickness of the tank.

To study movements in the target material caused by penetration forces, a 2-inch square grid of narrow white lines was painted on the front end surfaces of the stacked rollers before each test. After each test, the paint was carefully removed, the array of rollers was carefully restacked as necessary to achieve the original packing (density), and a new grid was painted for the next test.

The load measuring and recording system consisted of a linear strain gauge connected to a Brown recorder. The strain gauge assembly was calibrated before and after each test series. The Brown recorder also was calibrated immediately before and after each test. The recorder operated at a constant paper speed, and an electric clock reading in hundredths of a second was included in the pictures taken of the target tank during each test.

The optical observations of the operation of each test were made with a Nikon Model F single lens reflex 35 millimeter camera equipped with a battery-powered motor. All sequence photographs of the tests were taken at the fastest frame rate of the camera, between three and four frames per second. Kodak Plus X black and white film was used, and full-frame 8-1/2 x 11-inch enlargements were printed with an automatic photo-printer at a constant setting to provide reproducible measurements for an entire individual test sequence.

The test variables investigated included: (1) four different penetrator nose shapes; blunt, triangular, ogive, and semi-circular; (2) three different penetrator widths; one inch, two inches, and three inches; and (3) five different penetrator velocities: 1.8, 2.0, 2.4, 3.0, and 4.4 inches per second. At least two tests were conducted using each of the above nose shapes, widths and velocities for a total of one hundred and twenty tests.

Figures 14, 15, 16, and 17 show a series of sequence photos taken of a test using a blunt penetrator three inches wide at a constant penetration velocity of 2.0 inches per second. It can be seen that particles greater than approximately one projectile width away from the projectile centerline moved toward the surface and away from the projectile. Particles closer to the projectile than this were first displaced toward the surface due to the flow of particles from beneath the penetrator, then they were dragged down with the projectile, but they never attained a depth greater than their original depth. The distortion of the horizontal grid lines indicated that a boundary layer forms along the penetrator in this velocity range. Further, a distinct shear front was seen to move through the medium with and ahead of the projectile in much the same manner as a shock wave proceeds in front of a high-velocity projectile. The shear front is defined as the line which bounds the zone in which no shearing of the medium has occurred. The shape of this front is dependent upon projectile velocity; it is more blunt at lower velocities. The location of the shear front in the medium caused by the penetration event can clearly be seen since it is characterized by a narrow band of material having an increased void ratio. On the surface of the simulated cohesionless soil, the distance from the center line of the penetrator to the shear front monotonically increased as the depth of penetration increased.

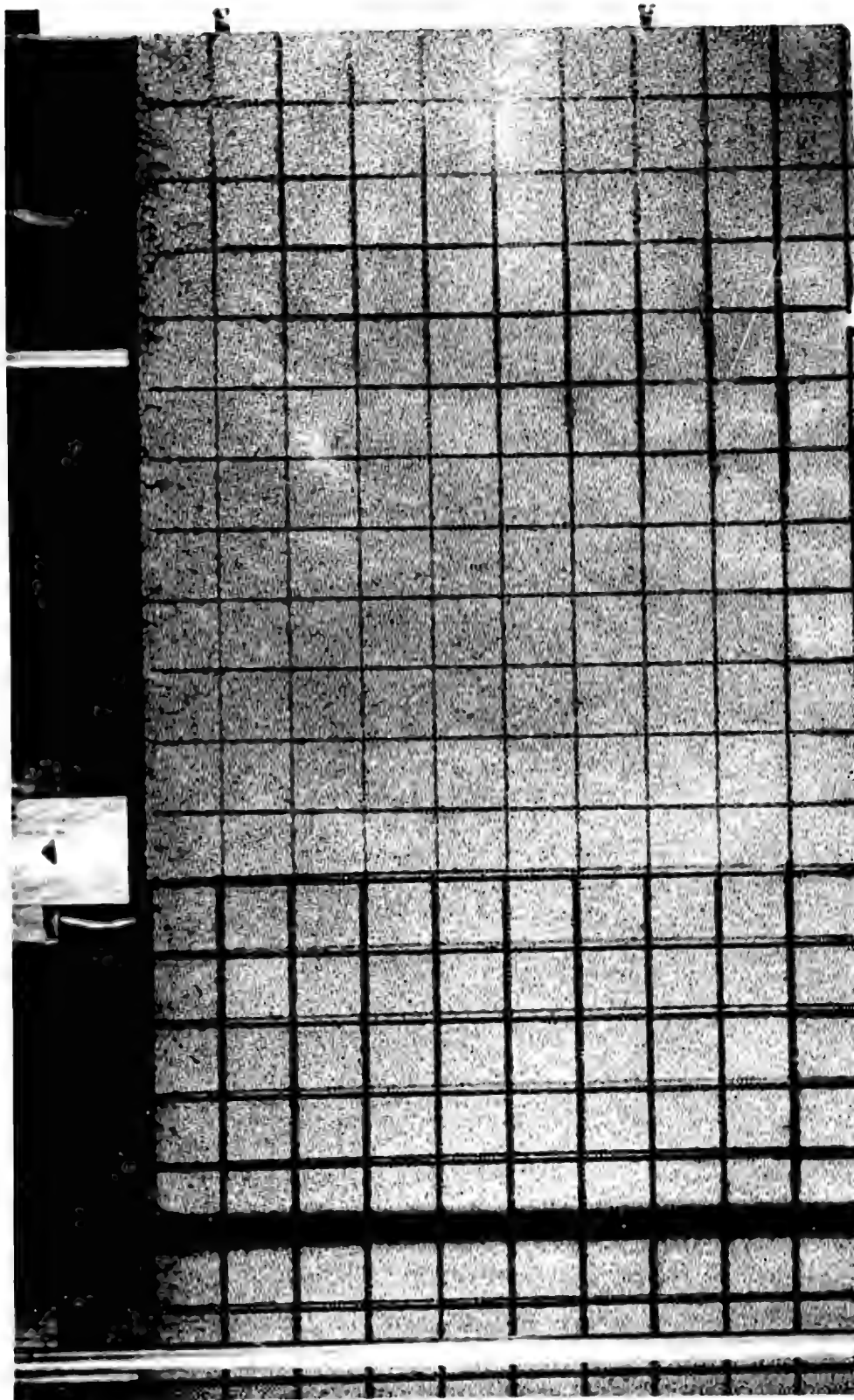


Figure 14. Initial Sequence Photo of a Needle Bearing Roller
Penetration Test at Constant Velocity

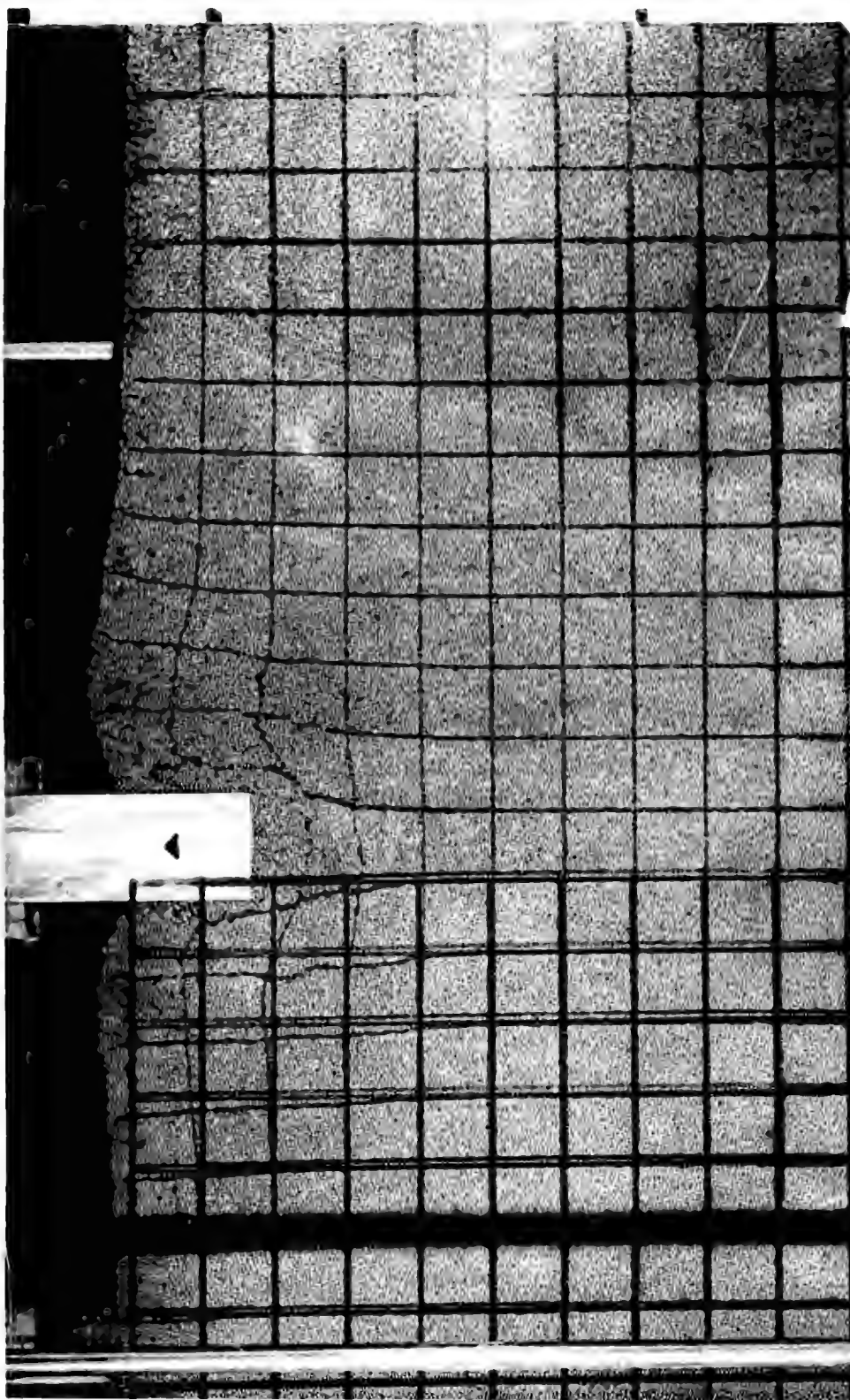


Figure 15. Second Sequence Photo of a Needle Bearing Roller
Penetration Test at Constant Velocity

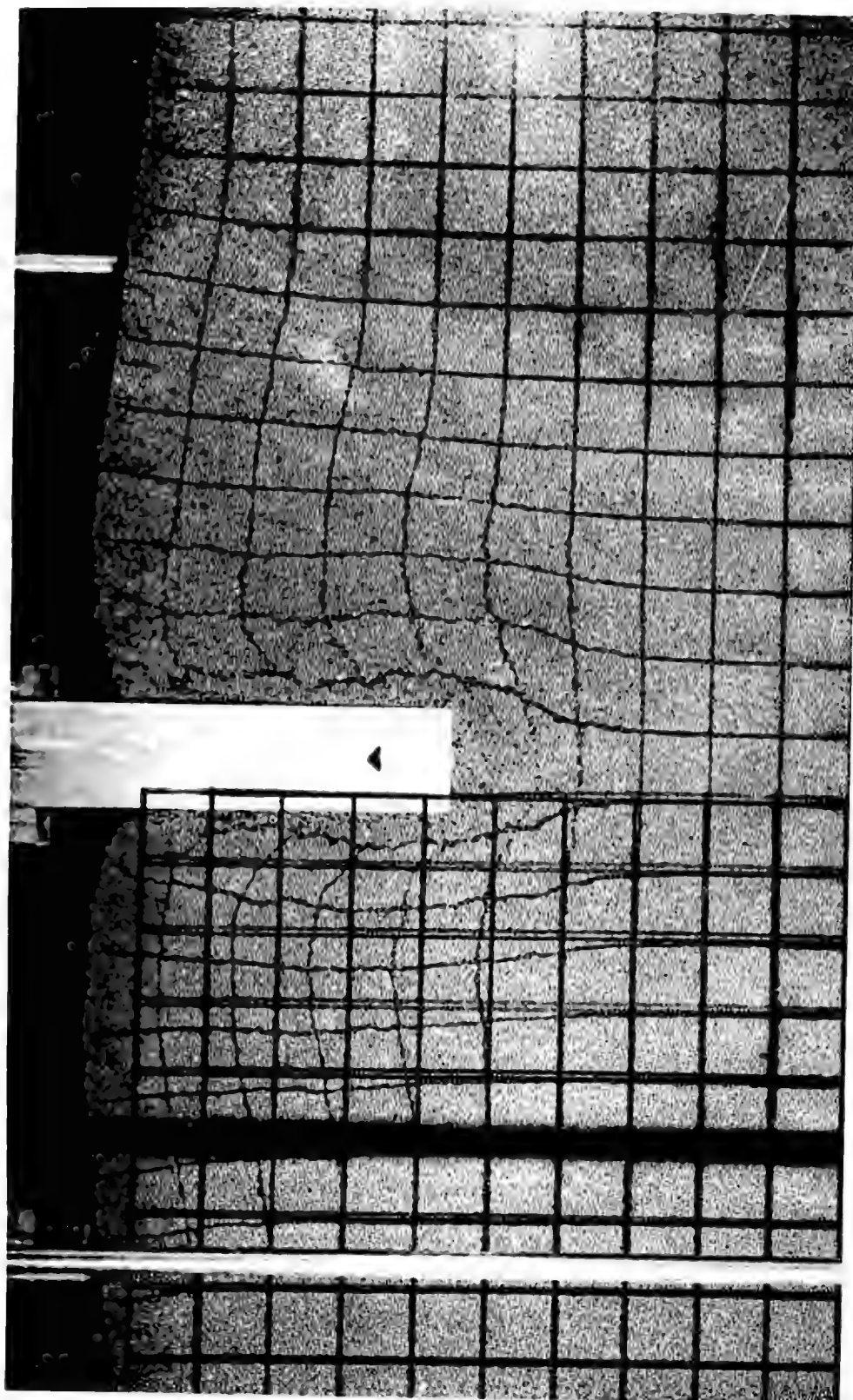


Figure 16. Third Sequence Photo of a Needle Bearing Roller
Penetration Test at Constant Velocity

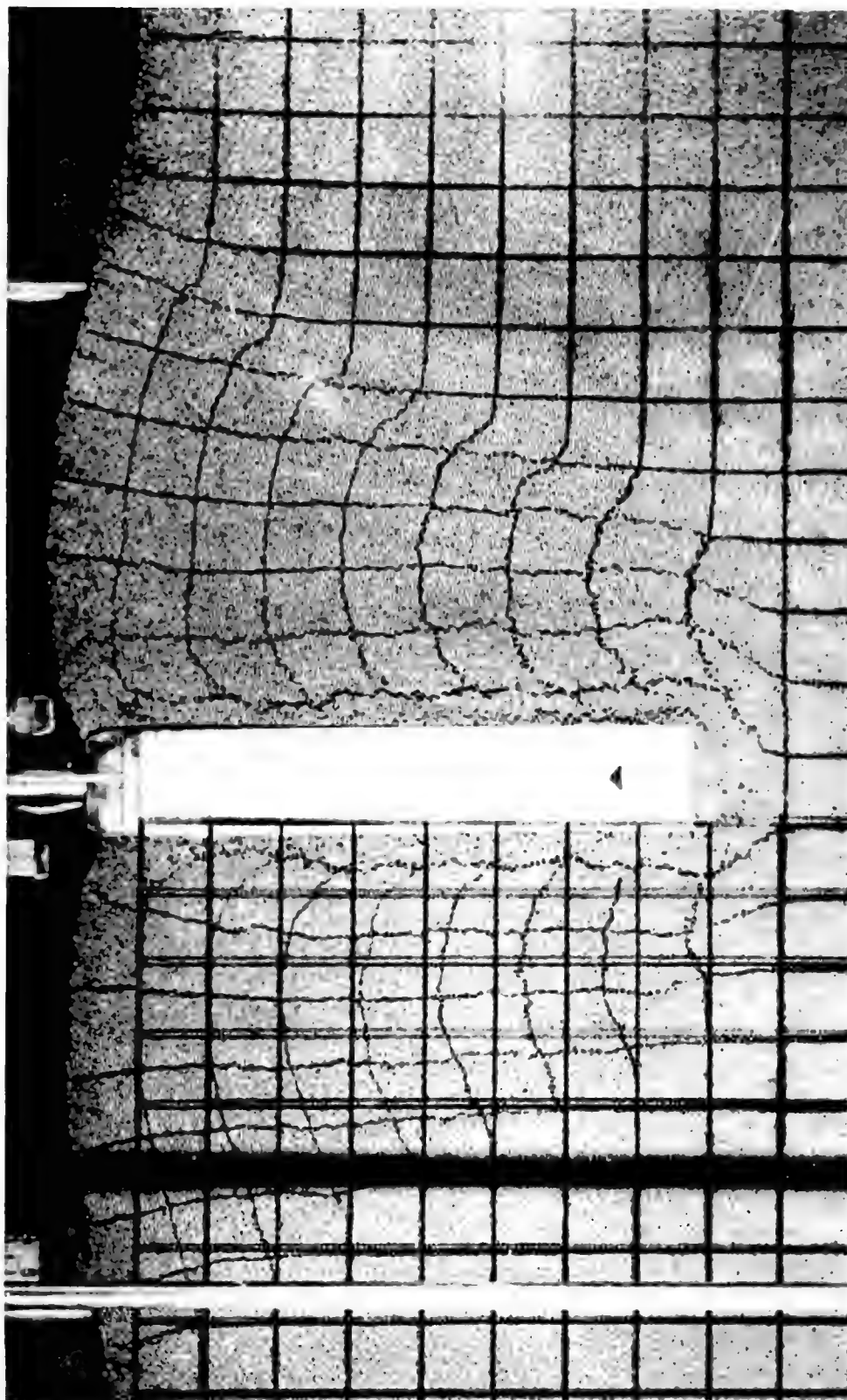


Figure 17. Final Sequence Photo of a Needle Bearing Roller
Penetration Test at Constant Velocity

Typically, particles ahead of the front were stationary. Particle motion started as the front passed any point. If a given grid square of particles in the two-dimensional test is examined, the square is seen to distort as the shear front passed through it. Once the front had completely passed through, the distorted square moved as a rigid body toward the surface and away from the penetrator. Horizontal motion of the square, however, is a finite bounded quantity for any penetration depth. In contrast, the vertical displacement increased monotonically with the depth of projectile penetration because the penetrator is continually occupying more of the space, pushing the particles upward toward the direction of least resistance.

For the 2- and 3-inch wide penetrators, slip surfaces developed deep in the medium. These are characterized by stationary material beneath the plane and the material above the slip surface moving entirely as a rigid body. As noted in Figure 17, the grid squares above the slip surface are still square after their motion, yet they have been moved up and away from the penetrator as well as having been tilted.

In the conventional bearing capacity theory, it is assumed that a wedge of the penetrated medium forms in front of the blunt penetrator and stays with it. This wedge is seen in this series of penetration tests, but the particles in the wedge continually change with increasing

depth of penetration. A wedge of the same particles still may exist if the medium has cohesive strength.

A preliminary analysis of unit resistance at a depth of 15.4 inches, using three velocities, three widths and four nose shapes is shown in Figure 18. The curves show the variation in average unit resistance (112 tests) versus the length to diameter $\left(\frac{L}{D}\right)$ of the four nose shapes. The nose shapes tested were, blunt, semicircular, triangular and six caliber ogive. The relationship between resistance and depth of penetration was nearly linear.

The unit resistance to penetration decreases with increasing penetrator width for each nose shape tested. Intuitively, this situation does not seem reasonable; however, Hvorslev³⁵ and Kerisel³⁶ report similar observations under considerably different test conditions but at approximately the same penetration velocities. Earlier tests in the same medium by Colp³⁷ showed this same result for different nose shapes. Unit penetration resistance decreased as the $\left(\frac{L}{D}\right)$ ratio increased.

³⁵M. J. Hvorslev, Discussion at Session II - Shallow Foundations, Symposium on Bearing Capacity and Settlement of Foundations, Duke University, April 1965.

³⁶J. Kerisel, "Deep Foundations Basic Experimental Facts," Deep Foundations Conference, Mexico D. F., Mexico, December 1964.

³⁷J. L. Colp, An Experimental Investigation of the Continuous Penetration of a Blunt Body into a Simulated Cohesionless Soil, Sandia Corporation, Albuquerque, New Mexico, SC-RR-65-260, December 1965.

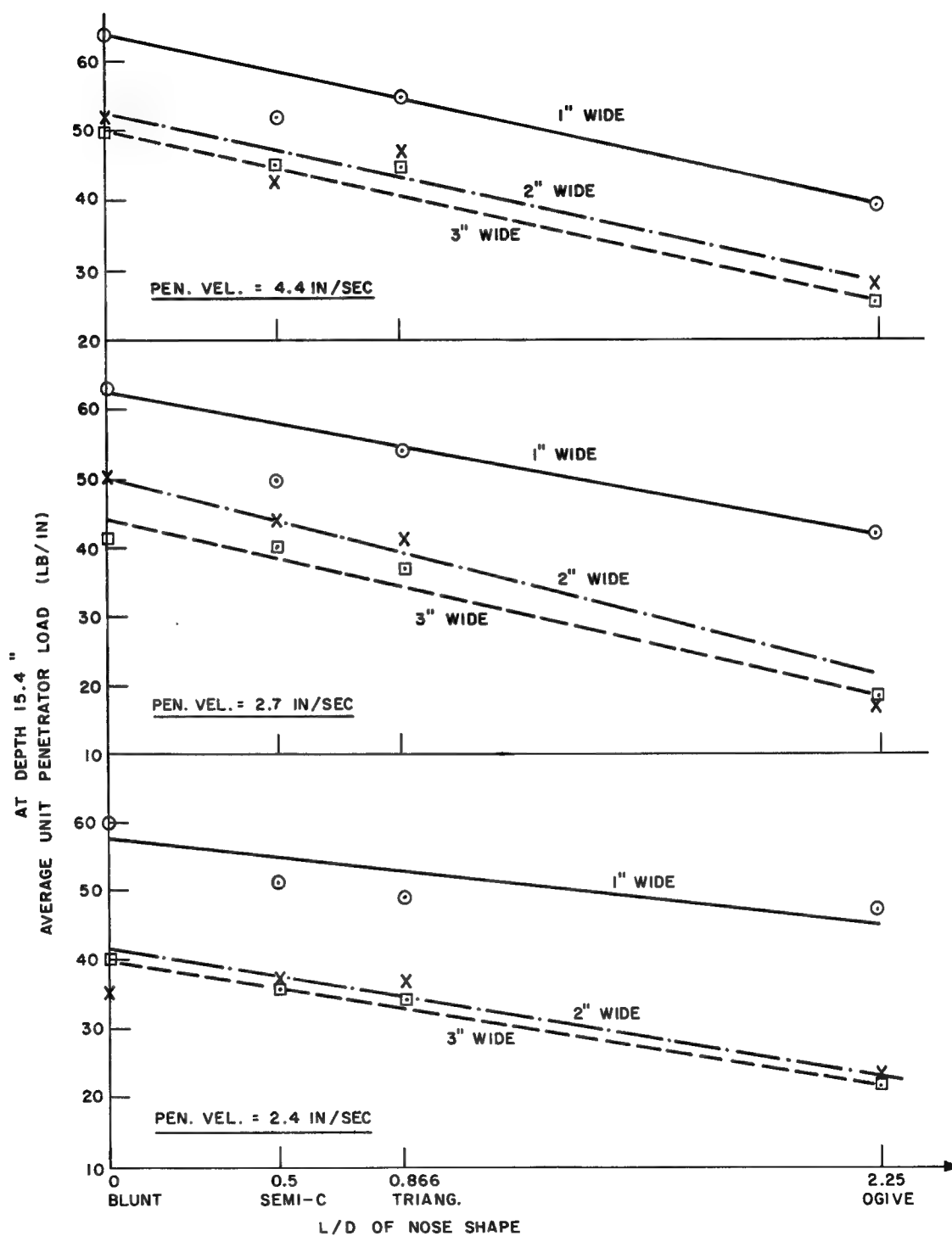


Figure 18. Unit Resistance vs Nose Shape for the Constant Velocity Two-Dimensional Tests

b. Dynamic Penetration Tests --

(1) Steel needle bearing roller penetration tests: Two dynamic penetration tests into a two-dimensional target array of steel needle bearing rollers were performed. These tests were performed to correlate the observations made in the low, constant velocity penetrations described above to high velocity penetrations. In this series, the velocity generator used was a light gas gun and the target tank and medium were the same that were used in the low constant velocity series. Motion pictures of the penetration were taken at a rate of 1000 frames per second. Figure 19 shows the test set-up used.

The first shot had a projectile impact velocity of 225 fps. A severe shear zone developed, in addition to a slip surface, well beneath the projectile. The medium above the surface moved as a rigid body and maintained the respective orientation of the painted grid lines. However, as the crater formed, the slip plane became a barrier beyond which no particles of the medium were thrown out by the impact. Thus, it could be assumed that the locking bonds of the medium which moved as a rigid body along the slip plane had been weakened, while those particles beneath the plane remained strong and provided a lower limit to crater size.

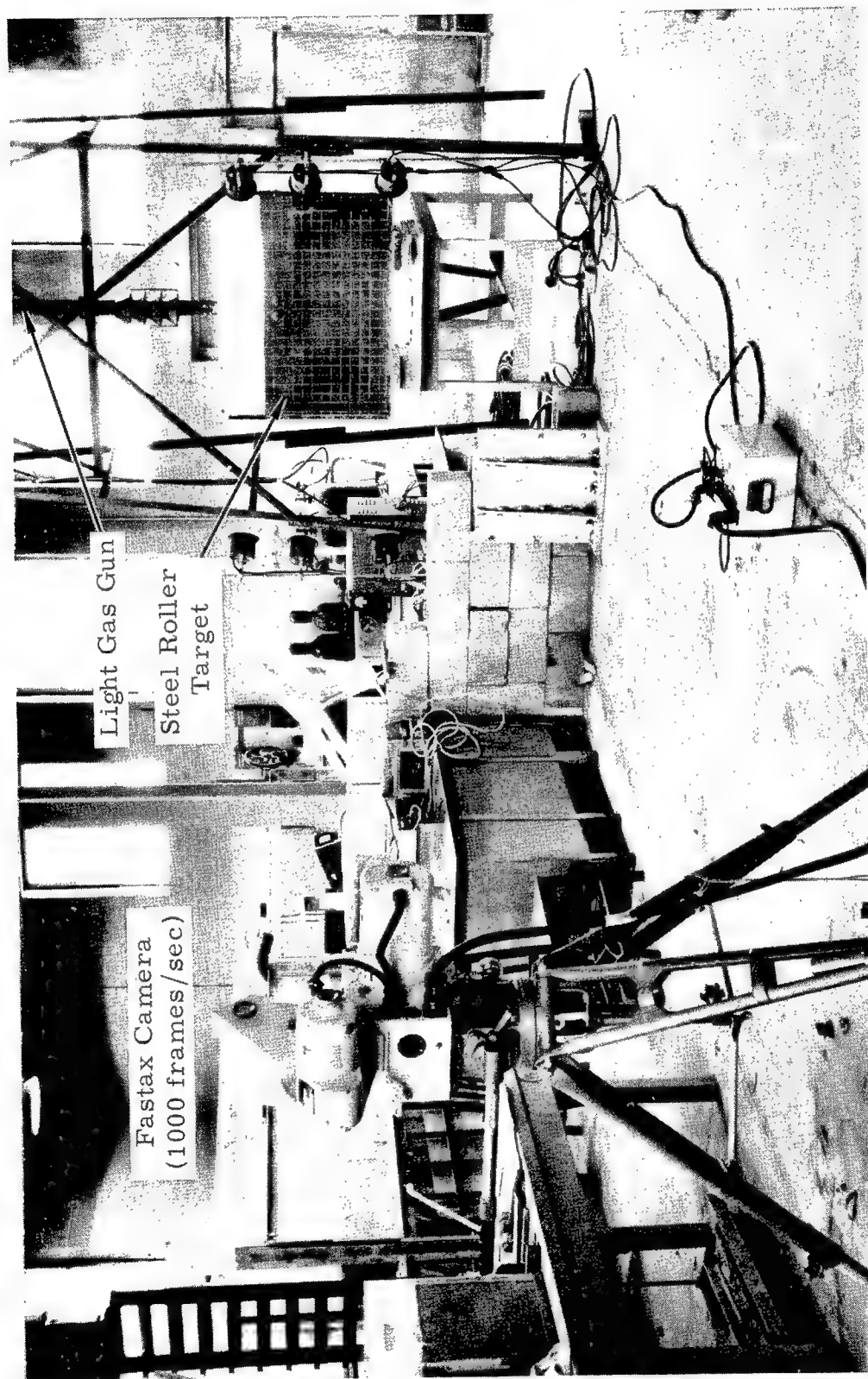


Figure 19. Test Setup for High Speed Penetration Test Into Steel Roller Target

The photographic coverage of the shot conducted at 350 fps was not as good as the 225 fps shot coverage, and the existence of a defined slip surface could not be determined.

The projectile penetrated about 5 inches into the roller array for both impact velocities. No scratching of the Plexiglas container walls could be seen, so it can be assumed that the entire deceleration effort was provided by the medium itself. None of the rollers in the area of the container walls were disturbed, so it is not believed that the container afforded false boundary conditions. The strength of the deceleration forces is demonstrated by the severe plastic deformation of the steel projectile shown in Figure 20. At the time of impact, the projectile started to tumble because of its short length and because it did not impact exactly perpendicularly. The most intense deceleration occurred within the first half inch of penetration. It is quite evident that the entry phase deserves considerable attention in the penetration problem analysis.

In the low constant velocity penetrations, the penetration force during the first half inch of penetration was very low. For this reason, it is not believed that resistance force correlation between low velocity and high velocity shots can be made.

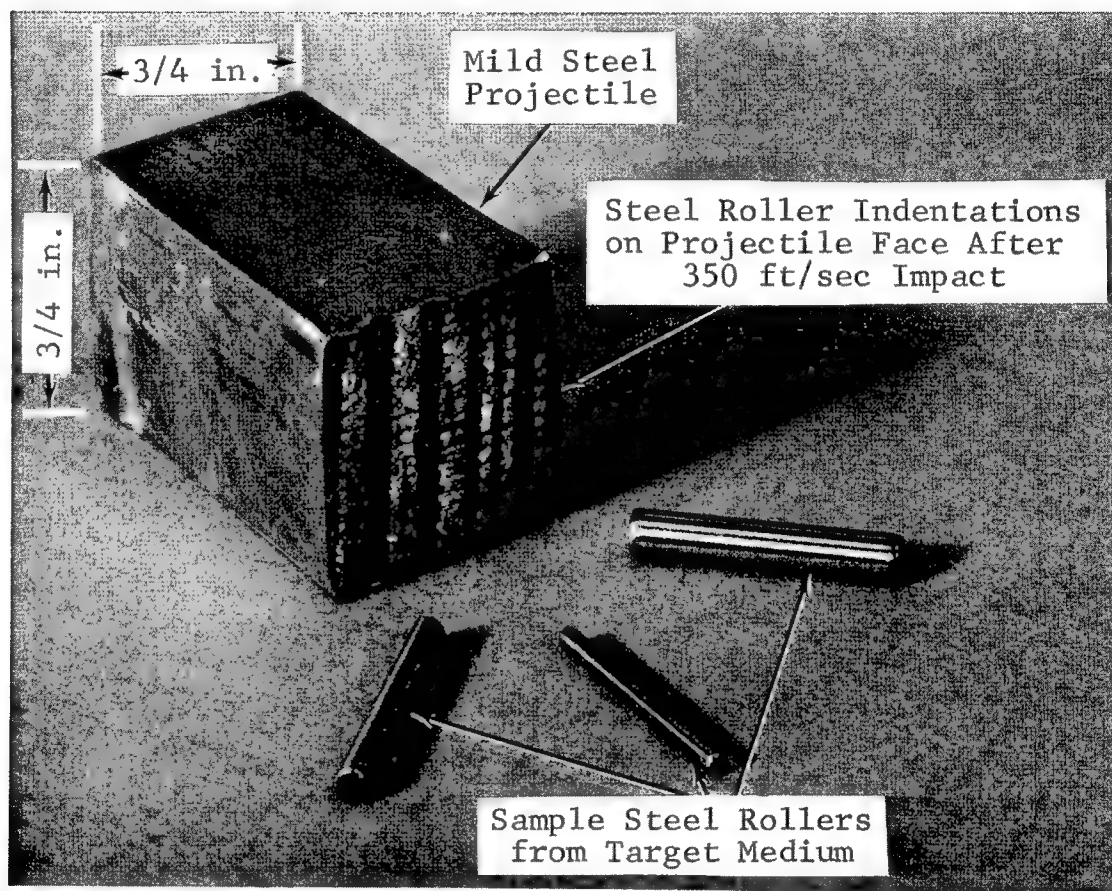


Figure 20. Light Gas Gun Projectile After Impact Into Two-Dimensional Steel Roller Target

Figures 21 through 28 show individual frames from the high speed movies taken of this test series. The displacements and motions of the target material particles during and after the projectile penetration can be seen.

The velocity of the particles within the target medium during the penetration event is quite small; in most cases examined, it was about one-fifth the magnitude of the penetrator velocity. In two high velocity penetrations (350 and 225 fps) into the roller bearings, relatively few particles in the general area of the penetration event were affected until after the projectile stopped. At that time, rollers were thrown out of the medium at a velocity about one-fifth that of the impacting projectile velocity. Only a few individual rollers could be followed in the motion pictures of the event, but their exit velocities appeared to be quite similar in magnitude.

Further, in this test series, the particles were not raised a large distance. By far the greatest amount of energy available for the penetration process is required to break the bonds of the locking granular material and to continue the shearing process. For this reason, it is proposed that in any preliminary theory of medium failure during a penetration event, only the shearing action need be considered. The greater sophistication resulting from inclusion of terms to account

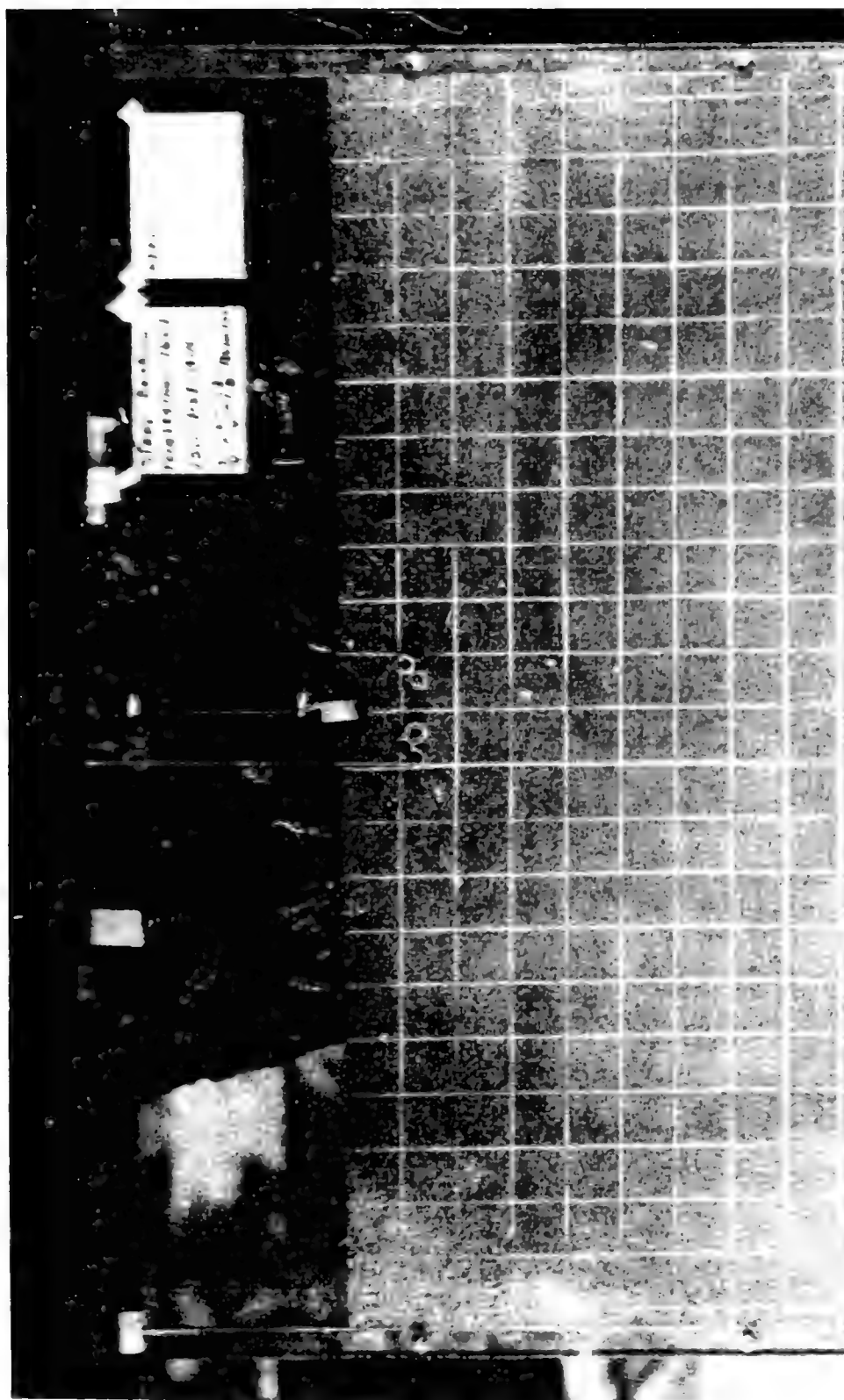


Figure 21. High Speed Movie Frame of Dynamic Penetration Into
Steel Roller Target - Time 0.0006 Second After Impact

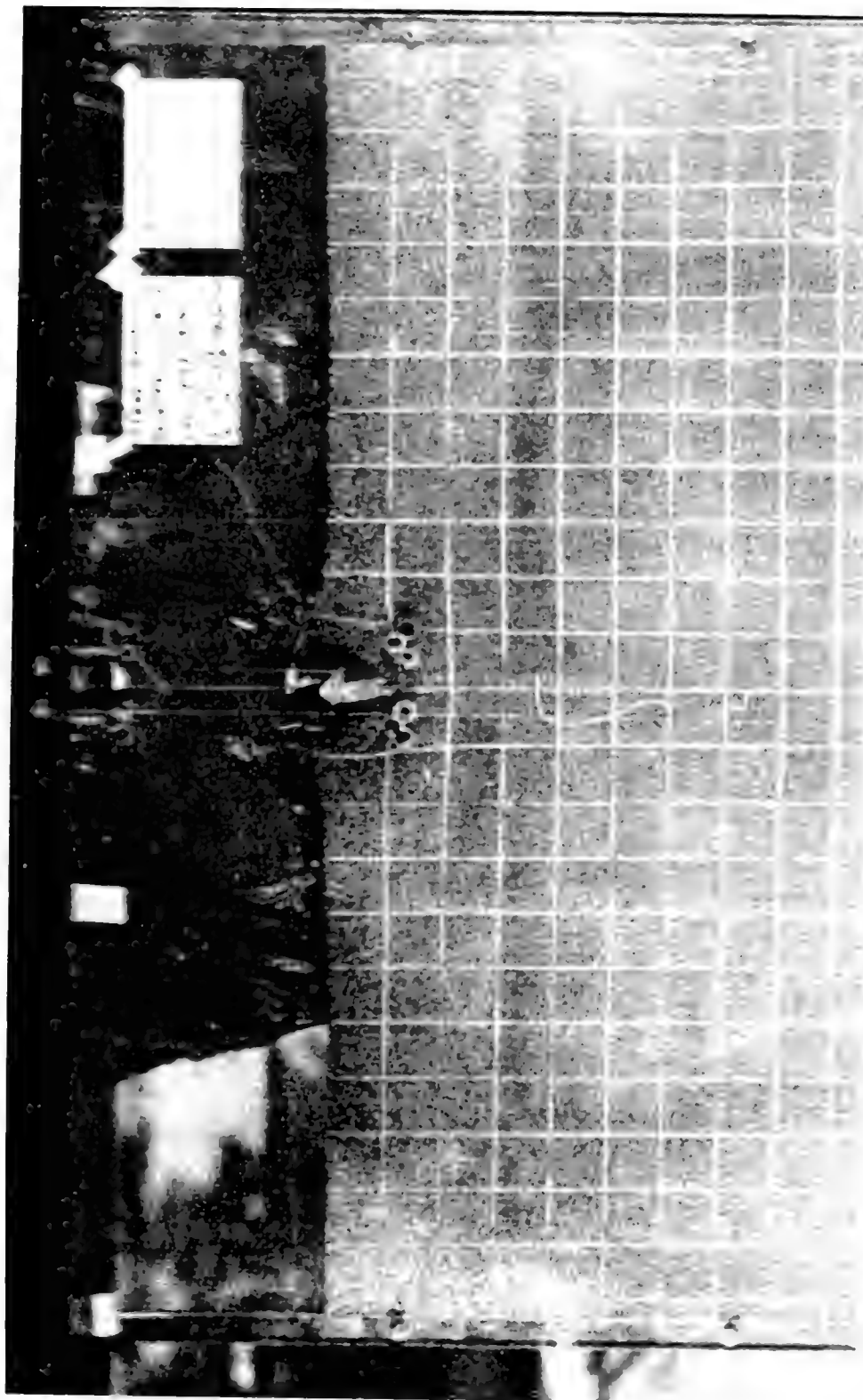


Figure 22. High Speed Movie Frame of Dynamic Penetration Into
Steel Roller Target - Time 0.0036 Second After Impact

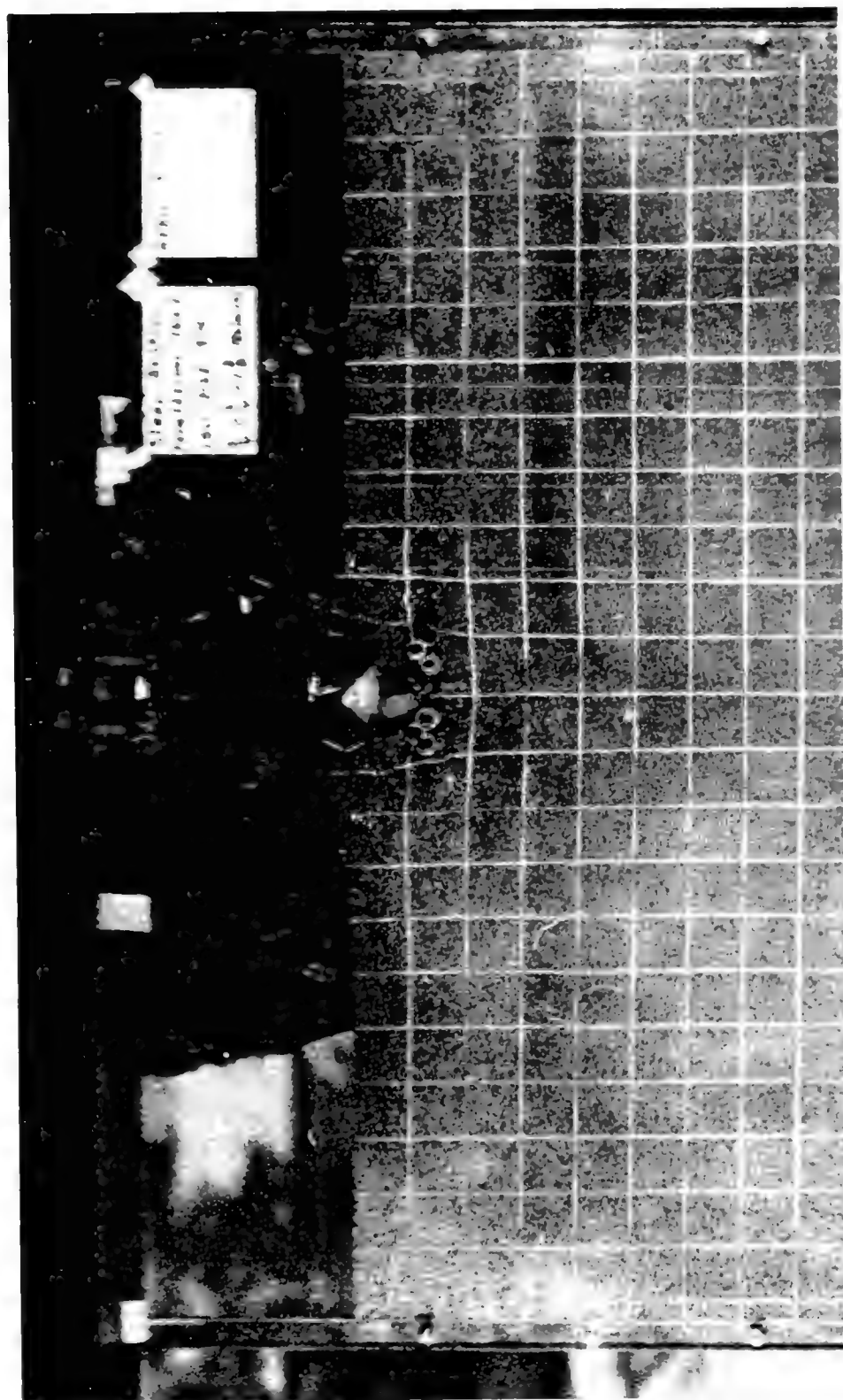


Figure 23. High Speed Movie Frame of Dynamic Penetration Into
Steel Roller Target - Time 0.0066 Second After Impact



Figure 24. High Speed Movie Frame of Dynamic Penetration Into
Steel Roller Target - Time 0.0096 Second After Impact



Figure 25. High Speed Movie Frame of Dynamic Penetration Into
Steel Roller Target - Time 0.0196 Second After Impact

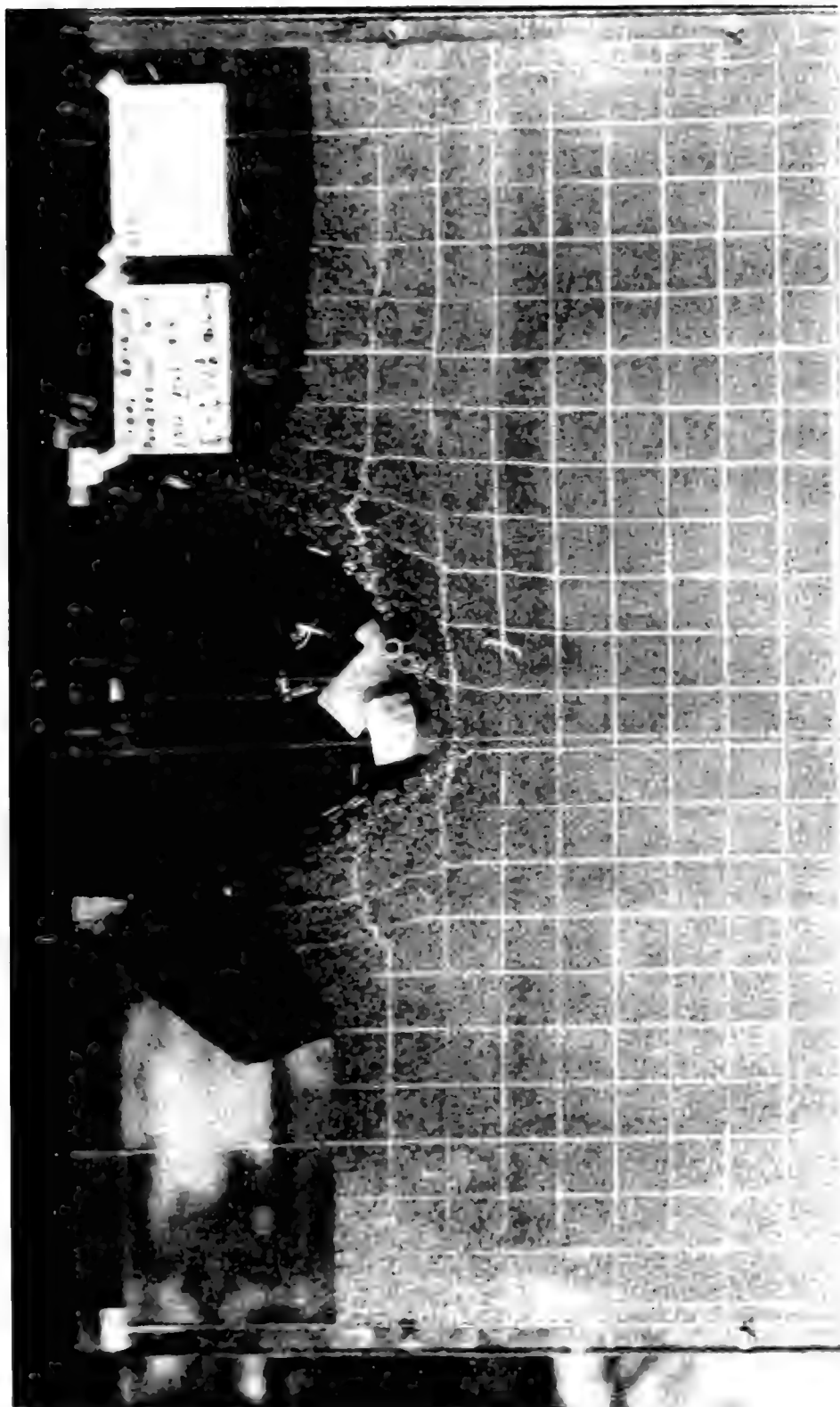


Figure 26. High Speed Movie Frame of Dynamic Penetration Into
Steel Roller Target - Time 0.0566 Second After Impact

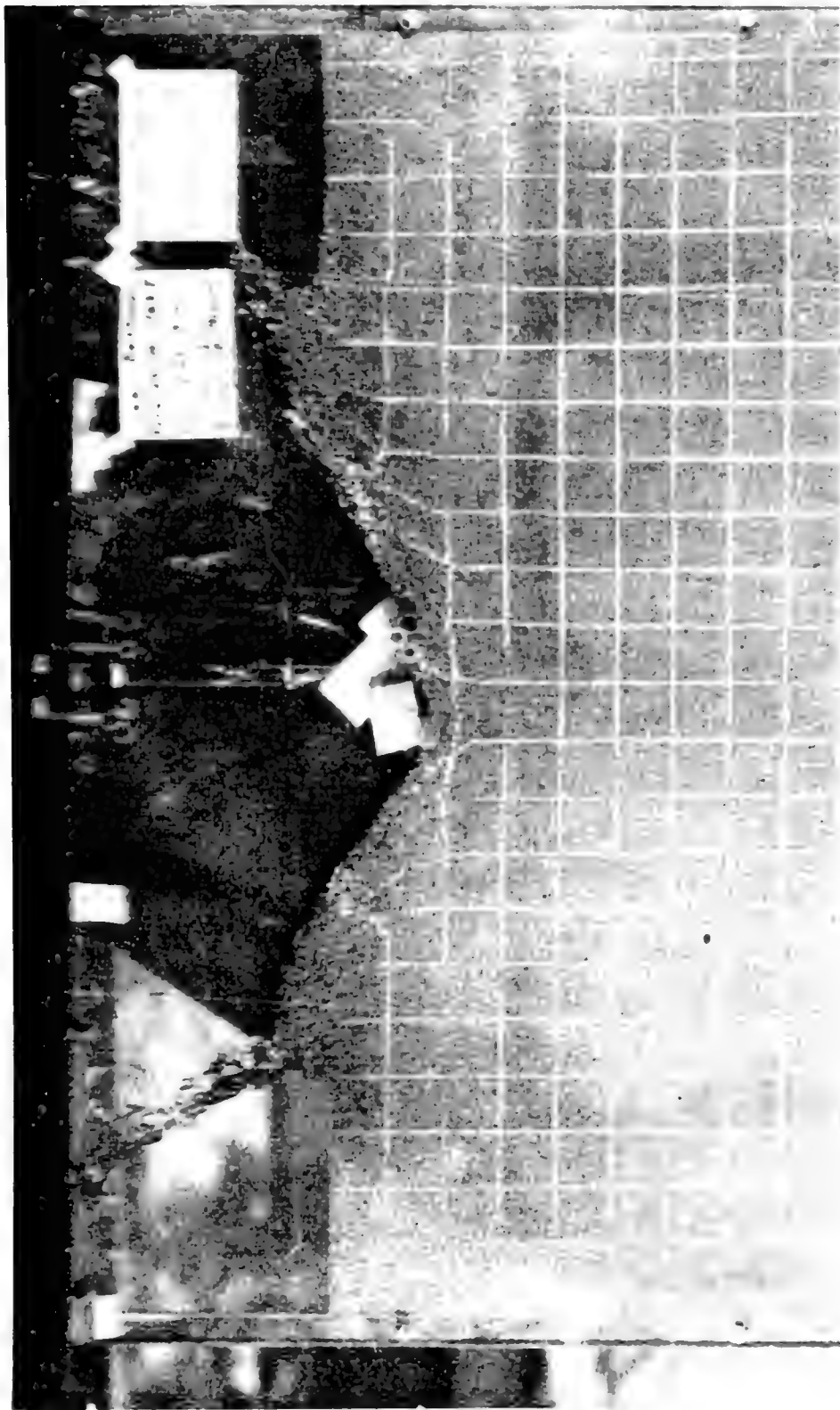


Figure 27. High Speed Movie Frame of Dynamic Penetration Into
Steel Roller Target - Time 0.2066 Second After Impact



Figure 28. High Speed Movie Frame of Dynamic Penetration Into
Steel Roller Target - Time 0.3066 Second After Impact

23 for particle exit velocities, etc., should be added only after a much better grasp of the basic shearing action is attained.

(2) Moist, bulked silt penetration tests: Four low velocity penetration tests were made into a moist, bulked silt target. A direct acting impact mechanical actuator was used on this series. The target tank used was similar to that described for the constant velocity steel roller penetration tests. The moist silt target material was placed in the target tank in a bulked state. The density of the target material was uniform throughout the target tank. The target was constructed by placing measured weights of material in measured volumes between the Plexiglas plate.

High speed movies were taken of the penetration event into the bulked silt. Figures 29, 30, and 31 are prints of individual frames from the high speed movies taken during this series. The decided difference in the target material deformation pattern observed in similar tests into dense, granular materials can be clearly seen in these photographs.

(3) Dry Ottawa sand penetration tests: A series of penetration tests were performed into a target of clean, dry Ottawa sand that passed a 20-mesh screen and was retained on a 30-mesh screen. Nineteen tests were included in this series.



Figure 29. Initial High Speed Movie Frame of Dynamic Penetration Into Bulked Silt Target

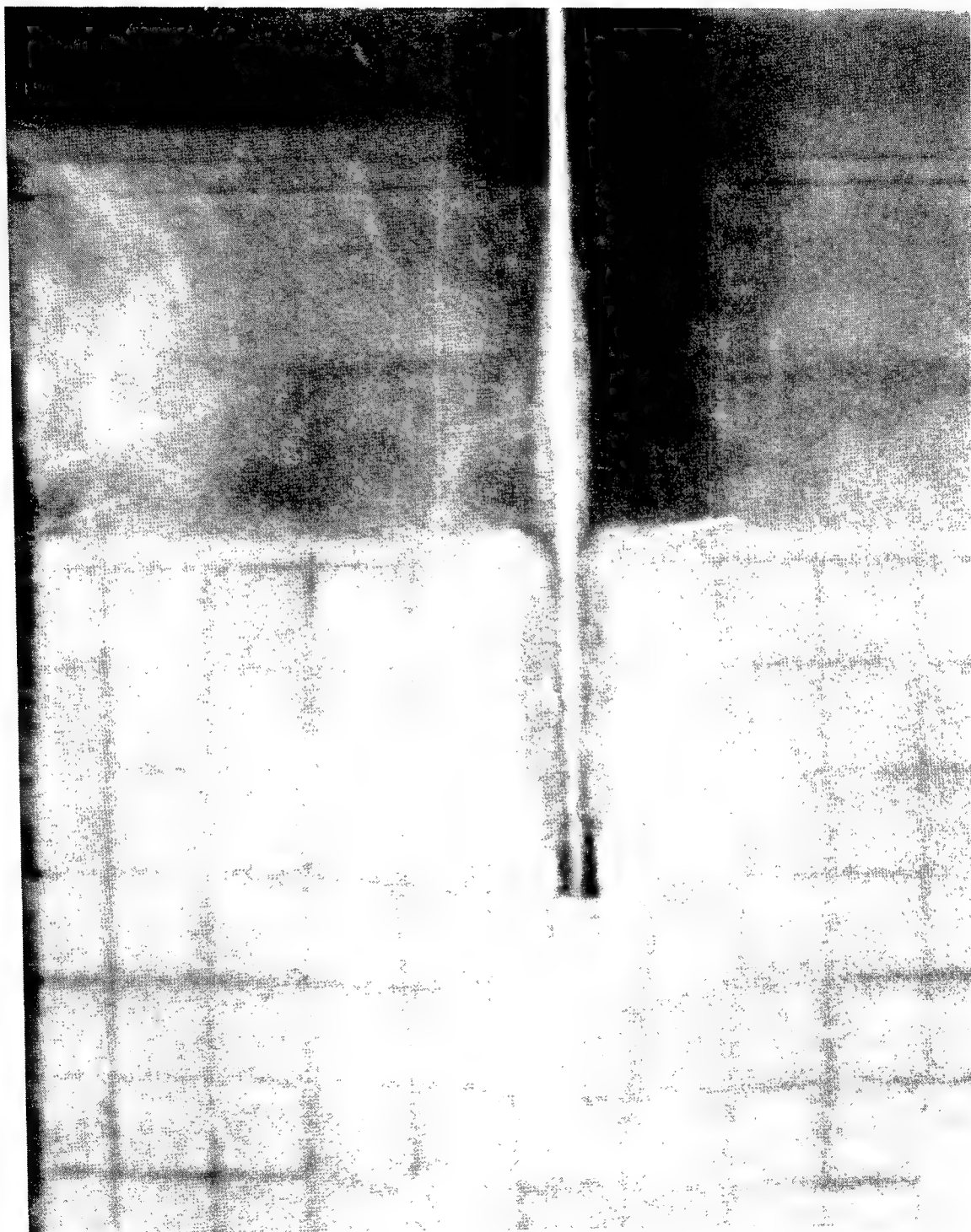


Figure 30. High Speed Movie Frame of Dynamic Penetration
Into Bulkied Silt Target

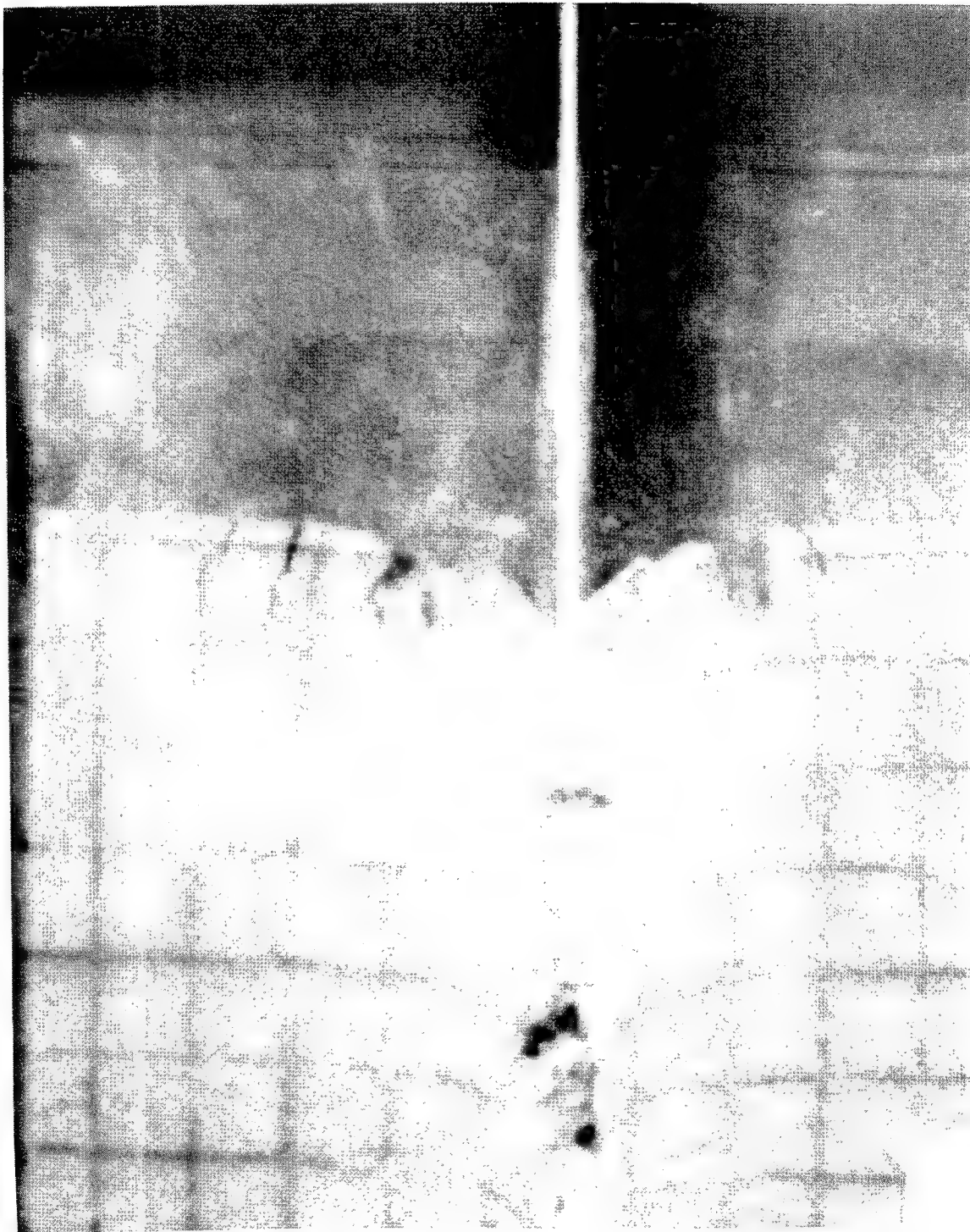


Figure 31. Final High Speed Movie Frame of Dynamic Penetration Into Bulk Silt Target

24 A light gas actuator was used to propel the projectile for this series. The target tank was the same as described earlier. Figure 32 shows the test setup used.

The test series included projectile impact velocities from 106 feet per second to 478 feet per second. Two sizes of projectiles were used; $3/4"$ x $3/4"$ in cross-section and $1-1/2"$ x $1-1/2"$ in cross-section. All projectiles weighed 0.51 pound. The density of the Ottawa sand target material was uniform for each individual test and was varied between 105 and 112 pounds per cubic foot.

High speed movies were taken of each test run. Figures 33 and 34 show individual frames from the movies taken. As can be seen, the deformation patterns observed are quite similar to those shown in the constant velocity penetration into steel needle bearing rollers shown earlier.

(4) Gelatin penetration tests: A series of penetration tests into a target of gelatin were performed. Gelatin was selected as a target material to simulate a soft, viscous, incompressible cohesive material such as saturated clay. Gelatin is a double-refracting material. A study was begun in which photoelastic means were used to determine the internal stresses induced by penetration. A large polariscope (Figure 35) was constructed and used in this study. Thirty-three penetration tests into this target material were made.

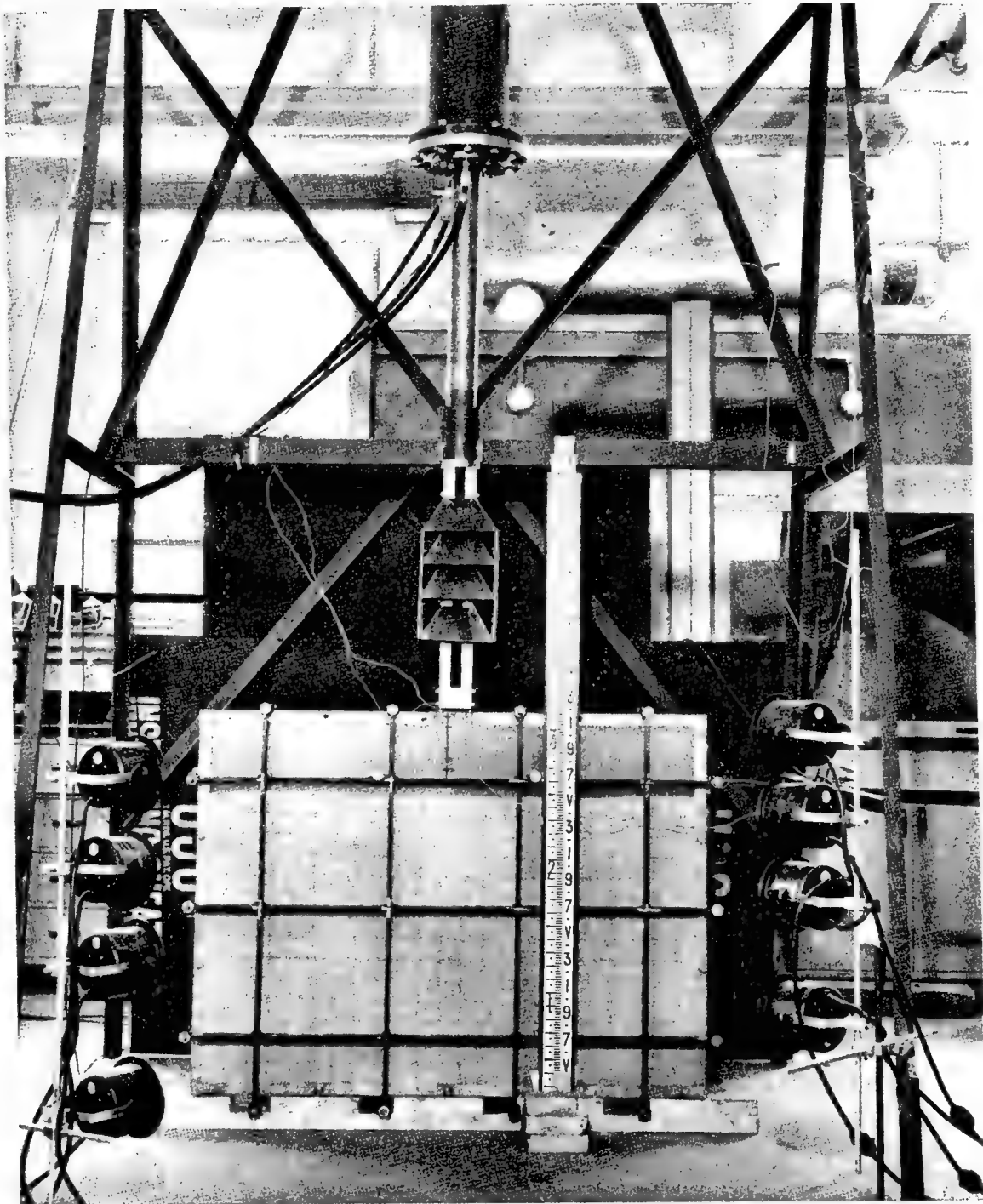


Figure 32. Laboratory Test Setup for Dynamic Penetration
Into Ottawa Sand



Figure 33. Initial Frame of High Speed Movie
Showing Dynamic Penetration Into Dry
Ottawa Sand



Figure 34. Final Frame of High Speed Movie
Showing Dynamic Penetration Into Dry
Ottawa Sand



Figure 35. Laboratory Test Setup for Penetration Test Into Gelatin
Showing Large Polariscope Used

A linear mechanical actuator was used to propel the projectiles. The same target tank as used in the previously described needle bearing roller tests was used for this series. Projectile impact velocities were varied from 110 feet per second to 395 feet per second. The same two projectile sizes as used in the Ottawa sand tests described above were used in this series. The gelatin was of uniform density for each individual test. Due to the difficulty of maintaining uniform laboratory temperature, it was not possible to hold the gelatin consistency exactly constant from test to test.

High speed movies of the penetration into the gelatin were taken through the large polariscope used in this test series. Figures 36 through 38 show individual frames from one of the high speed movies taken. These photos show the double-refracting effects in the gelatin caused by the entrance of the projectile. The resulting pictures were of such poor quality that the stress field could not be analyzed. The principal problem was that not enough light could be transmitted through the polariscope in the short exposure time required for 1000 frames per second movies. Three different lighting systems were tried and camera speeds up to 25,000 frames per second were employed. It is hoped that this work can be extended in the future using a series of exploding wires as light sources. Nevertheless, the mechanism of failure could be observed with these pictures. They show that there was never

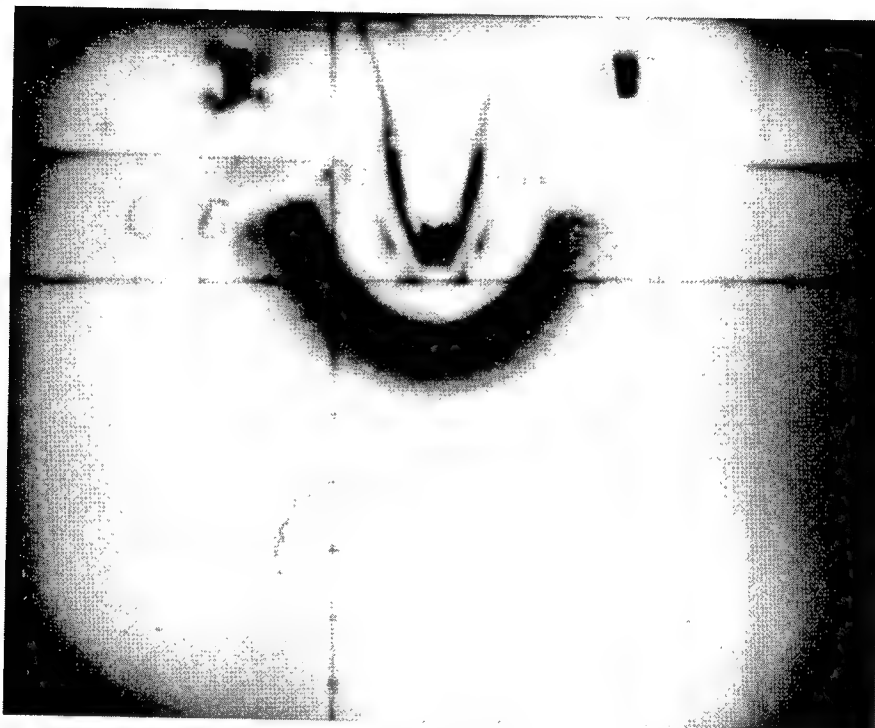


Figure 36. Initial Frame of High Speed Movie
of Dynamic Penetration Into Gelatin as
Seen Through the Polariscope

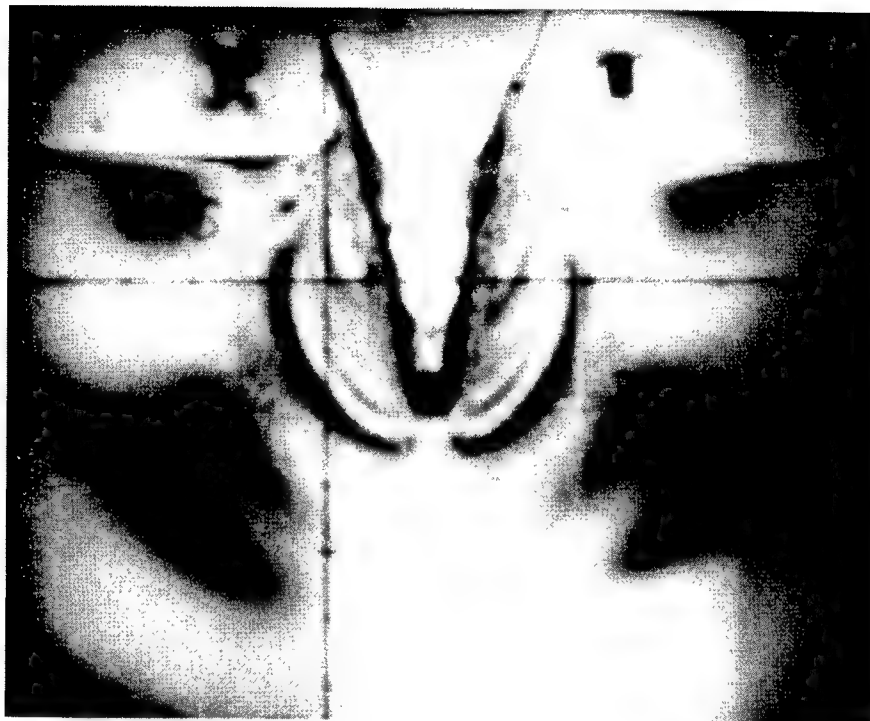


Figure 37. Intermediate Frame from High Speed Movie
of Dynamic Penetration Into Gelatin as Seen
Through the Polariscope



Figure 38. Final Frame from High Speed Movie
of Dynamic Penetration Into Gelatin as
Seen Through the Polariscope

any side friction on the projectile during the event except when the projectile tumbled. The stresses were low except near the front of the projectile and along the sides of the projectile. The initial shock wave in the target outran the projectile. Once the gelatin yielded at the surface, the energy going into the shock wave was terminated. The direction of yielding and flow at any instant of time was similar to the sand and needle-bearing tests.

Three-Dimensional Laboratory Tests

a. Water Tests -- A series of 11 experiments was conducted using water as the target medium. It was reasoned that the behavior of some soils in their saturated states might approach that of water. Most natural deposits of soil are mixtures of soil particles, air, and water. Saturated clays of low density could possibly be characterized as a viscous fluid during shear flow; thus, water penetration should give a lower bound on the resistance to penetration for incompressible soils.

The model projectile used in these tests was 1-1/2 inches in diameter, 2-1/4 inches long and weighed 1/2 pound. It was shot downward into a glass tank of water and high speed photography was used to record the motion. In one case, the projectile was allowed to fall free.

The velocity generator was the light gas gun used for the two-dimensional tests. The water tank was about 2 feet square and about six feet deep. The entrance velocities used for these 11 tests varied between 16 and 218 feet per second. The position of the projectile was plotted versus time by using the timing marks on the high speed photograph frames. By numerically differentiating the motion vs. time plot, velocity was calculated. By differentiating velocity vs. time, acceleration was calculated. A typical set of data is shown for test number 2 in Figure 39. A picture of the projectile during water penetration is shown in Figure 40. In all cases, there was a cavity around the projectile sides and rear, and this cavity stayed with the projectile until it came to rest on the bottom of the tank. Steady-state hydrodynamic theory assumes the resisting force to movement is proportional to the square of the velocity, or that the velocity squared divided by the deceleration is equal to a constant for a given projectile. In all water tests, the average deceleration was not proportional to the entrance velocities. Also for any individual test, the deceleration was not proportional to the velocity squared at any instant of time. In the data shown for test number 2, the velocity squared divided by the deceleration increased 36 percent in the 10 milliseconds it took the projectile to travel $12\frac{1}{4}$ inches. This is typical of all of the tests.

WATER TEST
 DIAMETER OF PROJECTILE — 1.5 INCHES
 LENGTH OF PROJECTILE — 2.25 INCHES
 WEIGHT OF PROJECTILE — 4.28 POUNDS

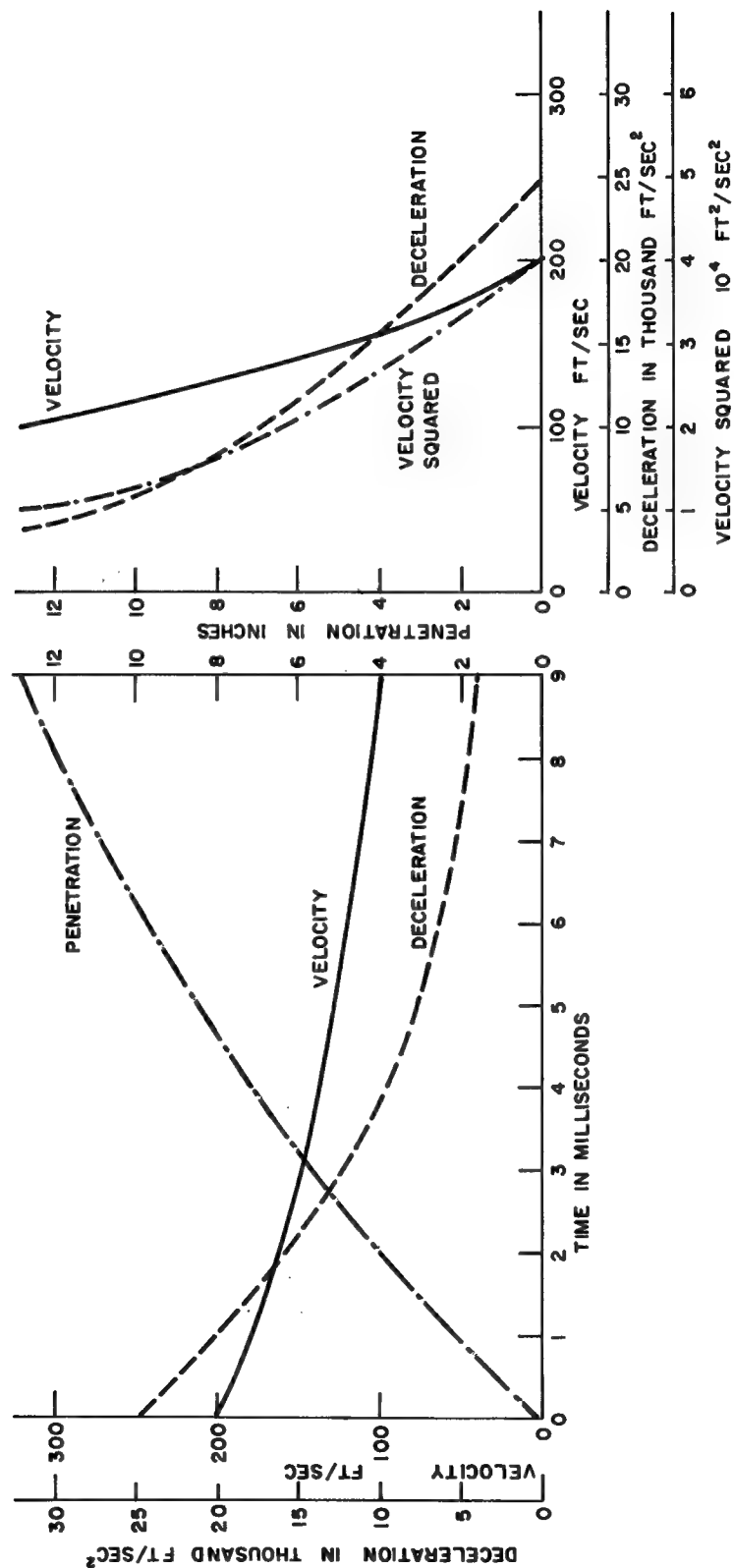


Figure 39. Motion-Time and Motion-Penetration Relations for Water Test No. 2



Figure 40. Frame from High Speed Movie Showing
Dynamic Penetration Into Water

b. Three-Dimensional Sand Tests -- A series of 111 tests was conducted. The tests were similar to the water tests except dry Ottawa sand at various densities was used as the target. Of course, the cameras could not be used to record the motion. At first an attempt was made to measure the deceleration of the projectile directly. Accelerometers were mounted in the projectile, but in only two cases was it possible to record a part of the deceleration time signature since the hard wire connection to the recording unit invariably broke. At the time the tests were being conducted there existed no radio telemetering package small enough to fit into the 1-1/2 inch diameter projectiles, so a microwave system was developed for this study by Dr. Don Thorn of the University of New Mexico to measure displacement versus time during the event. An antenna was placed in the bottom of the soil container. Microwaves were projected upward through the soil and reflected off of the projectile during penetration. There was a phase difference between the projected and reflected signal. The recording system allowed the superimposing of a time signal on the microwave record. The emitted and reflected signals were superimposed causing either cancellation or reinforcement. The time between peaks of reinforcement of signal was measured; then using the precalibrated velocity of the microwaves through the sand, the distance moved during the time interval was calculated. No change of velocity

of the microwaves could be detected when the density of the soil was varied between 99 and 110 pounds per cubic foot. When the projectile stopped, the signal became constant. The distance penetrated was measured. The initial velocity was calculated independently, by measuring the time increment that elapsed for the projectile to break two carbon leads spaced a known distance apart across the flight path of the projectile before impact. The time increment was measured with a Berkley counter. Working back from the maximum depth of penetration, it was possible to calculate the entrance velocity and total time of trajectory in the soil. In only 11 of the 111 tests was this possible since usually the projectile tumbled during the trajectory. At first the distance time data were numerically differentiated to obtain the velocity and deceleration plot, but this resulted in rough erratic plots so a polynomial was fitted to the depth-time data using a computerized method to best fit the data. These functions were differentiated twice to obtain velocity and deceleration plots. These data for the 11 tests are shown in Figures 41 through 51. The 4 tests in which the unit weight of the soil was 107 lb/cu. ft. are the best tests. In none of these cases was the deceleration proportional to the velocity squared. Because the projectile tumbled, there is no uniform trend in the relationships between deceleration and depth.

UNIT WEIGHT OF SAND — 99 POUNDS PER CUBIC FOOT
 DIAMETER OF PROJECTILE — 0.75 INCHES
 WEIGHT OF PROJECTILE — 0.50 POUNDS

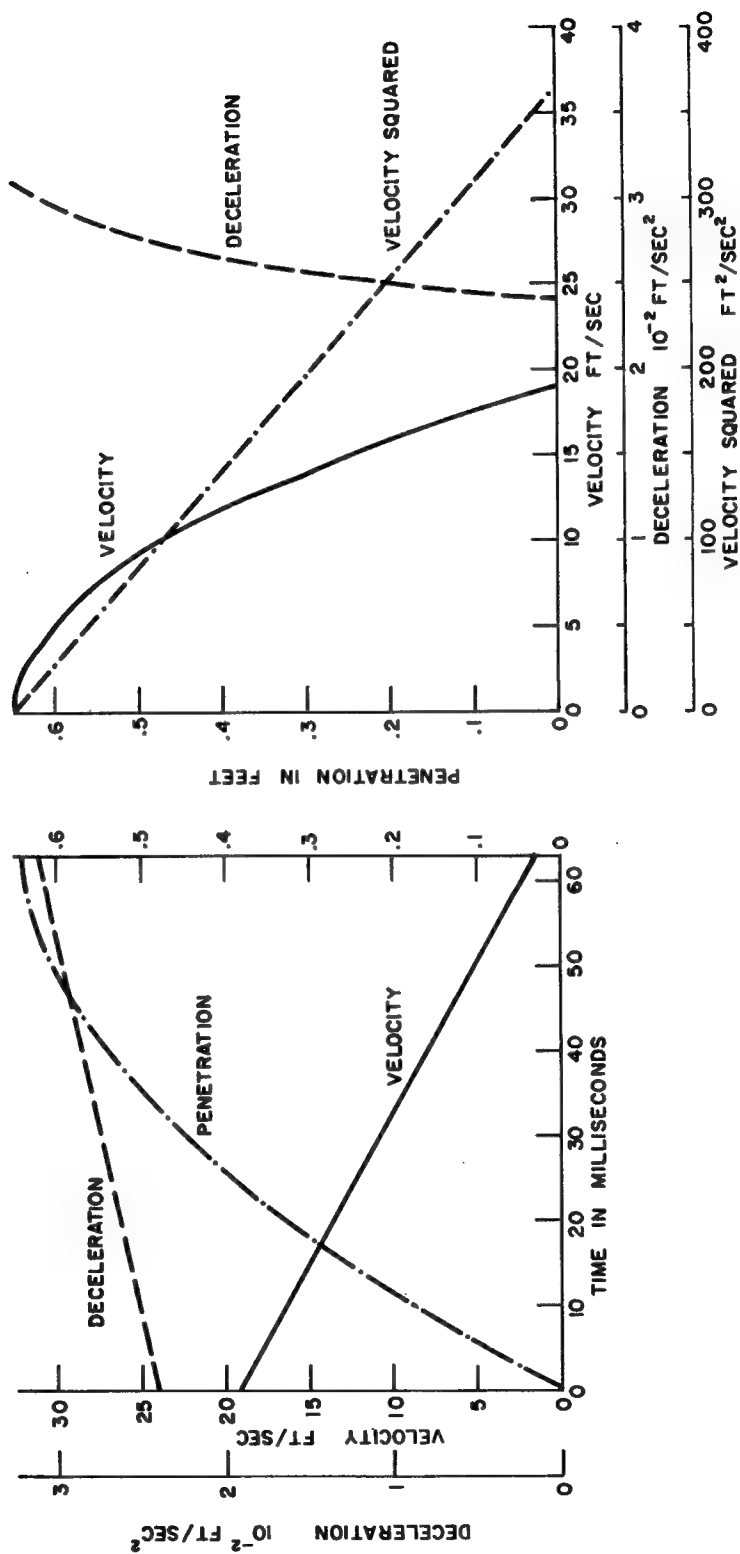


Figure 41. Motion-Time and Motion-Penetration Relations for Test No. (SO)G-IV-10A

UNIT WEIGHT OF SAND — 99 POUNDS PER CUBIC FOOT
 DIAMETER OF PROJECTILE — 0.75 INCHES
 WEIGHT OF PROJECTILE — 1 POUND

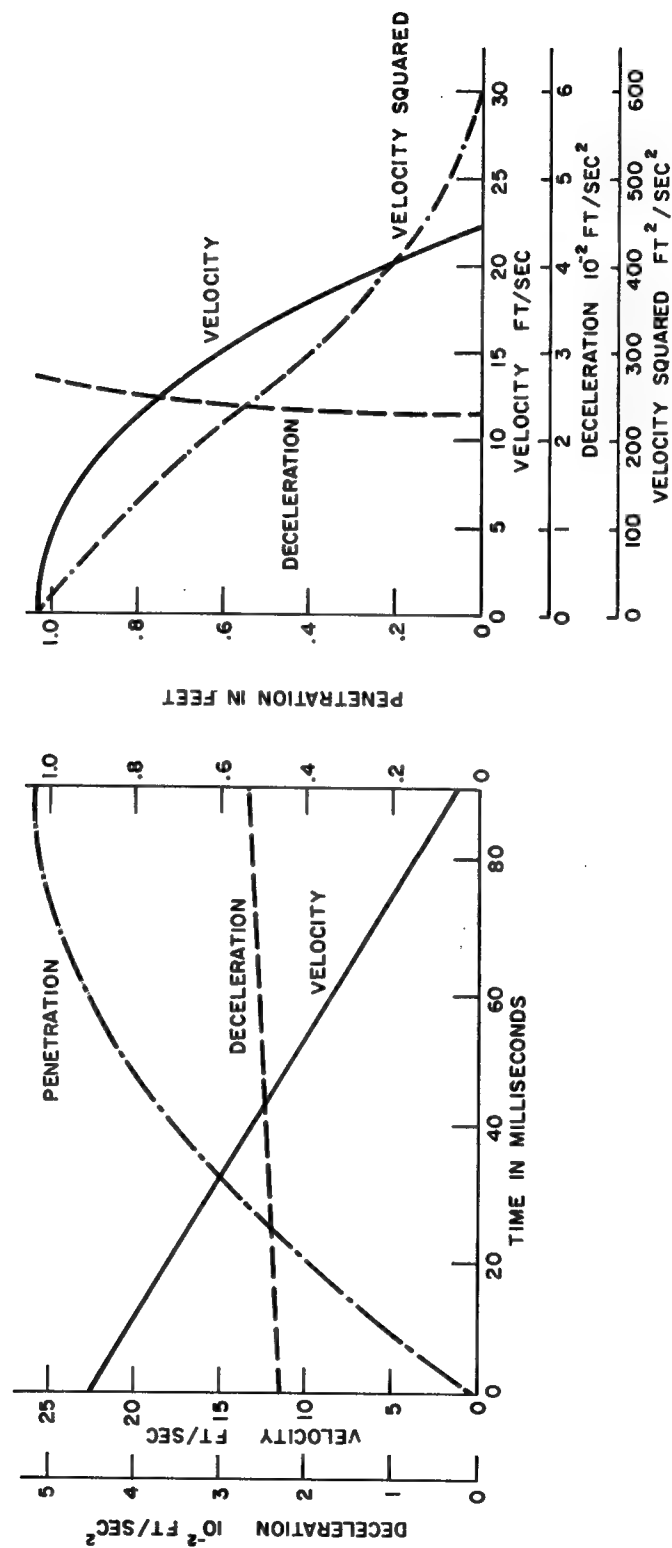


Figure 42. Motion-Time and Motion-Penetration Relations for Test No. (SO)G-IV-11C

UNIT WEIGHT OF SAND—99 POUNDS PER CUBIC FOOT
 DIAMETER OF PROJECTILE—0.75 INCHES
 WEIGHT OF PROJECTILE—2 POUNDS

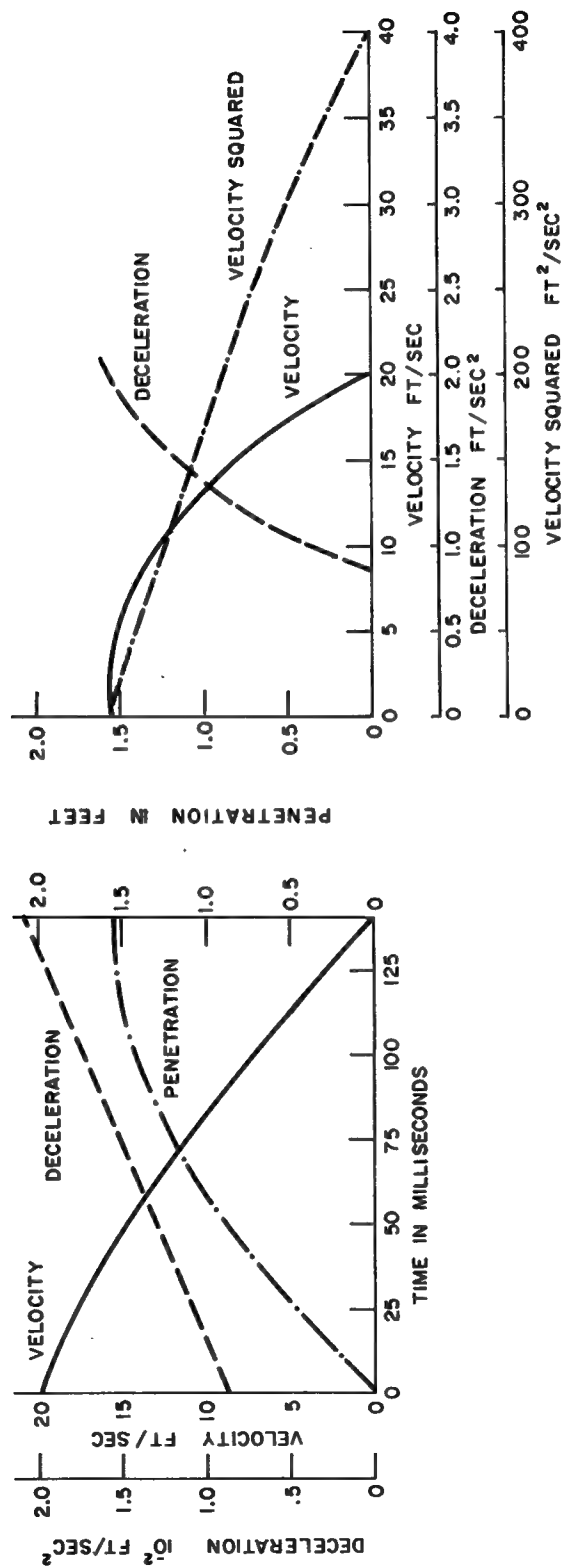


Figure 43. Motion-Time and Motion-Penetration Relations for Test No. (SO)G-IV-12A

UNIT WEIGHT OF SAND—99 POUNDS PER CUBIC FOOT
 DIAMETER OF PROJECTILE—1.5 INCHES
 WEIGHT OF PROJECTILE—2 POUNDS

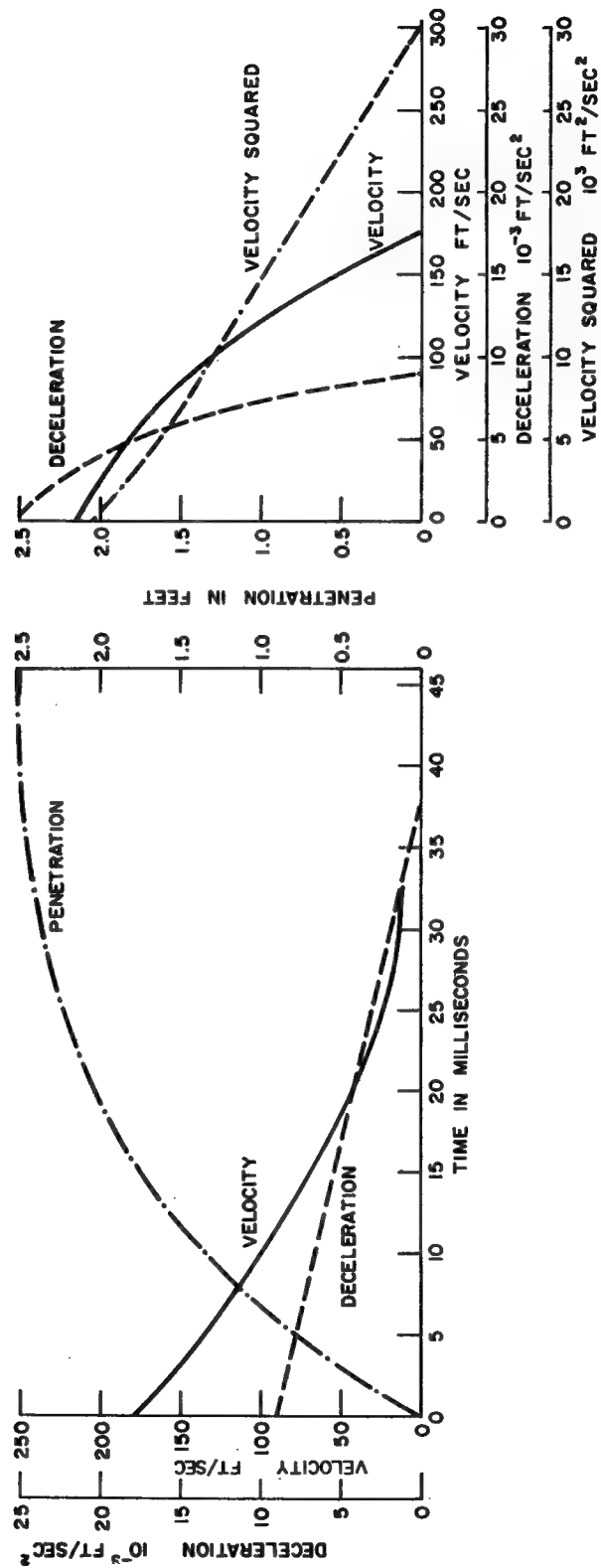


Figure 44. Motion-Time and Motion-Penetration Relations for Test No. (SO)G-IV-60

UNIT WEIGHT OF SAND — 107 POUNDS PER CUBIC FOOT
 DIAMETER OF PROJECTILE — 0.75 INCHES
 WEIGHT OF PROJECTILE — 0.5 POUNDS

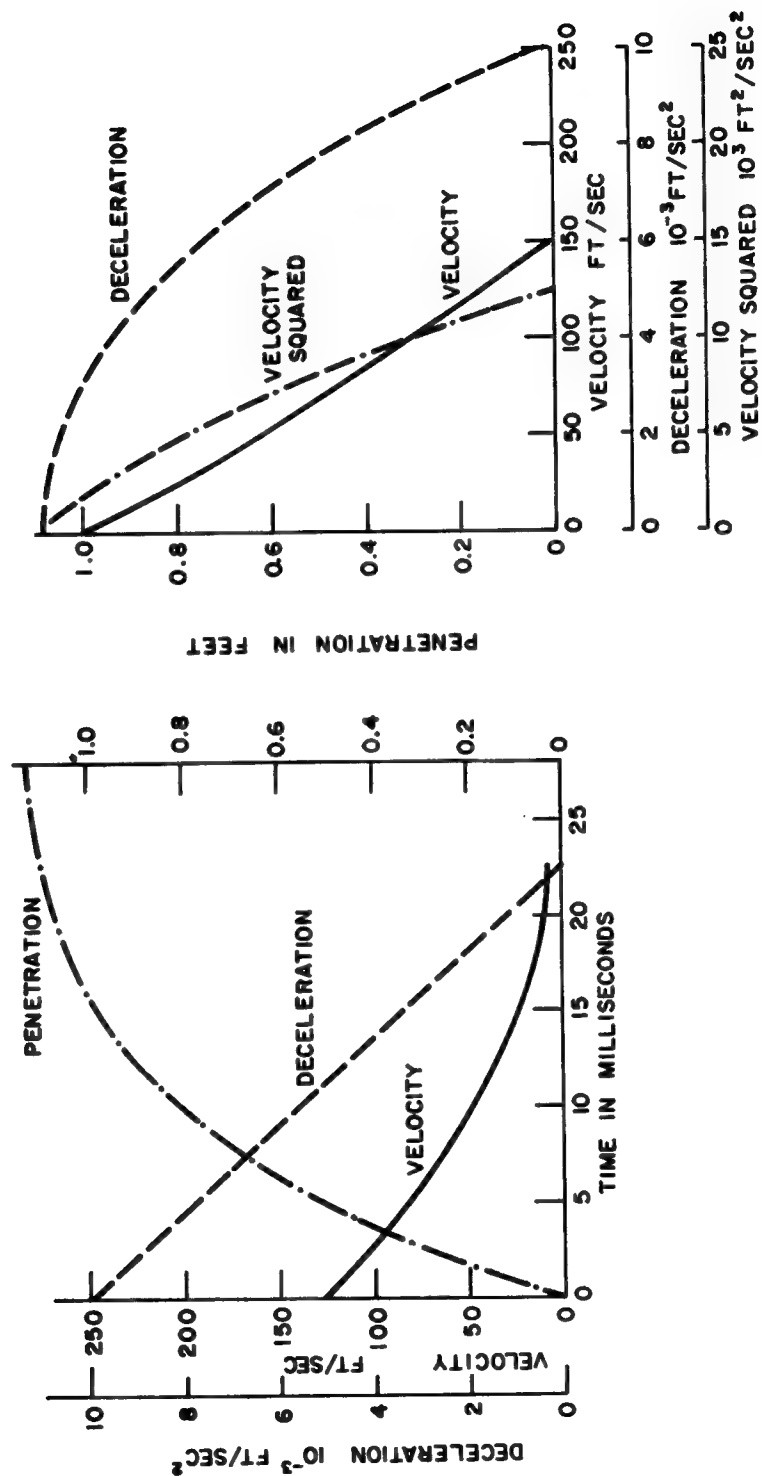


Figure 45. Motion-Time and Motion Penetration Relations for Test No. (SO)G-IV-40A

UNIT WEIGHT OF SAND—107 POUNDS PER CUBIC FOOT
 DIAMETER OF PROJECTILE—1.5 INCHES
 WEIGHT OF PROJECTILE—0.5 POUNDS

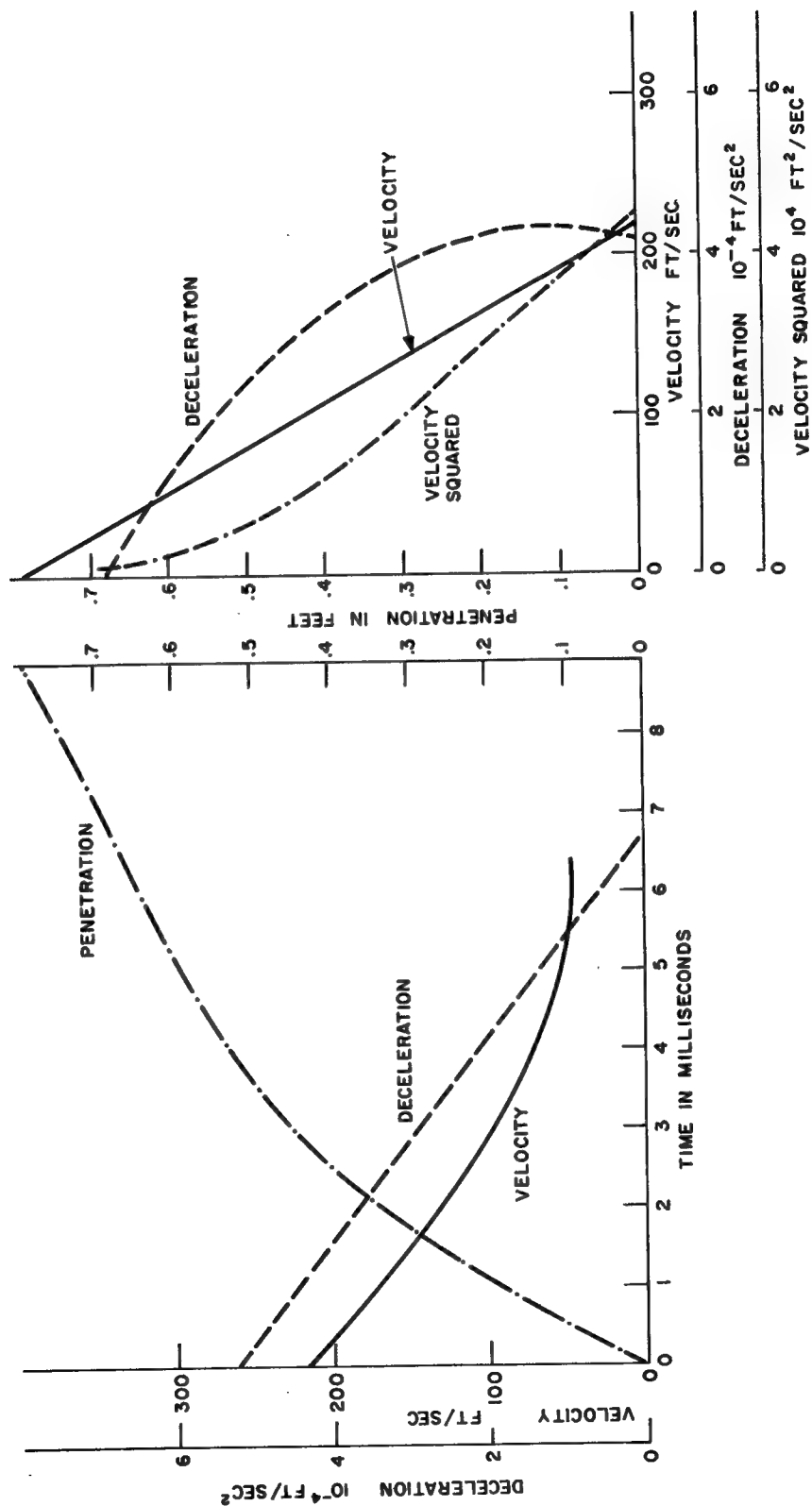


Figure 46. Motion-Time and Motion-Penetration Relations for Test No. 37A

UNIT WEIGHT OF SAND — 107 POUNDS PER CUBIC FOOT
 DIAMETER OF PROJECTILE — 1.5 INCHES
 WEIGHT OF PROJECTILE — 1 POUND

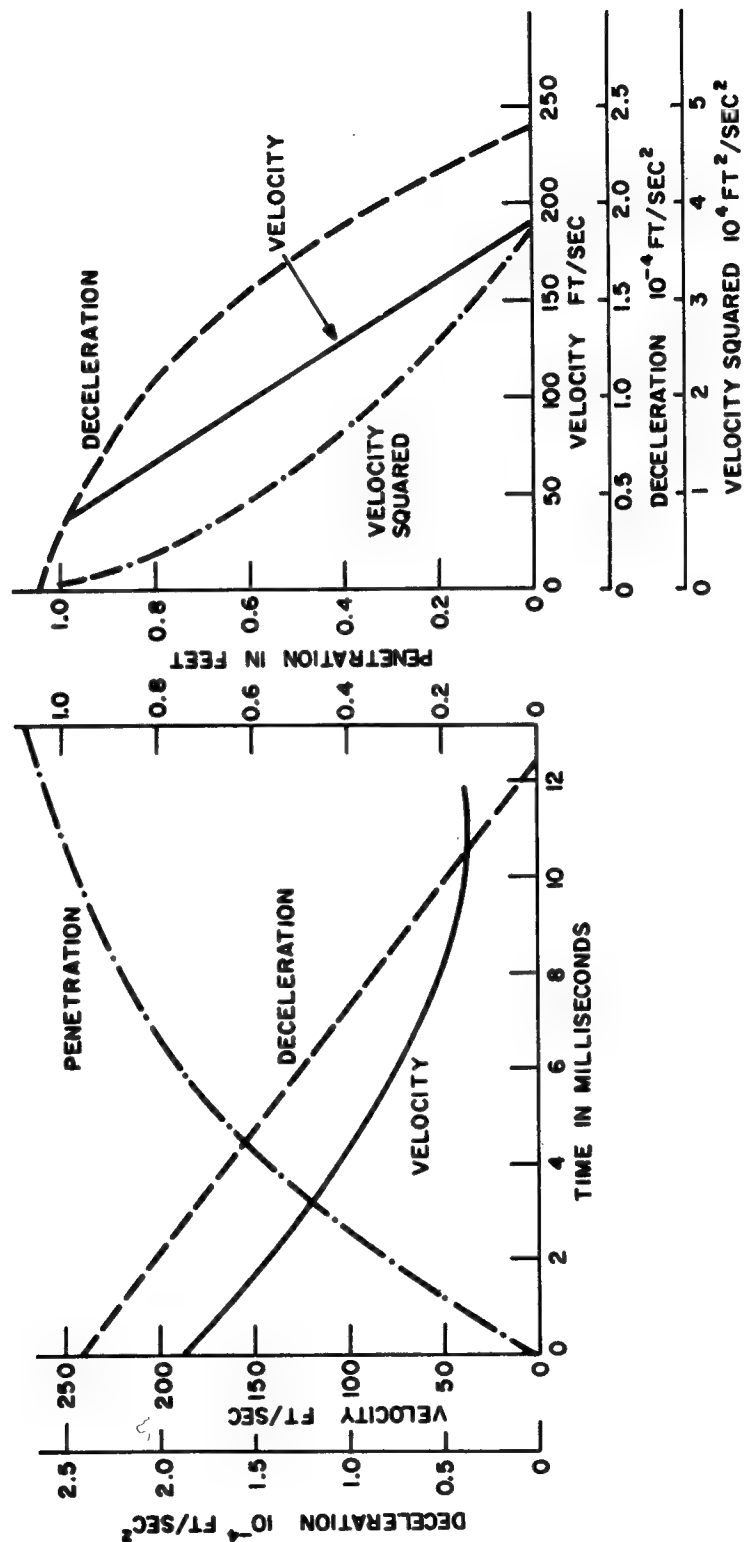


Figure 47. Motion-Time and Motion Penetration Relations of Test No. 38A

UNIT WEIGHT OF SAND — 107 POUNDS PER CUBIC FOOT
 DIAMETER OF PROJECTILE — 1.5 INCHES
 WEIGHT OF PROJECTILE — 2 POUNDS

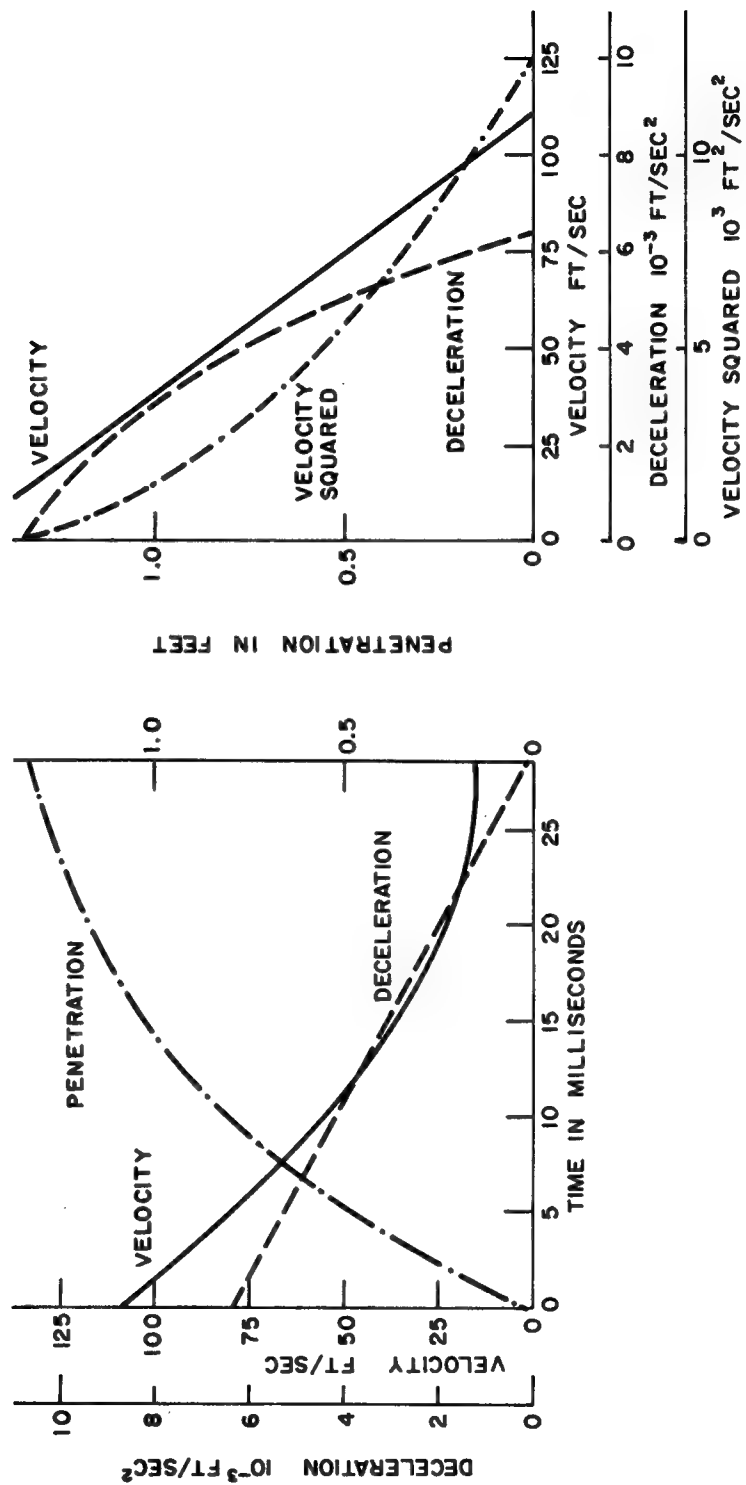


Figure 48. Motion-Time and Motion-Penetration Relations for Test No. 39A

UNIT WEIGHT OF SAND — 110 POUNDS PER CUBIC FOOT
 DIAMETER OF PROJECTILE — 0.75 INCHES
 WEIGHT OF PROJECTILE — 1 POUND

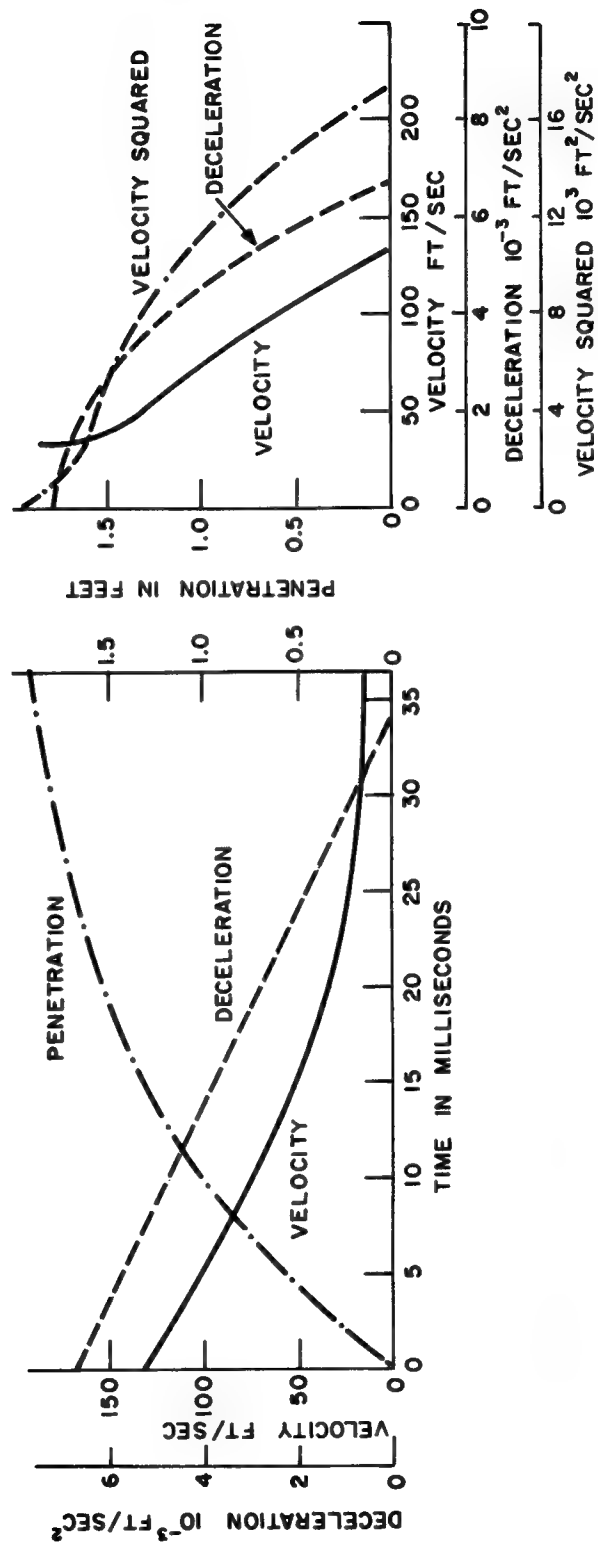


Figure 49. Motion-Time and Motion-Penetration Relations for Test No. 8M

UNIT WEIGHT OF SAND — 110 POUNDS PER CUBIC FOOT
 DIAMETER OF PROJECTILE — 0.75 INCHES
 WEIGHT OF PROJECTILE — 2 POUNDS

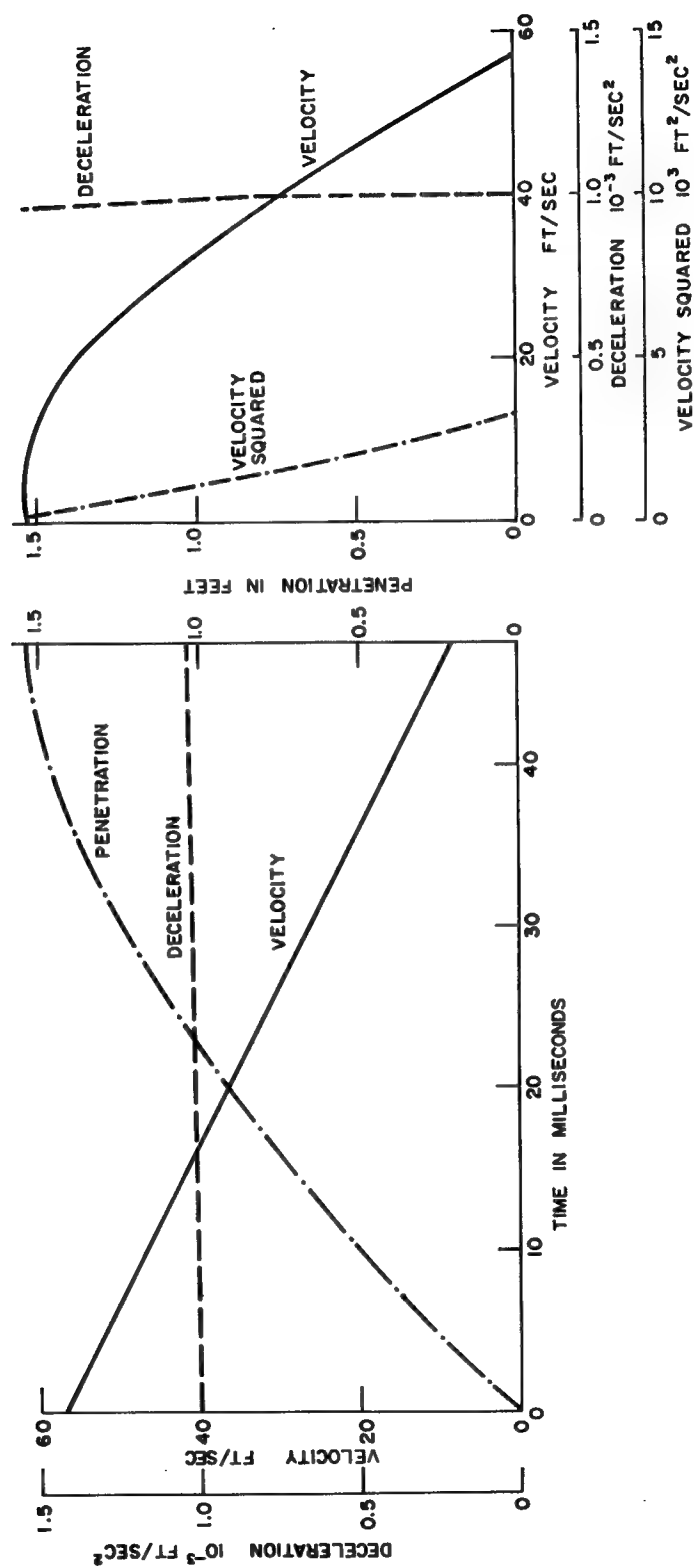
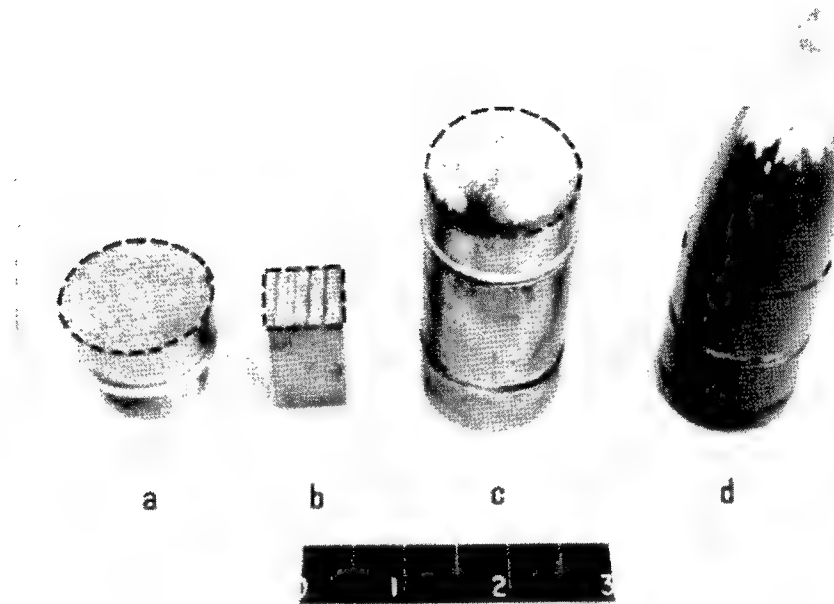


Figure 50. Motion-Time and Motion-Penetration Relations for Test No. 9F

Soil noses were found on the projectile after the tests, and the other comminuted soil was found in the general area where the ejecta fell back in the tank. The soil was warm to the touch immediately after each test.

Later, three different 1-1/2-inch diameter projectiles were shot into Ottawa sand using an explosive-actuated velocity generator and longer projectiles. This system gave a stable trajectory and velocities up to 1100 feet per second. Three different projectiles were used. The shapes of the noses of the projectiles were blunt, hemispherical and 2.2 caliber ogive. In these tests and previous tests, a nose of pulverized sand was found on the blunt nosed projectile and the hemispherical nose projectile, and a partial nose was found on the sharp nosed projectile. Photographs of the projectiles are shown in Figure 52. Photographs of the soil noses are shown in Figures 53 through 55. The sides of the projectile were still smooth after the event. The blunt nosed hard steel projectile was very rough and pitted on the flat face after the event. The sand was hot to touch after the projectile had been fired into it.

c. Horizontal Tests Into Pseudo Soils -- A series of 121 tests was conducted by Division 9226, Sandia Corporation, and the results are discussed briefly here. A radio telemetry system 3/4 inch in



- a. 1-1/2 inch blunt nose taken off cylindrical afterbody of projectile shot into 3-D Ottawa sand target.
- b. 3/4 x 3/4 inch parallelepiped projectile shot into 2-D roller bearing target.
- c. 1-1/2 inch cylindrical projectile with hemispherical nose shot into 3-D Ottawa sand target.
- d. 1-1/2 inch cylindrical projectile with six caliber tangent ogive nose shot into 3-D Ottawa sand target.

Note: --- line of separation. See Figures 53 through 55 for soil noses that adhered to these projectiles.

Figure 52. Photograph of Projectiles After Impact
Showing Nose Distress

UNIT WEIGHT OF SAND — 110 POUNDS PER CUBIC FOOT
 DIAMETER OF PROJECTILE — 1.5 INCHES
 WEIGHT OF PROJECTILE — 2 POUNDS

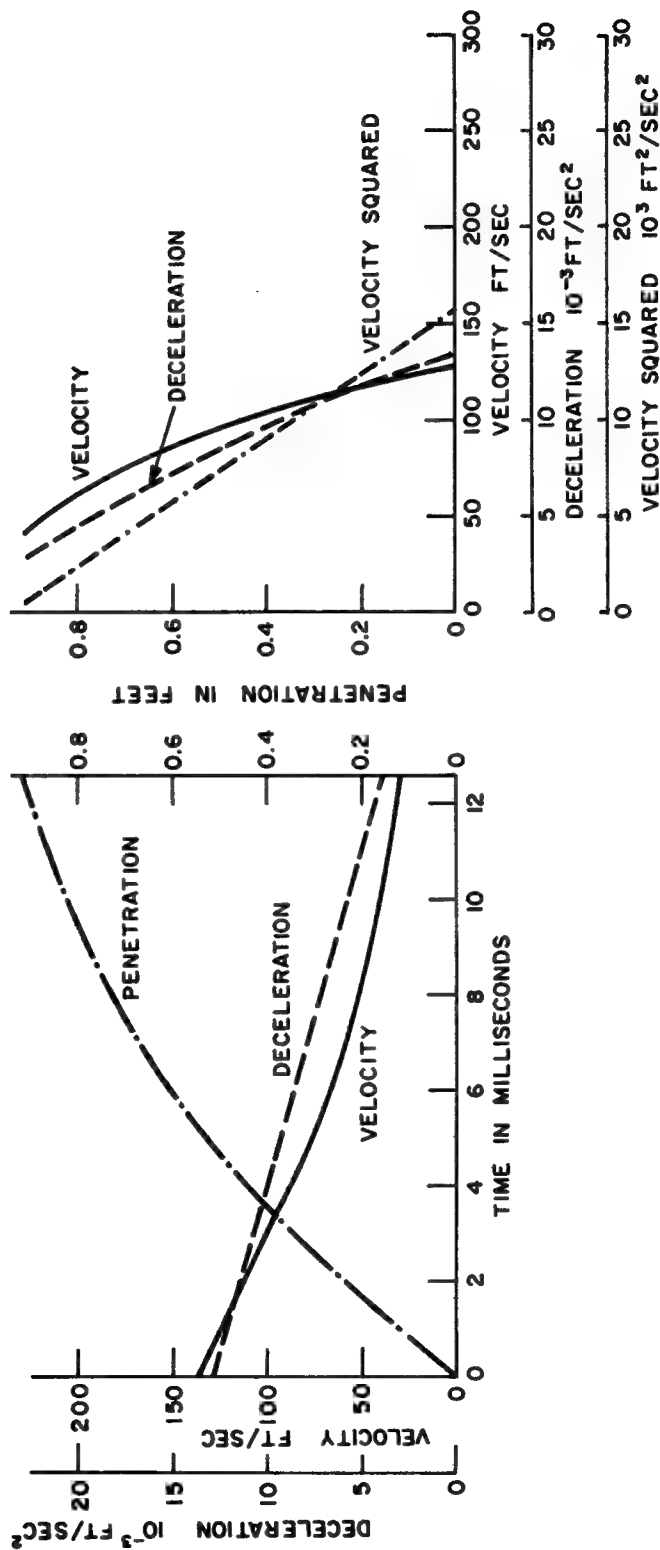


Figure 51. Motion-Time and Motion-Penetration Relations for Test No. (SO)G-IV-3D

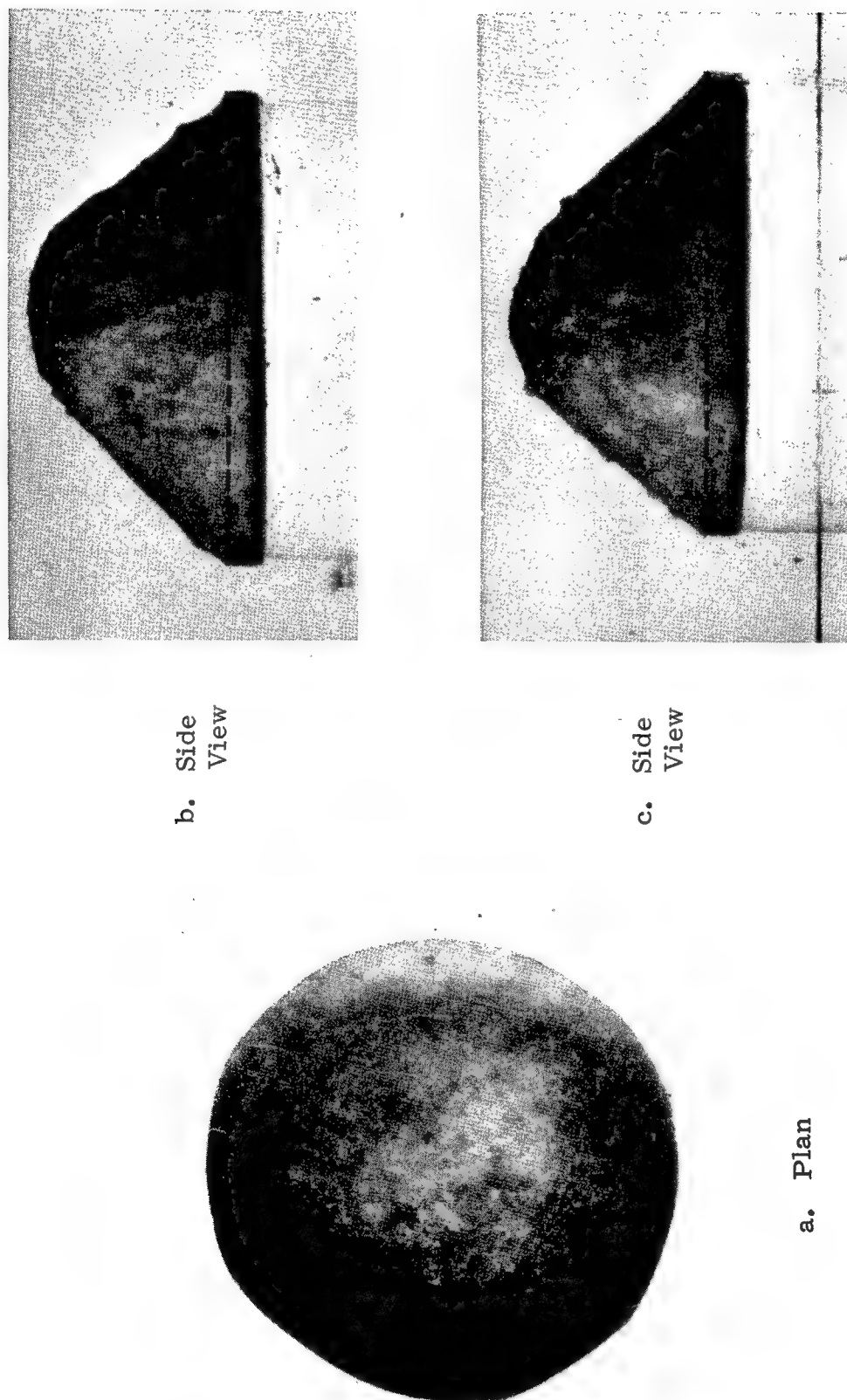
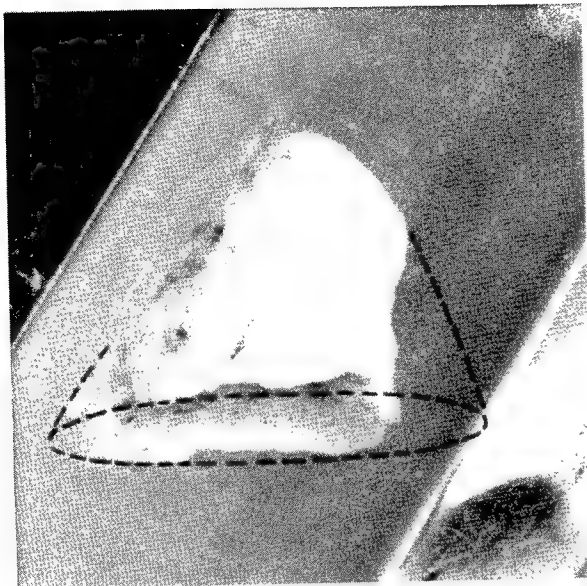
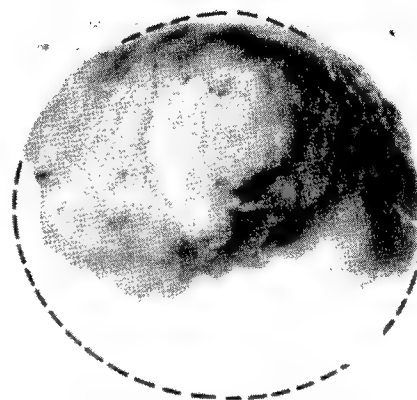


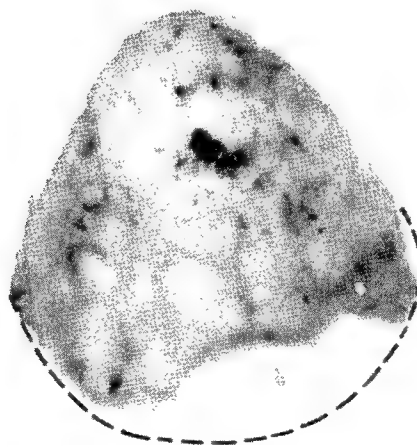
Figure 53. Plan and Side Views of Soil Nose Formed on 1-1/2 inch Blunt Nosed Projectile Fired Into Ottawa Sand



a



b



c

Figure 54. Three Different Views of Soil Nose that Formed on Hemispherical Nose of 1-1/2 inch Projectile. Ottawa Sand Target



Figure 55. 1-1/2 inch Projectile and Soil Nose Remains
After Penetration Into Ottawa Sand

diameter and about 4 inches long was developed which included a piezoresistive accelerometer. The decelerations were transmitted during penetration and recorded on magnetic tape. The instrumentation seemed to be excellent and should in the future provide valuable data. The entrance velocities were recorded using high speed cameras. The procedure was to propel the projectile down a tube using J. A. T. O. rocket power. The propelling equipment was stopped about 6 feet short of impact to allow the projectile to fly free into the target. The target was a mixture of various particles and plastic enclosed in a "sono" tube. The diameter of the tube was 24 inches and the length about 24 inches. Two sets of data are shown in Figures 56 and 57. It has been noticed that the deceleration records are highly influenced by the angle of attack. If the projectile was not exactly perpendicular to the target, the entrance spikes were lower and the depth of penetration greater for the blunt nosed projectiles. The sharp nosed projectiles were hot when taken from the target but the blunt nosed projectiles were cool. Soil noses were formed on the blunt projectiles. In Figures 58 and 59 are photographs of 1-1/2-inch blunt nosed projectiles flying out of the rear of the targets with their soil noses still attached. The density of the target material was 56 pounds per cubic foot and the unconfined compressive strength was 3 pounds per square inch.

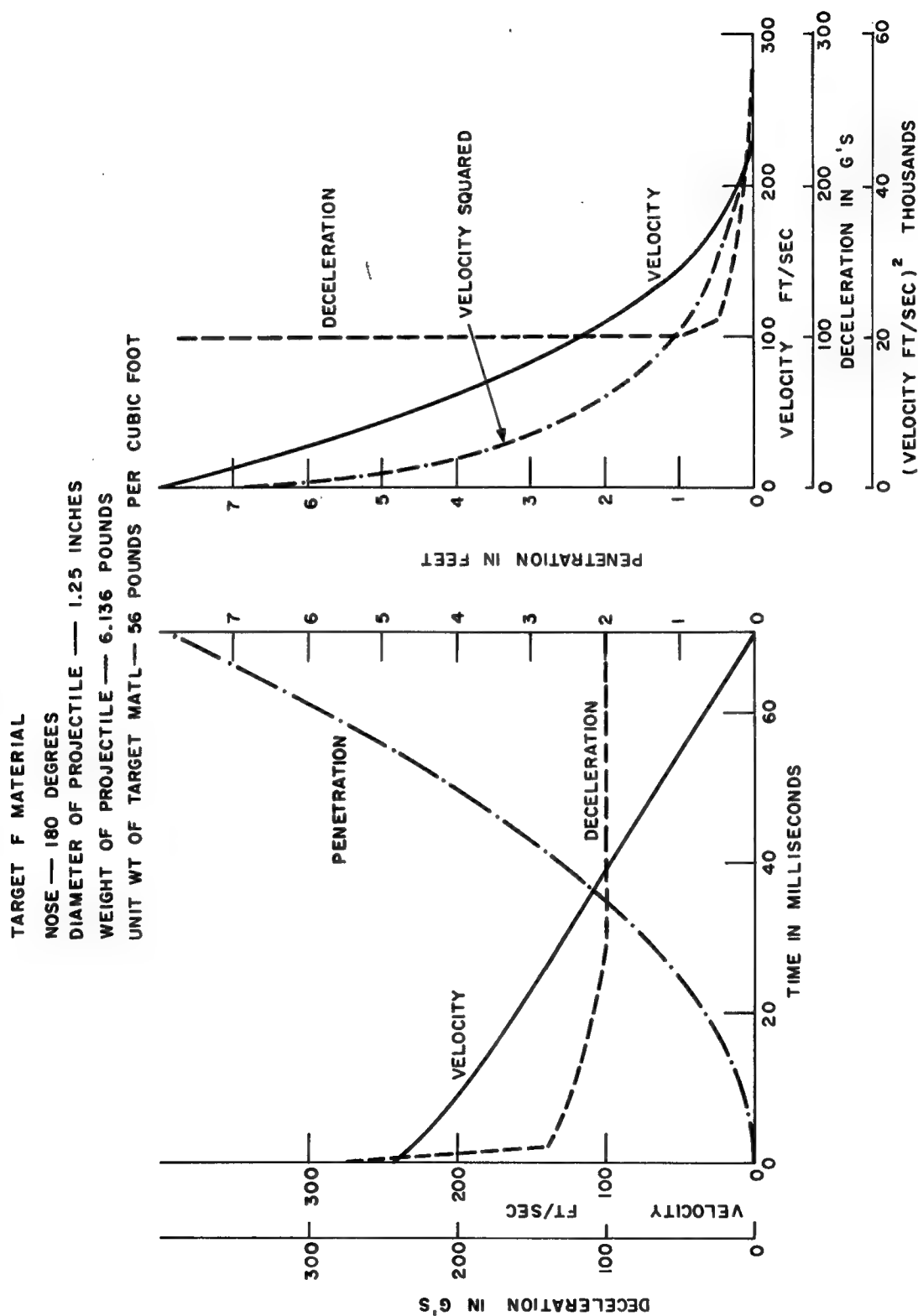


Figure 56. Motion-Time and Motion-Penetration Relations for Horizontal Test No. 277-109

TARGET F MATERIAL
 NOSE — 20 DEGREES
 DIAMETER OF PROJECTILE — 1.25 INCHES
 WEIGHT OF PROJECTILE — 6.136 POUNDS
 UNIT WT OF TARGET MATL — 56 POUNDS PER CUBIC FOOT
 MAX DEPTH OF PENETRATION — 11 FEET

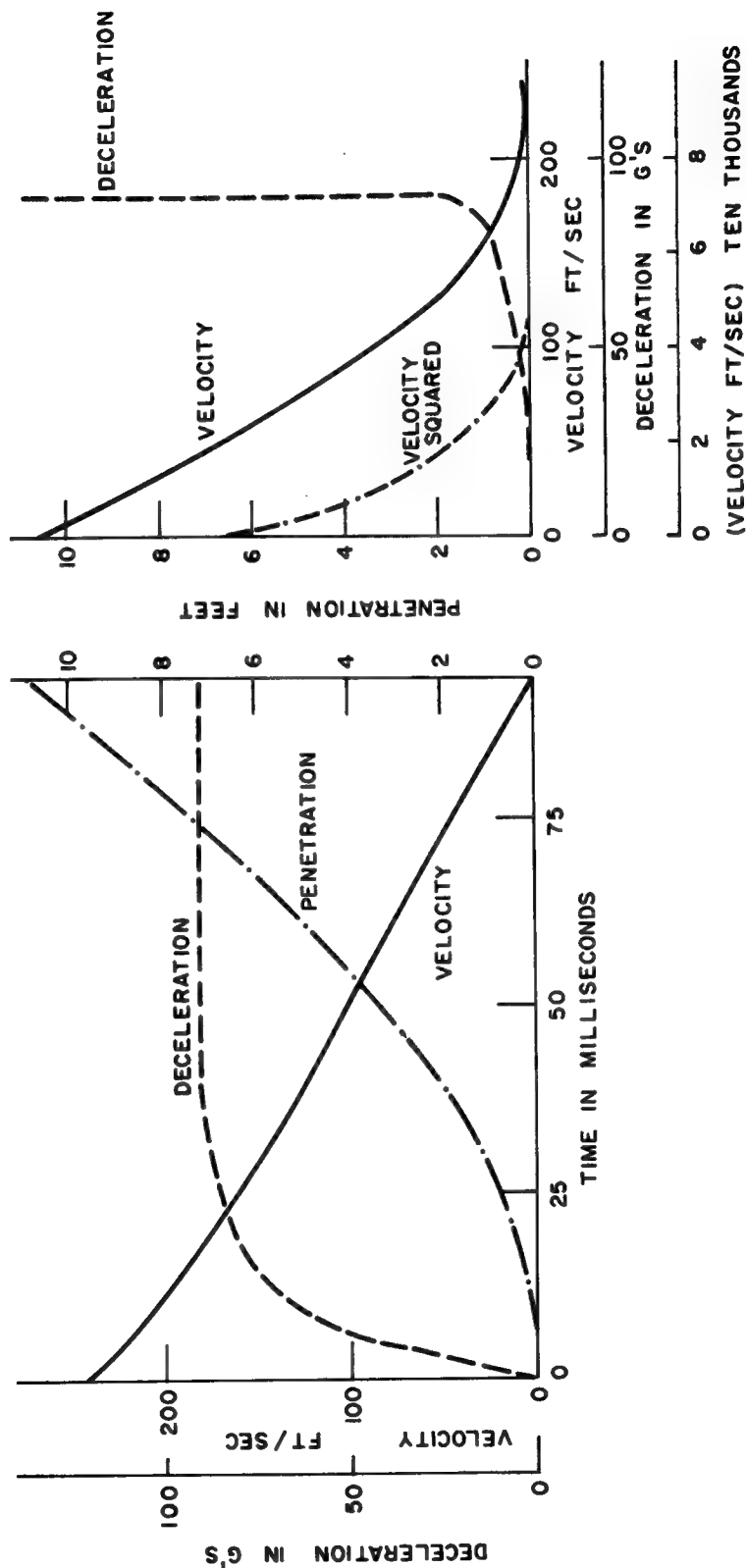


Figure 57. Motion-Time and Motion-Penetration Relations for Horizontal Test No. 277-110

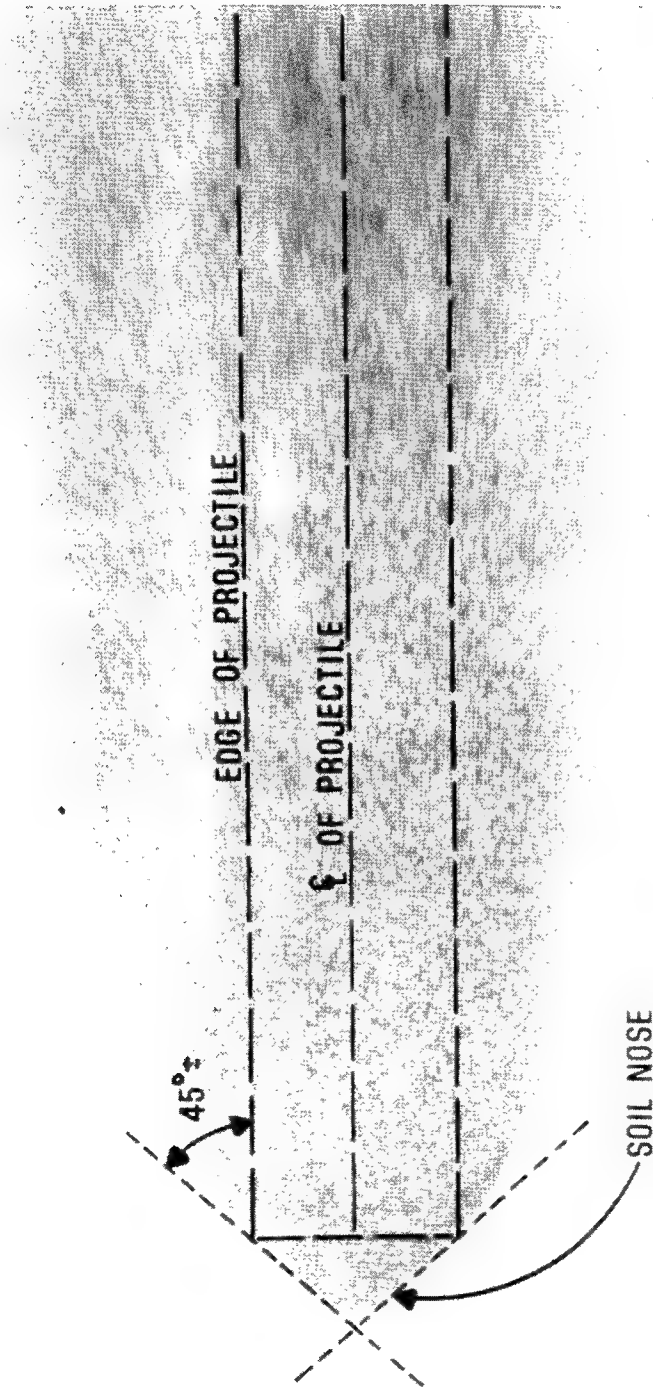


Figure 58. Blunt Nosed Projectile Flying Out Rear of Horizontal Target

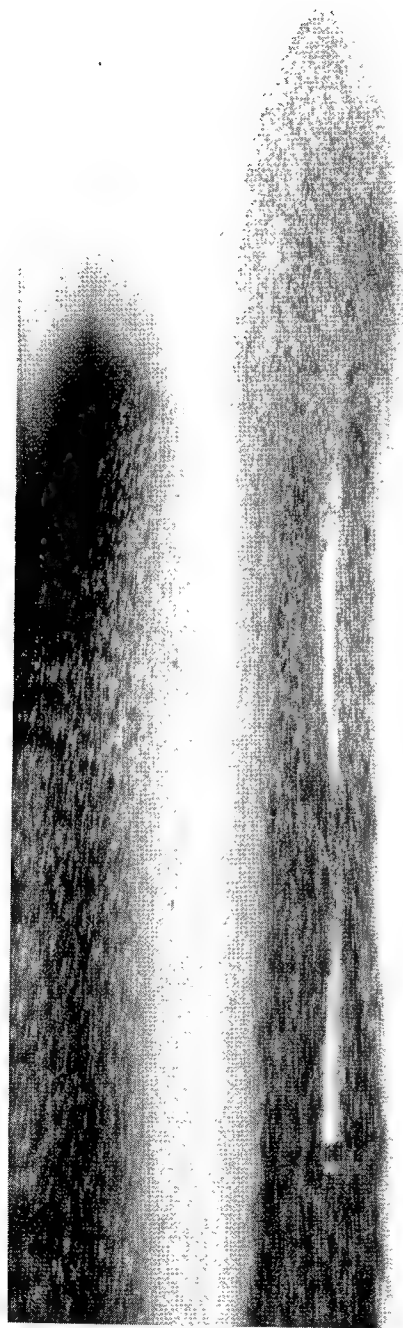


Figure 59. Image Motion Photograph of Blunt Nosed Projectile
Exiting from Pseudo Soil Target

The data obtained so far generally show that in these materials the deceleration is almost constant as the projectile passes through the constrained target. There is not much difference in these decelerations for either the blunt or sharp nosed projectiles. However, the sharp nosed projectiles do not show the high entrance spike the blunt nosed projectiles exhibit. The targets after penetration have radial cracks, a small crater at the entrance point and a much larger crater at the point of exit.

Full Scale Tests

a. Blunt Nosed Tests Into Dry Lake Playa -- A series of three blunt nosed vertical tests has been performed as a part of this study. The projectiles were dropped from a helicopter into a dry lake playa at the Sandia Test Range, Tonopah, Nevada. In Table I, the pertinent projectile parameters and depths of penetration are given. In Test No. 120-57 the accelerometers and radio transmission package inside the projectile were shattered upon impact so no deceleration time signature was obtained. In the two other blunt nosed tests, a record was obtained using a shock mitigated package, but the initial deceleration spike was not obtained. The average deceleration after the spike was approximately 2000 g's. In each of the three tests, the heave of the surface was only about 1/4 inch except near the edge of the impact crater, but the volume of heave plus the volume of the crater

TABLE I

Full Scale Vertical Tests

<u>Test No.</u>	<u>Diameter (in.)</u>	<u>Weight (lb.)</u>	<u>Length (in.)</u>	<u>Nose Type</u>	<u>Impact Velocity (ft/sec)</u>	<u>Depth of Penetration (ft.)</u>	<u>Soil Type</u>
120-57	9	1154	162	Blunt	540	13.5	Main Lake See Figure 60
120-89	9	636	110-3/8	Blunt	600	13.1	Antelope Lake See Figure 61
120-97	9	1050	113	Blunt	650	15.3	Antelope Lake See Figure 61

above the initial surface was a little greater than the volume of the hole created by the projectile.

The surface elevations after penetration are given in Table II for Test No. 120-57. The surface deformations for Test Nos. 120-89 and 120-97 were similar. Table III shows the calculations of the volume changes for Test No. 120-57. The crater was larger in Test Nos. 120-89 and 120-97 than in Test No. 120-57. The soil strata descriptions are shown for Test No. 120-57 in Figure 60 and for the other two tests in Figure 61.

The ground surface around the point of impact was cracked radially out about 12 feet in Test No. 120-57 and somewhat less in the other two tests. In Figures 62 and 63 are shown the surfaces after impact before and after the cracks were marked (Test No. 120-57).

A soil nose formed in all three tests. In Figures 64a, b, and c are shown the soil nose taken from the projectile in Test No. 120-57. In Figures 65a and 65b are shown the projectile before removal and the soil nose being excavated after the projectile was removed. In Figures 66a and 66b are shown photographs of the projectiles used in Test Nos. 120-87 and 120-97 after removal from the soil. The paint was slightly removed on the side of the projectile that was on the bottom side of the trajectory but this removal area does not extend

TABLE II

Surface Elevations Along Perpendicular Section
After Projectile Penetration
Test No. 120-57

[illegible]

TABLE III
Calculations for Volumes of Movement
Test No. 120-57

Seg No.	w	$\frac{w}{2}$	$\frac{w}{3}$	h_1	h_2	h_1+h_2	h_1+2h_2	$\frac{h_1+2h_2}{h_1+h_2}$	$A = \frac{w}{2}(h_1+h_2)$	$x = \frac{w}{3}\left(\frac{h_1+2h_2}{h_1+h_2}\right)$	y	$R = x+y$	$Vol = \frac{\pi}{2}RA$
North													
1	0.137	0.07	0.05	0	0.08	0.08	0.16	2.0	0.005	0.091	1.06	1.154	0.01
2	1.0	0.5	0.33	0.08	0.03	0.11	0.14	1.27	0.055	0.424	1.2	1.624	0.14
3	1.4	0.7	0.47	0.03	0.02	0.05	0.07	1.40	0.035	0.658	2.2	2.858	0.16
4	1.6	0.8	0.53	0.02	0.01	0.03	0.04	1.33	0.024	0.705	3.6	4.305	0.16
5	4.8	2.4	1.6	0.01	0.01	0.02	0.03	1.50	0.048	2.400	5.2	7.600	0.573
6	2.65	1.32	0.88	0.01	0	0.01	0.01	1.0	0.013	0.883	10.0	10.883	0.226
Total Volume of Heave in North Quadrant (cu ft)													1.268
Crater	0.69	0.34	0.23	0.42	0	0.42	0.42	1.0	0.143	0.23	0.375	0.605	0.136
South													
1	0.47	0.24	0.16	0.02	0.08	0.10	0.18	1.83	0.023	0.288	0.86	1.151	0.041
2	1.00	0.50	0.33	0.08	0.04	0.12	0.16	1.33	0.060	0.444	1.33	1.774	0.167
3	1.09	0.55	0.36	0.04	0.03	0.07	0.10	1.43	0.038	0.518	2.33	2.848	0.171
4	3.13	1.56	1.04	0.03	0.03	0.06	0.09	1.50	0.094	1.564	3.42	4.985	0.735
5	2.98	1.49	0.99	0.03	0.02	0.05	0.07	1.40	0.075	1.390	6.55	7.940	0.929
6	2.57	1.28	0.86	0.02	0	0.02	0.02	1.00	0.026	0.857	9.53	10.387	0.419
7	11.24	5.62	3.75	0.02	0	0.02	0.02	1.00	0.090	3.747	0.86	4.610	-0.651
Total Volume of Heave in South Quadrant (cu ft)													1.811
Crater	0.49	0.24	0.16	0.59	0	0.59	0.59	1.0	0.143	0.163	0.375	0.538	0.121
East													
1	0.13	0.07	0.04	0	0.13	0.13	0.26	2.0	0.009	0.088	1.03	1.117	0.016
2	1.04	0.52	0.35	0.13	0.04	0.17	0.21	1.24	0.088	0.429	1.16	1.589	0.220
3	1.45	0.78	0.48	0.04	0.01	0.05	0.06	1.20	0.039	0.580	2.20	2.780	0.170
4	4.71	2.36	1.57	0.01	0.01	0.02	0.03	1.50	0.047	2.355	3.65	6.005	0.443
5	2.59	1.29	0.86	0.01	0.02	0.03	0.05	1.67	0.039	1.441	8.36	9.801	0.600
6	2.75	1.37	0.92	0.02	0	0.02	0.02	1.00	0.028	0.917	10.95	11.867	0.522
Total													1.971
Crater	0.65	0.33	0.22	0.65	0	0.65	0.65	1.0	0.215	0.22	0.375	0.595	0.201
West													
1	1.20	0.60	0.40	0.02	0.01	0.03	0.04	1.33	0.018	0.532	1.27	1.802	0.051
2	2.26	1.13	0.75	0.01	0.01	0.02	0.03	1.50	0.023	1.130	2.47	3.600	0.130
3	1.97	0.99	0.66	0.01	0	0.01	0.01	1.00	0.099	0.657	4.73	5.3870	0.838
Total													1.019
Crater	0.87	0.44	0.29	0.70	0	0.070	0.070	1.0	0.308	0.29	0.375	0.665	0.322
Total surface heave													6.069
Total volume of crater below original surface													0.780
Volume of hole made by projectile = $\pi (0.375)^2 (13.5)$													5.964
Volume of crater above original surface = $(0.07)(\pi)(1.24)^2$													0.338

WOODWARD CLYDE SHERARD AND ASSOCIATES Consulting Soil Engineers and Geologists 1240 West Bayview Avenue Denver 23, Colorado		Job No. 7336-6762 Job Name TONOPAH TEST SITE	
DRILLING LOG		LOCATION (Coordinates or Station) N 2000 - S 100	
ST-2 (SOIL TEST HOLE 2)		NAME OF DRILLER BENE CAMPBELL	
4" x 4" ROTARY/AIR		THICKNESS OF OVERBURDEN HUNGEN 50"	9" TOTAL DEPTH OF HOLE 50"
13		LONGYEAR 44	
15		NONE 10-3-63 10-3-63	
5331 ±		SIGNATURE OF DRILLER BENE CAMPBELL	
		CLAY - SILTY, LIGHT BROWN, DRY, LOW PLASTIC, LIGHTLY FRACTURED. CL-CH CLAY - VERY SILTY, DRY TO SLIGHTLY MOIST LOW TO HIGHLY PLASTIC, BLOCKY, STIFF, STREAKS OF CH CL-MH SAND - VERY SILTY, VERY CALCAREOUS, LIGHT GRAY (WHITE), NON TO LOW PLASTIC FINES, DRY, VERY FRIABLE. SM-MH SAND - SILTY, MOIST, MED. BROWN, FINE TO COARSE GRAINED, NON PLASTIC, DENSE TO VERY DENSE. PROBABLE THIN CEMENTED LAYERS, VERY EASY TO DRILL. SP-SH SAND - VERY SILTY, DRY, LIGHT BROWN TO WHITE, VERY CALCAREOUS, DENSE TO VERY DENSE, WEAKLY TO WELL CEMENTED, SOME SMALL (PEA) GRAVEL, MAX. SIZE 1/4", (MOIST STREAKS OF SM NON-PLASTIC, NON-CEMENTED SAND VERY DENSE). SM-SH	
		50	1 34/12" (34)
		NO	SAMP. 50/7" (JAR SAMPLE 9' - 15' (85) OF CUTTINGS)
		70	1 50/9" (61)
		80	1&2 43/12" (43)
		95	1&2 21/12" (21)
		80	1&2 42/12" (42)
		90	1 50/7" (JAR OF CUTTINGS) (85)
		NO	SAMP. 50/6" (CUTTINGS FROM BARREL) (100)
		60	1&2 50/12" (50)
		70	1&2 47/12" (47)

Figure 60. Description of Soil Strata
for Test 120-57

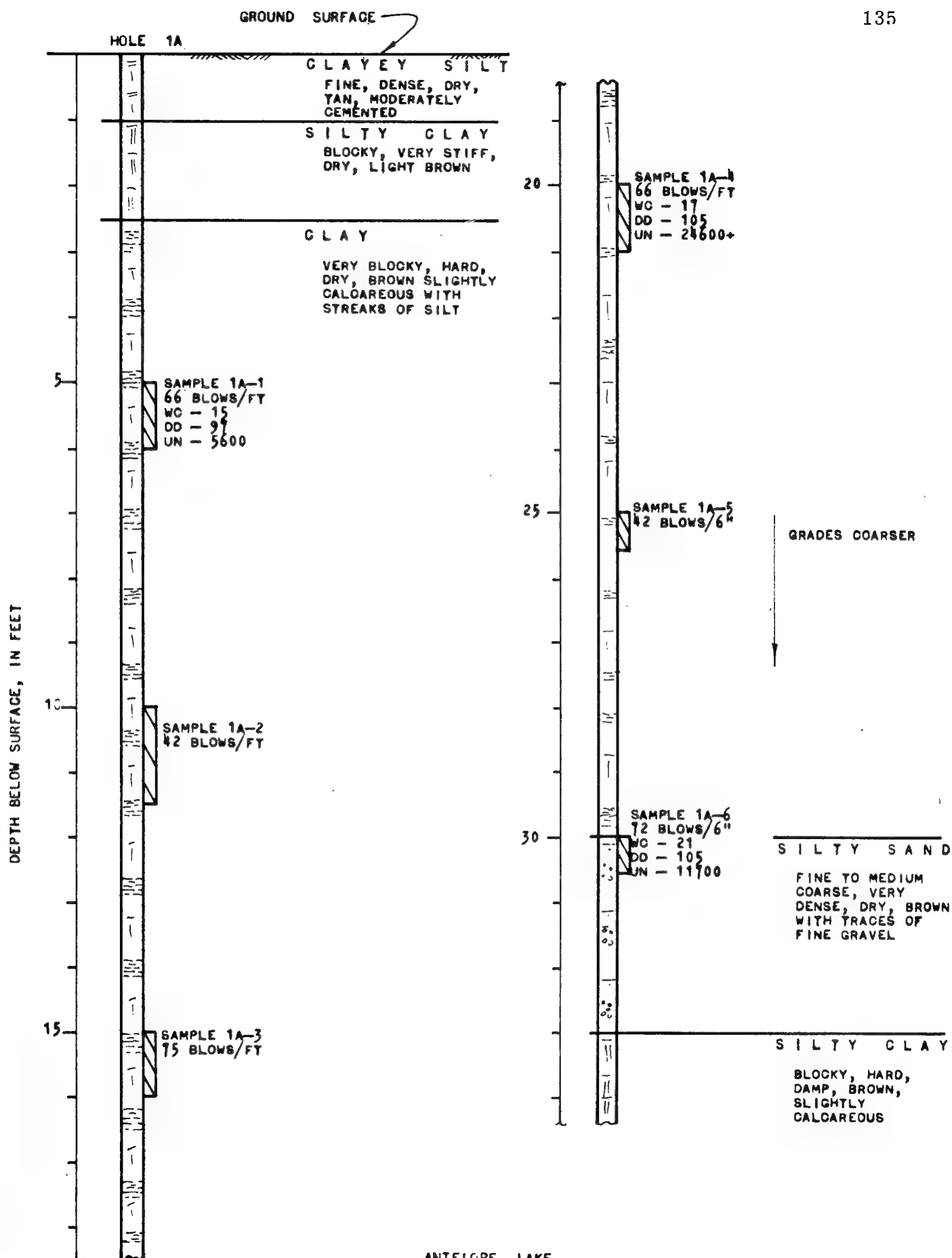


Figure 61. Log of Borings for Tests 120-89
and 120-97

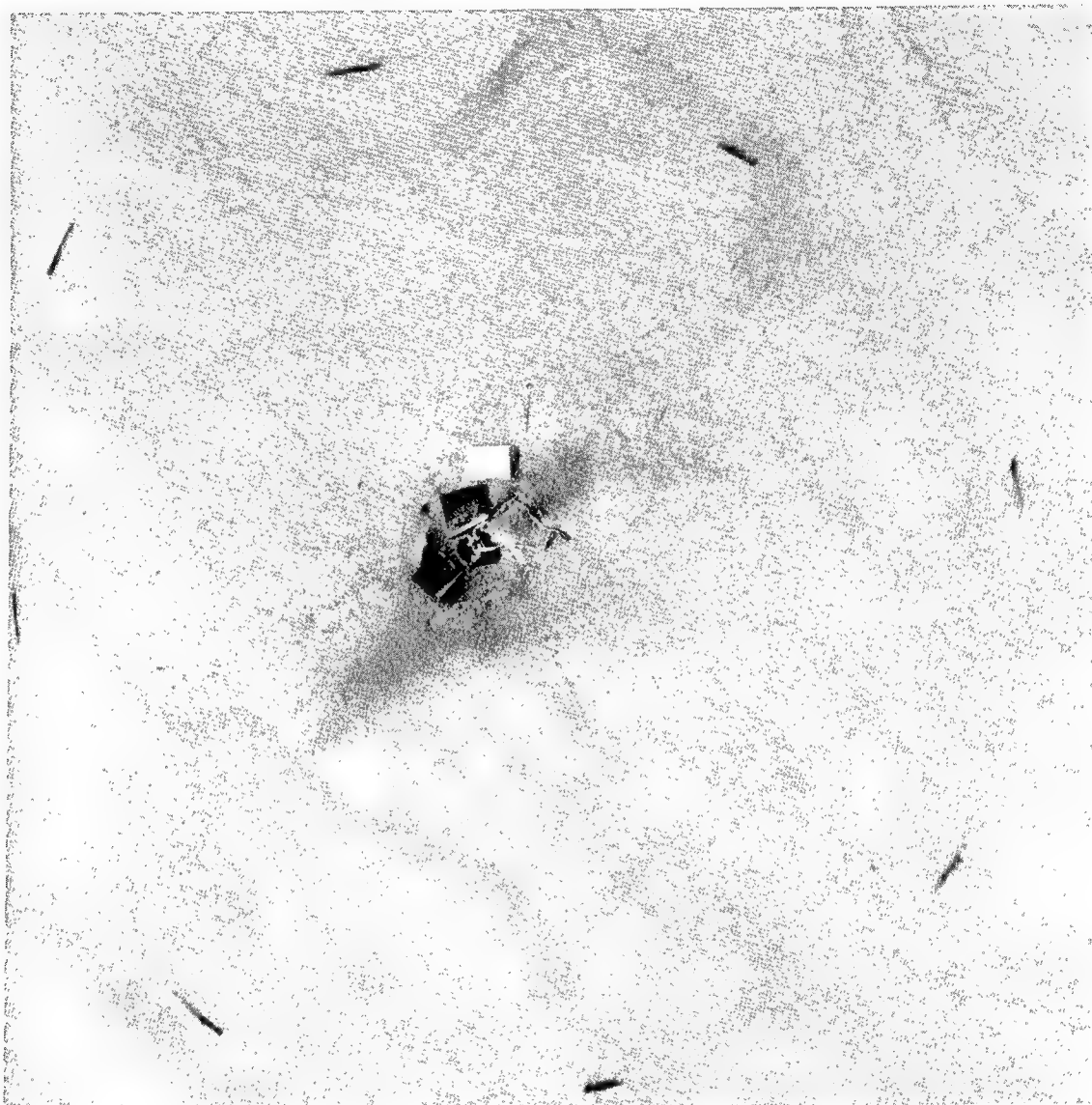


Figure 62. Photograph of Surface of Playa Lake Bed After Penetration of 9-inch Blunt Nosed Projectile

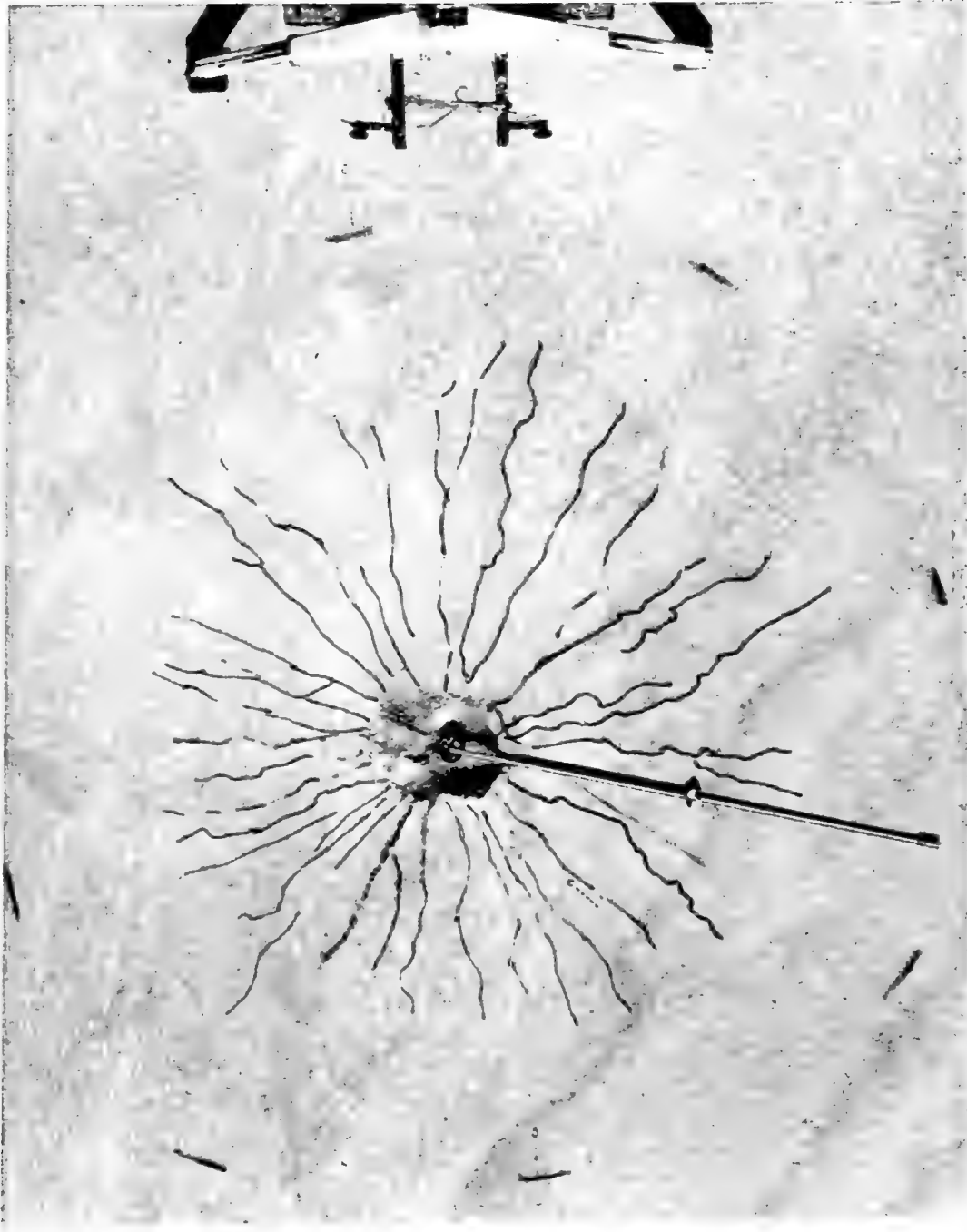


Figure 63. Photograph of Playa Surface with Radial Cracks Marked - After Penetration of 9-inch Blunt Nosed Projectile



Figure 64a. Side View of Soil Nose Taken from 9-inch Blunt Nosed Projectile
After 13.5 feet of Penetration Into Playa



Figure 64b. Side View of Soil Nose Taken from 9-inch Blunt Nosed Projectile After 13.5 feet of Penetration Into Dry Lake Playa



Figure 64c. Plan View of Soil Nose Taken from 9-inch Blunt Nosed Projectile After Penetration Into Playa

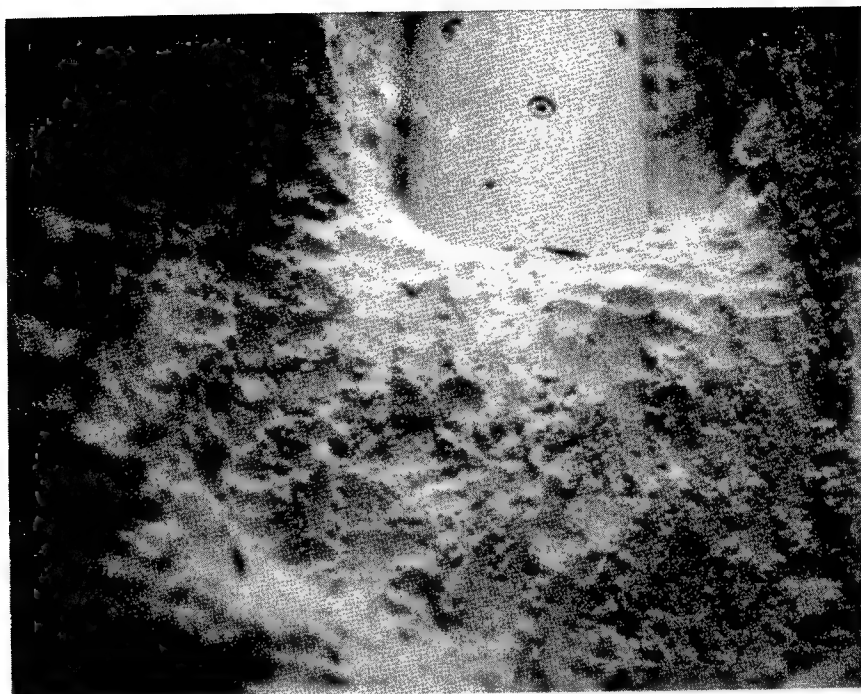
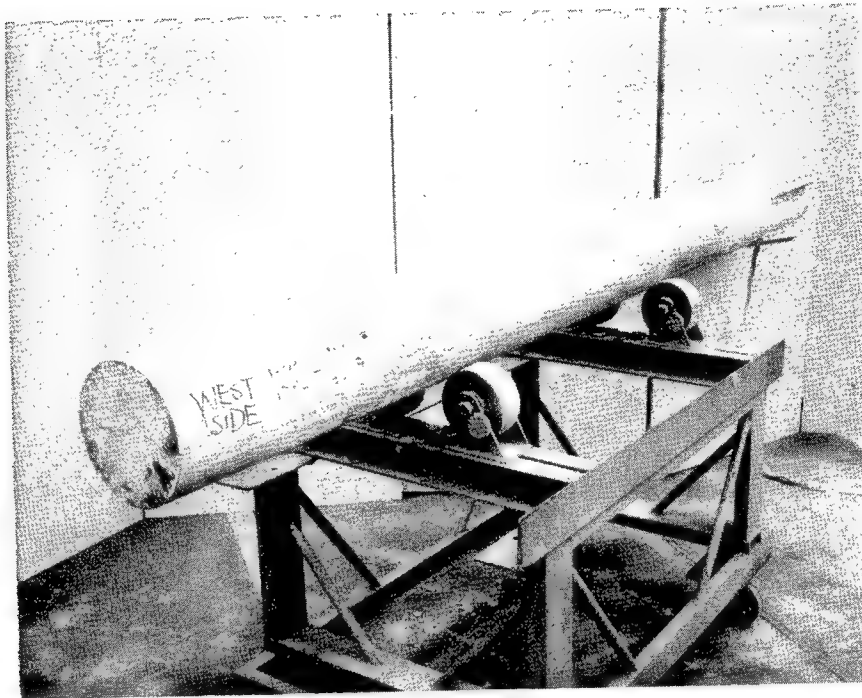


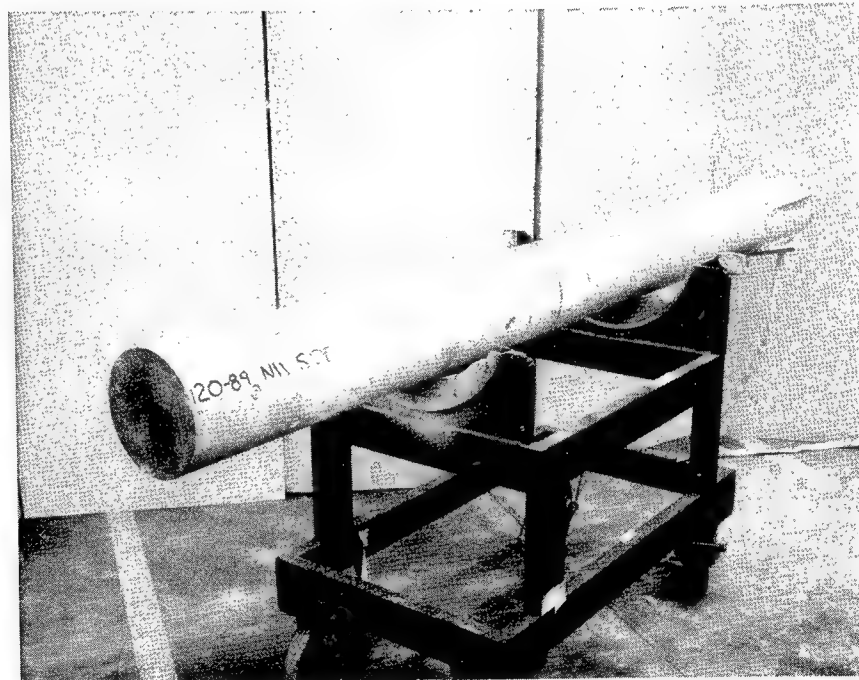
Figure 65a. Photograph of 9-inch Blunt Nosed Projectile Before Removal from Playa



Figure 65b. Soil Nose Being Recovered from Playa After Projectile was Removed



a



b

Figure 66. Photographs of Blunt Nosed Projectiles After Penetration Into Dry Lake Playa

to the blunt end. In Test No. 120-57 the paint was only removed for 6 inches back from the blunt end on the area that was on the bottom side of the trajectory. All three tests were about 5 degrees off the vertical at time of impact. When the projectiles were removed, soil was stuck to the sides, but the paint was intact under the soil. The hole remained open in all three tests and none of the projectiles could have been removed had not a hole 4 feet in diameter been bored down beside the projectile. This large hole allowed the projectile and the soil nose to be excavated. The penetration hole had to be larger during penetration process or all of the paint on the projectile would have been removed. The ultimate angle of internal friction and the cohesive strength of the soil near Test Nos. 120-89 and 120-97 was about 41 degrees and 1 ton per square foot.

b. Sharp Nosed Tests Into Playa -- The soil for these tests was similar to the soil described for Test No. 120-57. These tests were conducted by Sandia Corporation using the same type equipment described for the blunt nosed tests. Soil noses were not looked for nor was the surface surveyed after impact. For one 2.2 caliber test, none of the paint was removed immediately behind the nose. In other sharp nosed projectile tests, where the nose shape was varied, it is believed that the area of paint removal immediately behind the nose increased as the nose was made longer. The motion time data for

three tests are given in Figures 67, 68, and 69. The depth of penetration listed on the figures is a measured depth where the penetration plotted is a calculated value obtained by numerically integrating the deceleration twice with respect to time. The deceleration is certainly not a linear function of the velocity squared at any instant of time as the Poncelet equation assumes. Soil has been observed stuck to the point in several of the tests. The data presented do not show a deceleration spike upon impact.

By making the projectile nose sharp, the surface deceleration spike must be highly mitigated, but for high velocity impact (1000-1500 ft/sec), the afterbody of the projectile was broken in tension when no deceleration spike was recorded. A very short duration deceleration spike must have existed in order to propagate a compression wave up the projectile so that a tension wave would be reflected off the rear of the projectile to break the afterbody. Generally, the sharp pointed projectiles penetrated further into the dry lake playa than blunt nosed projectiles when all other parameters were held constant.

c. Sharp Nosed Test Into Sand -- Although many sharp nosed tests have been performed by Sandia Corporation into many different soils, one test into sand is of particular interest. The test was performed at Eglin Air Force Base using a projectile with a 9.25 caliber point. The data obtained for deceleration, velocity and penetration

TARGET — DRY LAKE PLAYA
 NOSE — 2.2 CALIBER OGIVE
 WEIGHT — 990 POUNDS
 MAX DEPTH OF PENETRATION — 9.2 FEET
 DIAMETER OF PROJECTILE — 9 INCHES

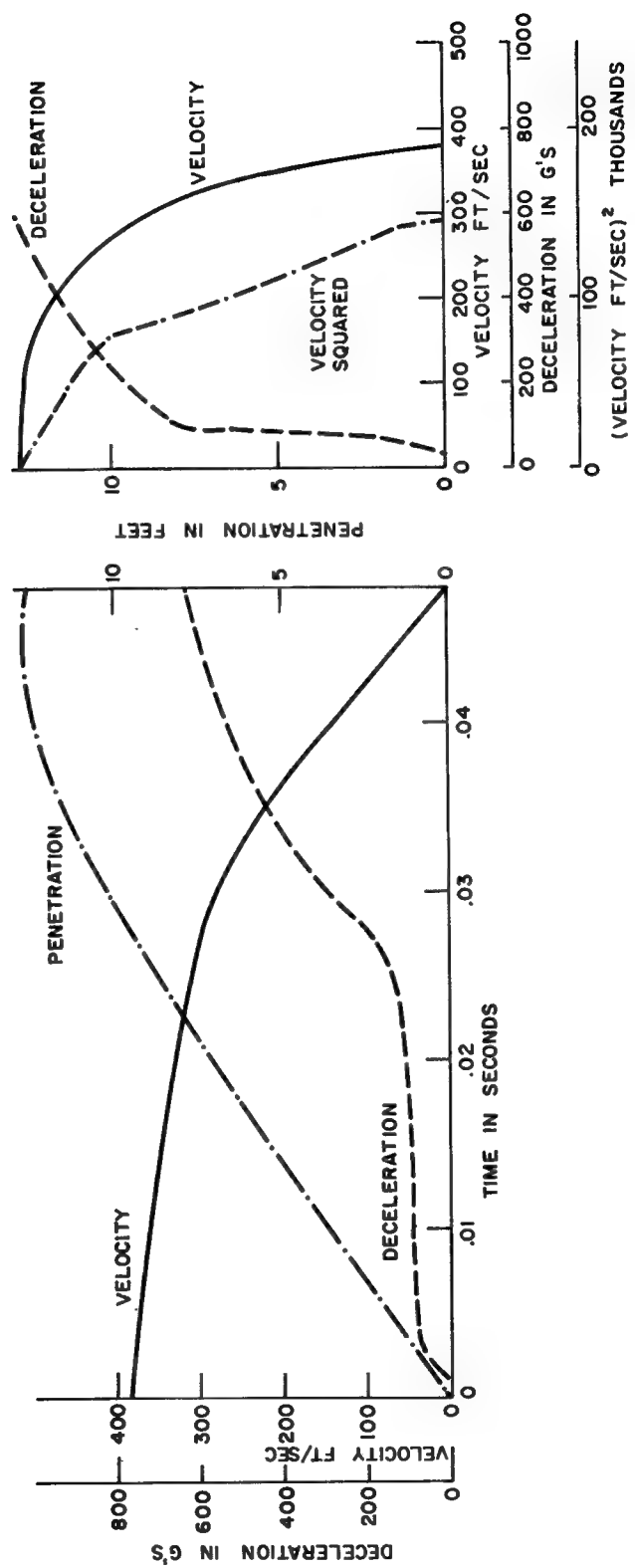


Figure 67. Motion-Time and Motion-Penetration Relations for Test No. 120-7

TARGET — DRY LAKE PLAYA

NOSE — 6 CALIBER OGIVE

WEIGHT — 900 POUNDS

MAX DEPTH OF PENETRATION — 14.2 FEET

DIAMETER OF PROJECTILE — 9 INCHES

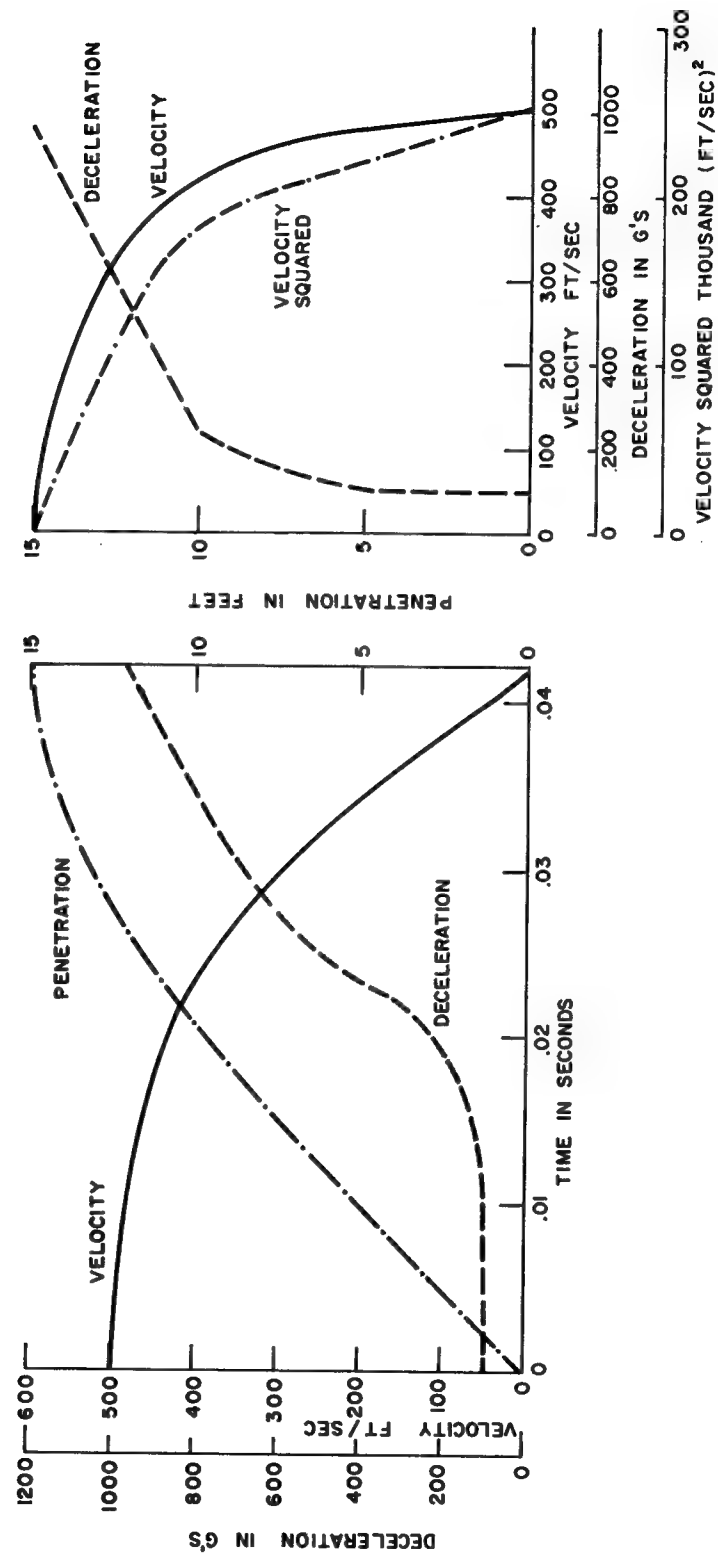


Figure 68. Motion-Time and Motion-Penetration Relations for Test No. 120-9

TARGET — DRY LAKE PLAYA
 NOSE — 9.25 CALIBER OGIVE
 WEIGHT — 1105 POUNDS

MAX DEPTH OF PENETRATION — 14.2 FEET
 DIAMETER OF PROJECTILE — 9 INCHES

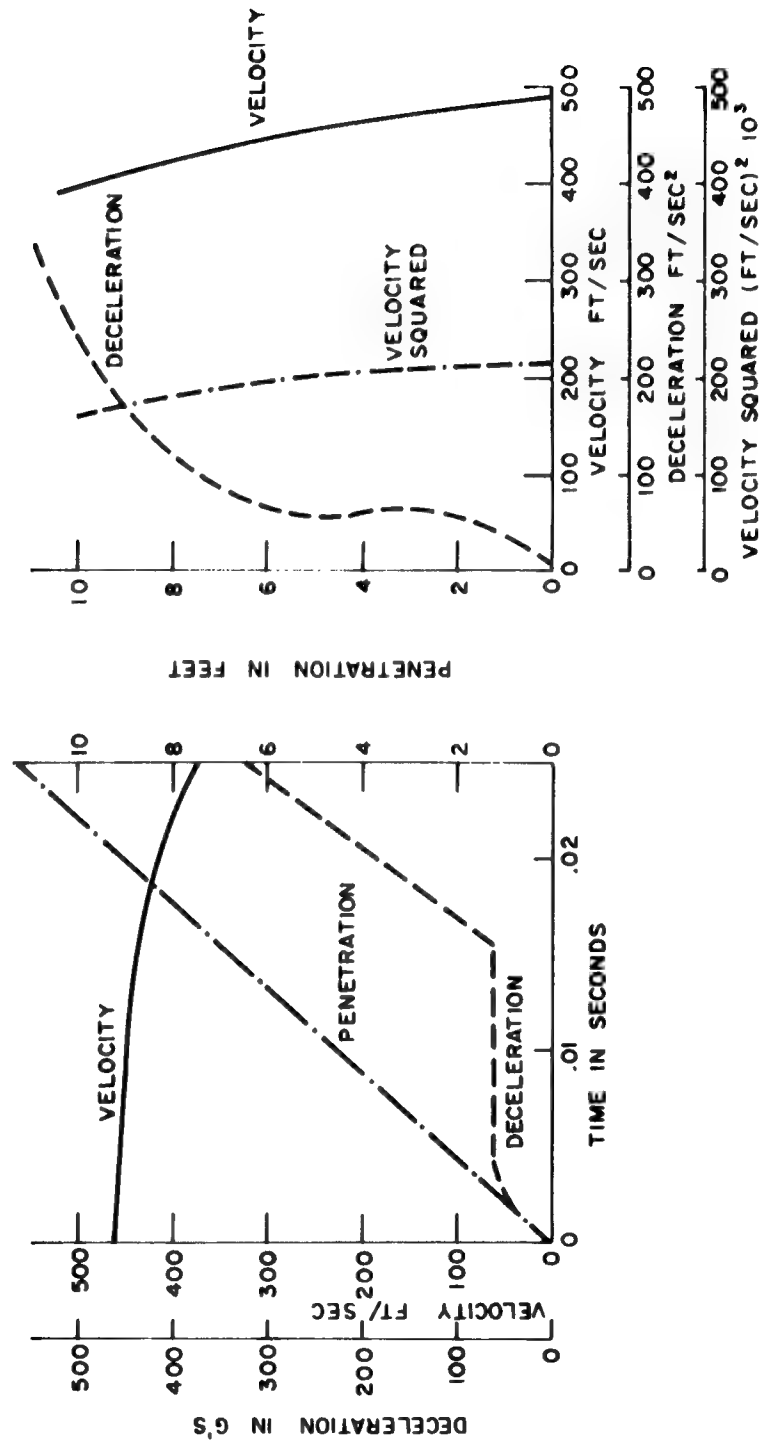


Figure 69. Motion-Time and Motion-Penetration Relations for Test No. 120-11

are shown in Figure 70. Photographs of the projectile before and after penetration are shown in Figures 71 and 72. The crater and hole formed by the projectile are shown in Figure 73. In this test, a soil nose certainly did not form since the point is ablated. Possibly the ablation would not have happened if the point had not been so sharp. Knowing that soil noses do form on projectiles with short noses, and that long nosed projectiles ablate, it seems reasonable to assume there is some nose shape where neither phenomena occurs. The line of separation between the soil and afterbody was about 4 feet back of the point on this 9 inch projectile.

No deceleration record was obtained after one tenth of a second of time which corresponds to 56 feet of penetration although the projectile continued in penetration to a depth of 71 feet.

TARGET — EGLIN SAND
 NOSE — 9.25 CALIBER OGIVE
 WEIGHT — 1150 POUNDS
 MAX DEPTH OF PENETRATION — 71 FEET
 DIAMETER OF PROJECTILE — 9 INCHES

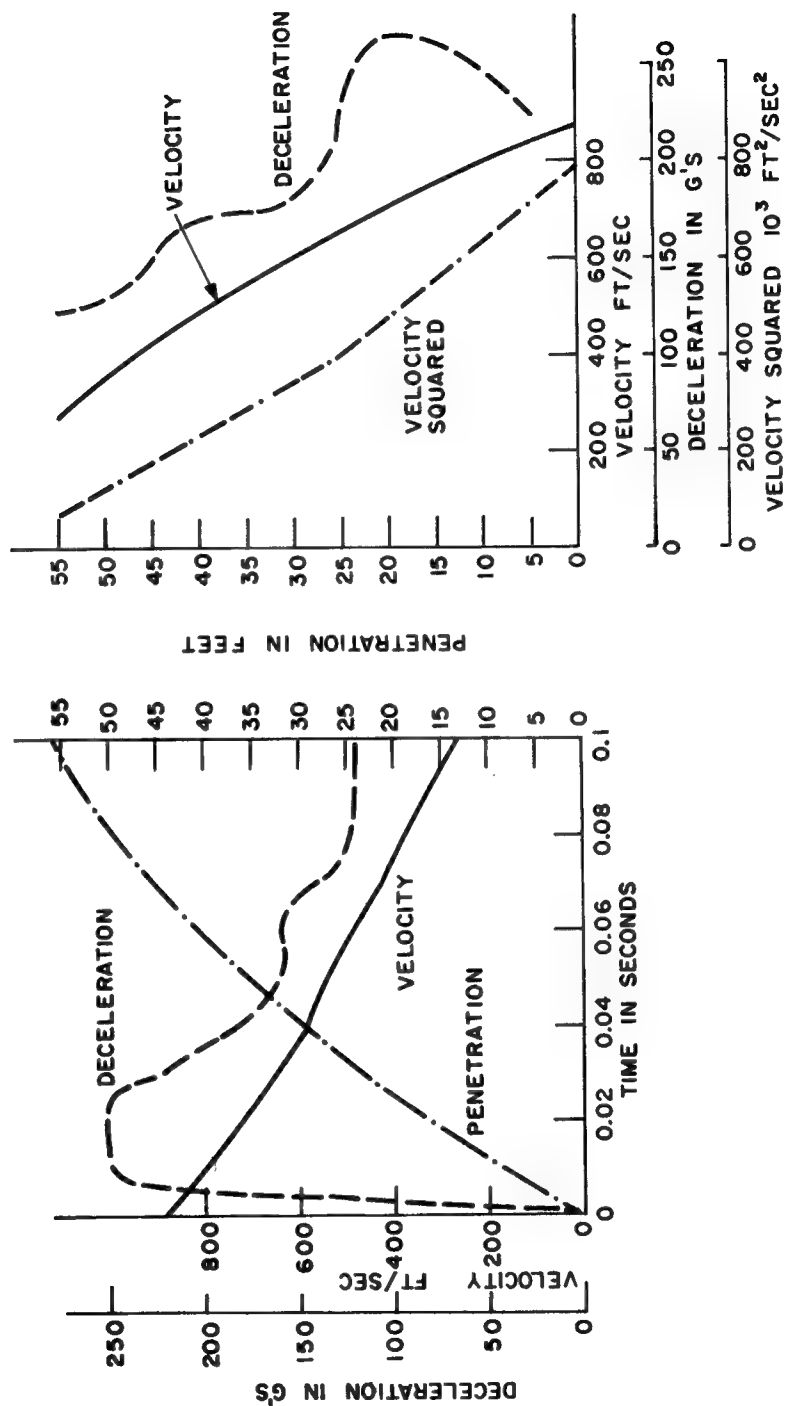


Figure 70. Motion-Time and Motion-Penetration Relations for Test No. 120-5

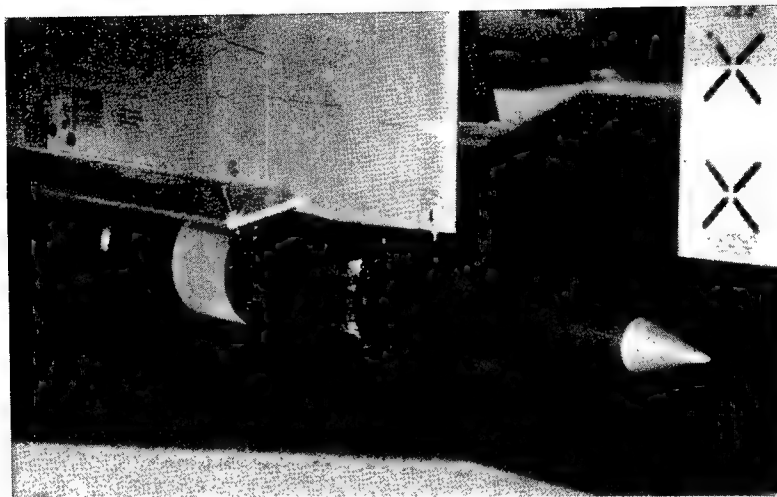


Figure 71. Photograph of 9.25 Caliber Projectile
Before Penetration Into Sand

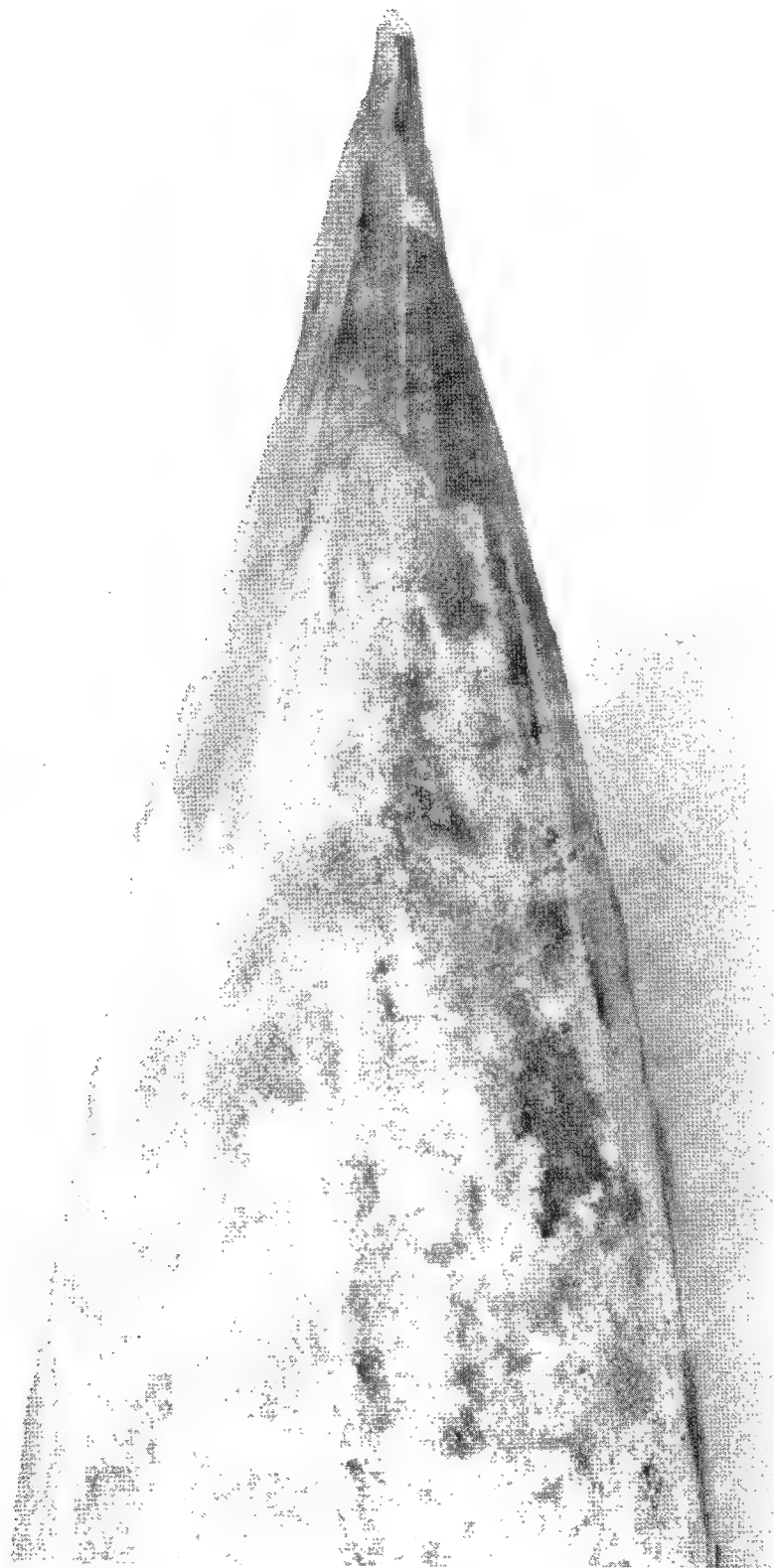


Figure 72. 9.25 Caliber Projectile After Sand Penetration



Figure 73. Crater in Eglin Sand After Penetration of 9-inch Diameter Projectile

IV. SUMMARY AND RESULTS OF EXPERIMENTAL OBSERVATIONS

1. As shown by all the deceleration records, the soil force which resists projectile motion is not constant and independent of velocity as Euler predicted nor is it a linear function of the velocity squared term as the Poncelet and Petry formulas assume.

2. Before the projectile hits, the state of stress in the half-space of soil is as follows:

$$\sigma_z = z\gamma$$

$$\sigma_r = kz\gamma \quad (\text{III-1a})$$

$$\tau_{rz} = 0$$

where

γ = effective unit weight of soil

and

k = coefficient of earth pressure at rest.

$$k \leq 1$$

The velocities are all zero before impact, thus

$$V = V_r = V_z = 0 \quad (\text{III-1b})$$

The initial state of stress for any other target is different.³⁸

During the event when $r \rightarrow \infty$, or when $z \rightarrow \infty$ the equation for the stresses and velocities before impact must hold. This would not be true for another kind of target.

3. A soil nose forms on blunt, hemispherical and short ogive nosed projectiles as the projectile enters the soil. This nose is nearly conical. On long ogive nosed projectiles, the metal ablates. The shape of nose and angle of incidence highly affects the deceleration spike at time of impact. The energy expended as the projectile passes from air into the soil seems small because of the very short duration of the deceleration spike.

Along the trajectory below the projectile, there is no movement of the soil. Thus τ_{rz} is equal to zero at the center line. From the Mohr circle, Figure 11, it can be seen that the direction of flow β_s is $\frac{\pi}{4} - \frac{\phi}{2}$ and the pseudo direction of yield or flow $\beta_n = \beta_s + \frac{\pi}{2} + \phi$

³⁸R. O. Hultgren, L. J. Thompson, and D. G. Kitzinger, State of Stress in an Elastic Earth Target Resting on a Rigid Half-Space. Sandia Corporation, Albuquerque, New Mexico, Research Report 64-1734, May 1965.

when τ_{rz} is equal to zero. The nose on a blunt nosed projectile as seen in the two and three dimensional tests has edge slopes near these angles. In Figure 74a it can be seen that the equation of the edge of the nose cone is

$$z = \frac{R_p - r}{\tan\left(\frac{\pi}{4} - \frac{\phi}{2}\right)} + d \quad (\text{III-2a})$$

for

$$d \leq z \leq \frac{R_p}{\tan\left(\frac{\pi}{4} - \frac{\phi}{2}\right)}$$

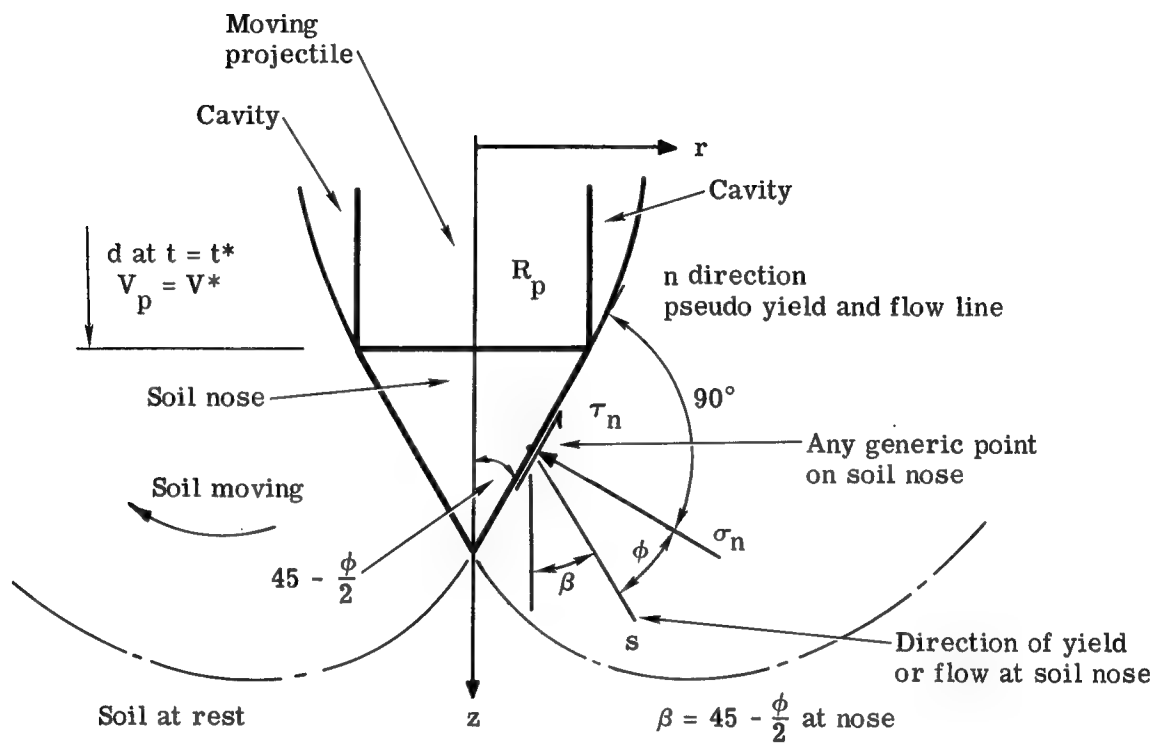
and

$$0 \leq r \leq R_p$$

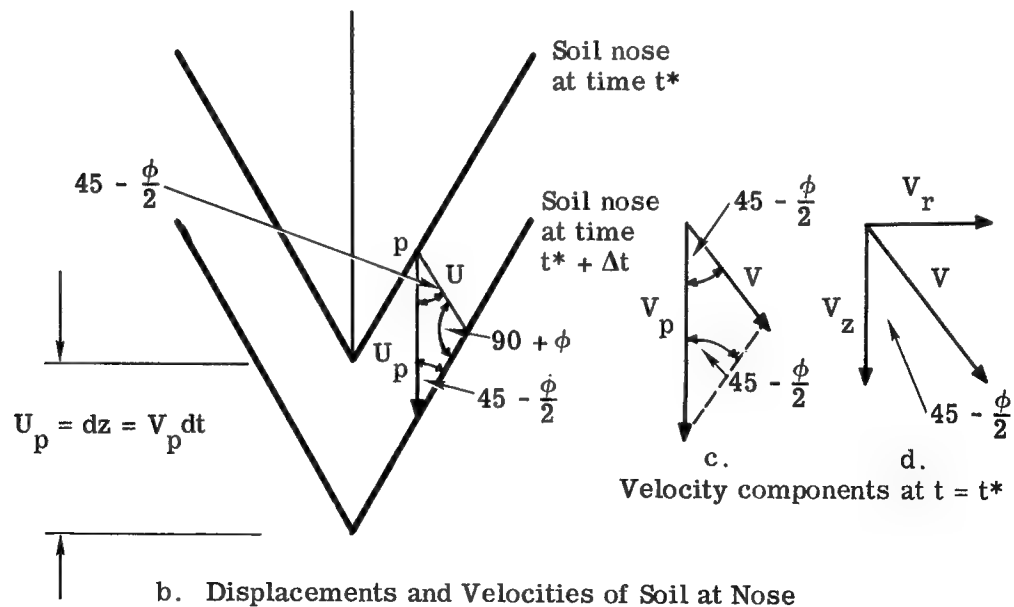
The mass of the soil cone does not change with time; therefore, M_c is constant.

The equation for M_c , the conical mass of the soil carried along with a blunt nosed projectile, is

$$M_c = \rho \frac{\pi}{3} \frac{R_p^3}{\tan\left(\frac{\pi}{4} - \frac{\phi}{2}\right)} \quad (\text{III-2b})$$



a. Stresses and Direction of Flow Lines at Nose



b. Displacements and Velocities of Soil at Nose

Figure 74. State of Stress and Velocity at the Soil Nose

4. As the projectile impacts, the soil is pushed down and outward. In the short interval of time it takes the projectile to pass through the interface, the soil particles go from zero velocity to some high velocity. The direction of motion during this short interval seems to follow a log spiral centered at the edge of the face of the blunt nosed projectile. In order to separate out the interface effects, it looks reasonable to assume for initial conditions that

- a. The soil nose has formed,
- b. The direction of the velocity of the soil particles follows a log spiral centered on the edge of the projectile face. Below the log spiral that has an initial radius of the length of the side of the point, no motion is occurring. The velocity of the soil particles is a function of the velocity of the projectile and position of the particles only.
- c. The projectile is moving at a velocity V_o which is less than the velocity V_i before impact.

A lower bound on the change in velocity at the interface can be obtained if it is assumed the soil offers no resistance to the movement of the soil nose formed. If the soil offers no resistance, momentum would be conserved and

$$V_o = \frac{M_p}{M_p + M_c} V_i$$

Actually the target resistance at time of impact is high so this is a poor approximation, and momentum is not conserved; thus

$$V_o \leq \frac{M_p}{M_p + M_c} V_i \quad (\text{III-3a})$$

Or the velocity just after impact can be assumed as

$$V_o = \frac{k M_p V_i}{M_p + \rho \frac{\pi}{3} \frac{R_p^3}{\tan\left(\frac{\pi}{4} - \frac{\phi}{2}\right)}} \quad (\text{III-3b})$$

where k depends on the nose shape, projectile diameter, target soil, and even perhaps V_i

5. After the projectile has entered the soil, the stresses on the soil nose can be found from the Mohr diagram when its shape is known. From Figure 11 and from Equations II-34, II-35, and II-36 it can be seen that

$$\sigma_z = \sigma_s + \left[C + \sigma_s \tan \phi + K \left(\frac{\partial V_r}{\partial z} + \frac{\partial V_z}{\partial r} \right) \right] \left[\frac{1 + \sin \phi}{\cos \phi} \right]$$

$$\sigma_r = \sigma_\psi = \sigma_s - \left[C + \sigma_s \tan \phi + K \left(\frac{\partial V_r}{\partial z} + \frac{\partial V_z}{\partial r} \right) \right] \left[\frac{1 - \sin \phi}{\cos \phi} \right]$$

$$\tau_{rz} = 0$$

$$\text{when } \beta = \frac{\pi}{4} - \frac{\phi}{2}$$

The shear stress parallel to the soil nose is τ_n and the stress normal to soil nose is σ_n . But from Equation II-32 and the Mohr circle in Figure 11 it is seen that

$$\tau_n = C + \sigma_n \tan \phi + K \left(\frac{\partial V_r}{\partial z} + \frac{\partial V_z}{\partial r} \right) \quad (\text{III-4})$$

$$\sigma_n = \sigma_s$$

where the direction of s is β_s and the direction of n is $\beta_s + \frac{\pi}{2} + \phi$, since both s and n are yield and flow lines.

As shown in Figure 74a the vertical component of τ_n is

$$\tau_{nz} = \tau_n \cos \left(\frac{\pi}{4} - \frac{\phi}{2} \right)$$

and the vertical component of σ_n is

$$\sigma_{nz} = \sigma_s \sin \left(\frac{\pi}{4} - \frac{\phi}{2} \right)$$

The sum $\tau_{nz} + \sigma_{nz}$ is the vertical force on the differential area element dA of the soil nose. Since the cone is symmetric about the centerline z , dA can be taken as the area of a strip dz in height around the nose where

$$dA = 2\pi r \frac{dz}{\cos \left(\frac{\pi}{4} - \frac{\phi}{2} \right)}$$

or

160

$$dA = 2\pi \csc\left(\frac{\pi}{4} - \frac{\phi}{2}\right) r dr$$

since

$$\frac{dr}{dz} = \tan\left(\frac{\pi}{4} - \frac{\phi}{2}\right) \text{ at the nose}$$

The total force on the nose, F , is the integral of the forces on the differential areas. Thus

$$F = 2\pi \int_{r=0}^{r=R} p \left[\sigma_s + \tau_n \cot\left(\frac{\pi}{4} - \frac{\phi}{2}\right) \right] r dr \quad (\text{III-5})$$

By substitution of Equation III-4

$$F = 2\pi \int_{r=0}^{r=R} p \left[\sigma_s \left(1 + \tan \phi \cot\left(\frac{\pi}{4} - \frac{\phi}{2}\right) \right) + C' \cot\left(\frac{\pi}{4} - \frac{\phi}{2}\right) \right] r dr \quad (\text{III-6})$$

where σ_s is as function of depth and velocity of the projectile and position on soil nose cone at any instant of time.

6. Since the sides of the soil cone seem to be straight except at the point, the flow lines must be parallel to each other. Then over the whole nose the angle β_s to the s line (direction of flow) is $\frac{\pi}{4} - \frac{\phi}{2}$ and the angle β_n to n line is $\beta_s + \frac{\pi}{2} + \phi$. If the flow lines are parallel at the surface of the cone, the velocity vectors of the soil being displaced must be uniform over the nose. All points on the nose move down the same distance during the short time interval Δt .

The distance the soil particles move is U in the direction

$\beta = \frac{\pi}{4} - \frac{\phi}{2}$. Since $\frac{dU}{dt} = V$ it can be seen in Figure 74b, c, and d, that

$$V = \frac{V_p}{2 \cos\left(\frac{\pi}{4} - \frac{\phi}{2}\right)} \text{ in the direction } \beta = 45 - \frac{\phi}{2} \quad (\text{III-7})$$

and that

$$\begin{aligned} V_z &= \frac{V_p}{2} \\ V_r &= \frac{V_p}{2} \tan\left(\frac{\pi}{4} - \frac{\phi}{2}\right) \end{aligned} \quad (\text{III-8})$$

As the blunt nose projectile travels through soil, there seems to be little friction on the sides of the projectile. An open cavity surrounds the projectile except at the nose. Along the edge of the cavity

$$\tau_{ns} = 0 \quad (\text{III-9})$$

$$\sigma_n = 0$$

and

$$V_n = 0$$

where the direction s is along the cavity and the direction n is normal to the surface of the cavity.

A reasonable assumption for the equation of the cavity seems to be

$$r = R_p + (d - z) k \quad (\text{III-10})$$

where $z \leq d$, $r \geq R_p$ and k is constant and between $\tan\left(\frac{\pi}{4} - \frac{\phi}{2}\right)$ and zero.

To obtain stability of the projectile, its length must be several times its diameter so that it does not tumble in the cavity. Possibly the length to diameter ratio must be at least 7 or 8 to 1 to obtain the desired stability for large projectiles.

8. For the penetration hole to remain open, the soil must arch around the cavity created by the projectile. This only happens if the soil has some cohesive strength. After the projectile has stopped, the hole remaining open in the soil is somewhat smaller than the projectile. Therefore, on the surface of the projectile, there are normal forces which cause frictional forces that resist removal of the projectile; but these forces do not seem to exist during penetration, since, in the case of the blunt nosed projectile, the paint is not removed even though soil is stuck to the projectile.

9. The stress σ_z and τ_{rz} are zero at the surface. Thus σ_z is the minimum principal stress and equal to σ_ψ . The cracks at the surface show that the radial normal stress has exceeded the strength of the soil in tension or that σ_ψ is equal to zero.

10. The volume of the soil raised at the surface is about the same as the volume of the hole created by the projectile.

The heave of soil at the surface shows that the assumption that the density is constant is not unrealistic.

11. The motion of the target in the two-dimensional tests, as well as the length of surface cracks and surface deformations in the full scale tests indicate that the phenomenon of penetration is primarily one of shear deformation, if the soil density is above critical density. There seems to be a shear front that travels with the projectile. The equation of the leading edge of the front seems to be a log spiral in the case of a blunt nosed projectile penetrating a half space. For other types of targets, the equation of the shear front probably depends on the boundary constraints.

The motion of the particles in the two-dimensional tests indicates that the shear front translates with the projectile and that the velocity of the target particles is a function of the position and velocity of the projectile.

For pure translation of the velocity field, which is a function of the velocity of the projectile, the components of the velocity field can be written

$$V_r = f_1(r, z, V_p) \quad V_z = f_2(r, z, V_p)$$

where V_p can be treated as a constant over the whole field at an instant of time.

The acceleration terms for the field particles are then

$$\frac{dV_r}{dt} = \frac{\partial V_r}{\partial r} \frac{dr}{dt} + \frac{\partial V_r}{\partial z} \frac{dz}{dt}$$

and

$$\frac{dV_z}{dt} = \frac{\partial V_z}{\partial r} \frac{dr}{dt} + \frac{\partial V_z}{\partial z} \frac{dz}{dt}$$

For translation of the velocity field in the z direction, derivatives with respect to r are zero, and $\frac{dz}{dt} = V_p$, thus

$$\frac{dV_r}{dt} = V_p \frac{\partial V_r}{\partial z} \quad (\text{III-11})$$

and

$$\frac{dV_z}{dt} = V_p \frac{\partial V_z}{\partial z} \quad (\text{III-12})$$

12. It is observed that there is a discontinuity in the displacement and velocity fields below the point and to the side of the soil that is moved. This discontinuity defines the shear front. On the edge of this discontinuity, the velocity components are zero.

13. It can be seen from the two-dimensional test photographs that at any instant of time the displacement of the particles is very similar to the displacements initially approximated by Prandtl for the indentation of an infinitely long footing or punch into a half space of rigid-plastic weightless material. There is a zone of material below the projectile that has not been influenced by the presence of the projectile. If the movement of the target particles is along a log spiral centered on the edge of the projectile, then there can be no velocity component perpendicular to the log spiral.

If the soil does move at each instant of time along a log spiral centered on the edge of the projectile, the velocity field can be calculated as follows.

Let $x = A q e^{\omega \tan \phi}$ where x is a new variable,

$$A \text{ is a constant} = e^{\left(\frac{\pi}{4} - \frac{\phi}{2}\right) \tan \phi}$$

and ω is a new variable such that

$$\omega + \frac{\pi}{4} = \beta + \phi.$$

From Figure 75 it can be seen that

$$r = R_p + x \sin \omega = R_p + \sin \omega (A q e^{\omega \tan \phi}) \quad (\text{III-13})$$

$$z = d + x \cos \omega = d + \cos \omega (A q e^{\omega \tan \phi}) \quad (\text{III-14})$$

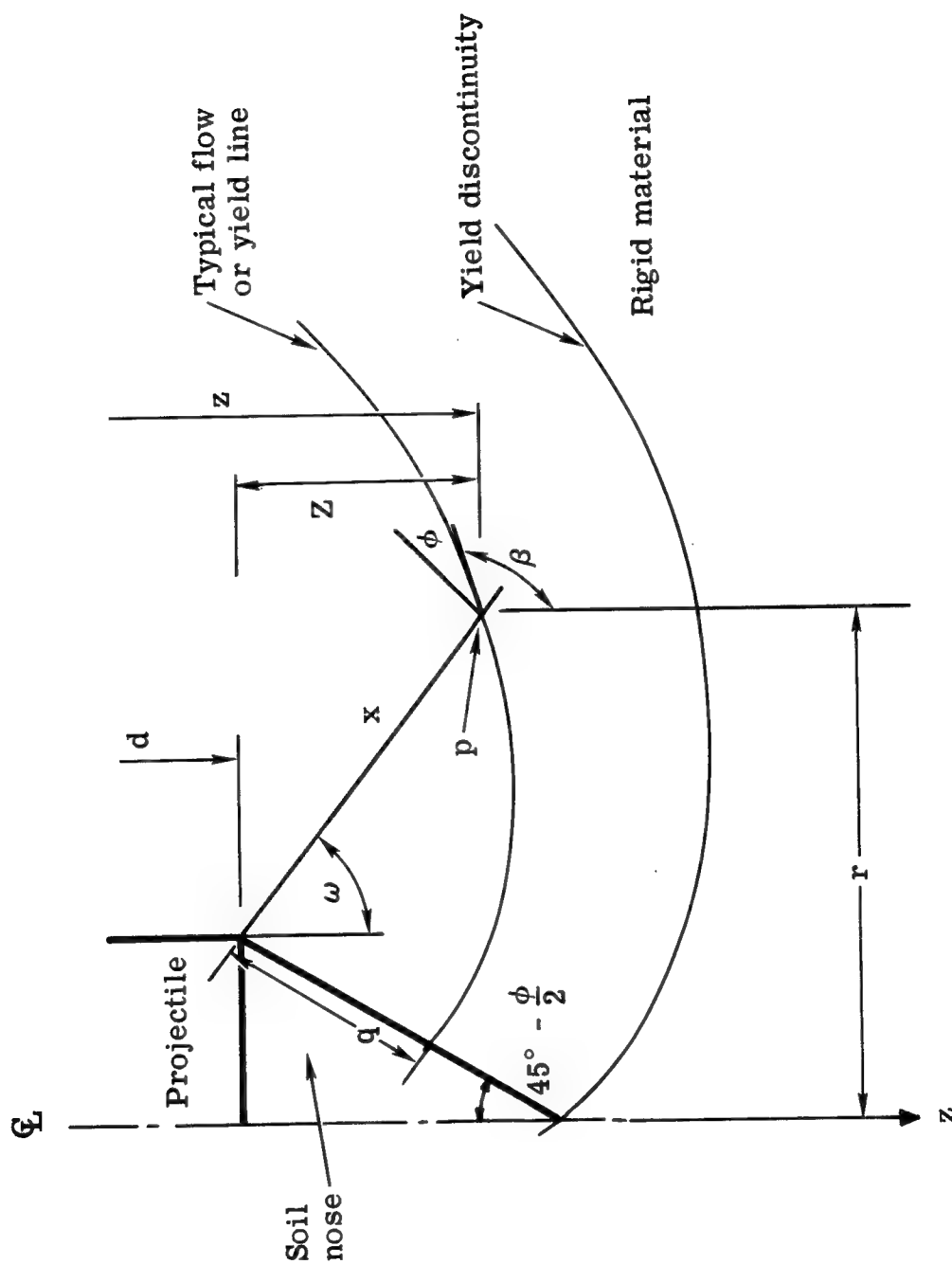


Figure 75. Assumed Direction of Flow Lines at an Instant of Time

By taking the partial derivative of Equations III-13 and III-14 with respect to r , the two following equations are obtained.

$$\frac{\partial q}{\partial r} + (\tan \phi + \cot \omega) q \frac{\partial \omega}{\partial r} = \frac{1}{A \sin \omega e^{\omega \tan \phi}} \quad (\text{III-15})$$

and

$$\frac{\partial q}{\partial r} + (\tan \phi - \tan \omega) q \frac{\partial \omega}{\partial r} = 0 \quad (\text{III-16})$$

Solving simultaneously Equations III-15 and III-16

$$\left. \begin{aligned} \frac{\partial \omega}{\partial r} &= \frac{\cos \omega}{q A e^{\tan \phi}} \\ \frac{\partial q}{\partial r} &= -\frac{\cos \omega \tan \phi}{A e^{\omega \tan \phi}} + \frac{\sin \omega}{A e^{\omega \tan \phi}} \end{aligned} \right\} \quad (\text{III-17})$$

Taking the partial derivative of Equations III-13 and III-14 with respect to z

$$\frac{\partial q}{\partial z} + (\tan \phi + \cot \omega) q \frac{\partial \omega}{\partial z} = 0$$

and

$$\frac{\partial q}{\partial z} + (\tan \phi - \tan \omega) q \frac{\partial \omega}{\partial z} = \frac{1}{A \cos \omega e^{\omega \tan \phi}}$$

Using elimination

$$\left. \begin{aligned} \frac{\partial \omega}{\partial z} &= - \frac{\sin \omega}{q A e^{\omega \tan \phi}} \\ \frac{\partial q}{\partial z} &= \frac{\sin \omega \tan \phi}{A e^{\omega \tan \phi}} + \frac{\cos \omega}{A e^{\omega \tan \phi}} \end{aligned} \right\} \quad (\text{III-18})$$

since

$$\beta = \omega + \frac{\pi}{2} - \phi$$

$$\frac{\partial \beta}{\partial r} = \frac{\partial \omega}{\partial r} \text{ and } \frac{\partial \beta}{\partial z} = \frac{\partial \omega}{\partial z}$$

The continuity equation with $\rho = 0$ is

$$\frac{\partial V_r}{\partial r} + \frac{V_r}{r} + \frac{\partial V_z}{\partial z} = 0 \quad (\text{II-19})$$

where V_r and V_z are functions of q and ω at any instant of time, thus

$$\frac{\partial V_r}{\partial q} \frac{\partial q}{\partial r} + \frac{\partial V_r}{\partial \omega} \frac{\partial \omega}{\partial r} + \frac{V_r}{r} + \frac{\partial V_z}{\partial q} \frac{\partial q}{\partial z} + \frac{\partial V_z}{\partial \omega} \frac{\partial \omega}{\partial z} = 0$$

But

$$\left. \begin{aligned} V_r &= V \sin \beta = V \sin \left(\omega + \frac{\pi}{2} - \phi \right) = V \cos(\omega - \phi) \\ V_z &= V \cos \beta = V \cos \left(\omega + \frac{\pi}{2} - \phi \right) = -V \sin(\omega - \phi) \end{aligned} \right\} \quad (\text{III-19})$$

thus

$$\left. \begin{aligned} \frac{\partial V_r}{\partial q} &= \cos(\omega - \phi) \frac{\partial V}{\partial q} \\ \frac{\partial V_r}{\partial \omega} &= \cos(\omega - \phi) \frac{\partial V}{\partial \omega} - V \sin(\omega - \phi) \\ \frac{\partial V_z}{\partial q} &= -\sin(\omega - \phi) \frac{\partial V}{\partial q} \\ \frac{\partial V_z}{\partial \omega} &= -\sin(\omega - \phi) \frac{\partial V}{\partial \omega} - V \cos(\omega - \phi) \end{aligned} \right\} \quad (\text{III-20})$$

By substituting Equations III-17, III-18 and III-20 into the continuity Equation, II-19, the following equation is obtained.

$$\begin{aligned} &\cos(\omega - \phi) \frac{\partial V}{\partial q} \frac{\partial q}{\partial r} + \left[\cos(\omega - \phi) \frac{\partial V}{\partial \omega} - V \sin(\omega - \phi) \right] \frac{\partial \omega}{\partial r} + \frac{V}{r} \cos(\omega - \phi) \\ &- \sin(\omega - \phi) \frac{\partial V}{\partial q} \frac{\partial q}{\partial z} - \left[\sin(\omega - \phi) \frac{\partial V}{\partial \omega} + V \cos(\omega - \phi) \right] \frac{\partial \omega}{\partial z} = 0 \end{aligned}$$

or

$$\begin{aligned} &\frac{\partial V}{\partial q} \left[\frac{\cos(\omega - \phi)(\sin \omega - \cos \omega \tan \phi) - \sin(\omega - \phi)(\cos \omega + \sin \omega \tan \phi)}{A e^{\omega \tan \phi}} \right] \\ &+ \frac{\partial V}{\partial \omega} \left[\frac{\cos(\omega - \phi)(\cos \omega) + \sin(\omega - \phi)(\sin \omega)}{q A e^{\omega \tan \phi}} \right] \\ &+ V \left(\frac{\cos(\omega - \phi)}{r} - \frac{\sin(\omega - \phi) \cos \omega}{q A e^{\omega \tan \phi}} + \frac{\cos(\omega - \phi) \sin \omega}{q A e^{\omega \tan \phi}} \right) = 0 \end{aligned}$$

which reduces to

$$\frac{\partial V}{\partial \omega} \frac{\cos \phi}{q A e^{\omega \tan \phi}} + V \left(\frac{\cos(\omega - \phi)}{r} + \frac{\sin \phi}{q A e^{\omega \tan \phi}} \right) = 0$$

or

$$\frac{1}{V} \frac{\partial V}{\partial \omega} + \tan \phi + \frac{\cos(\omega - \phi)}{\cos \phi} \cdot \frac{q A e^{\omega \tan \phi}}{R_p + A q e^{\omega \tan \phi}} = 0 \quad (\text{III-21})$$

Since

$$r = R_p + A q e^{\omega \tan \phi} \sin \omega$$

and

$$\frac{\partial r}{\partial \omega} = A q e^{\omega \tan \phi} \cos \omega + A q e^{\omega \tan \phi} \sin \omega \tan \phi$$

then

$$\frac{1}{V} \frac{\partial V}{\partial \omega} + \tan \phi + \frac{1}{r} \frac{\partial r}{\partial \omega} = 0 \quad (\text{III-22})$$

Integrating with respect to ω , it is found that

$$\ln V + \omega \tan \phi + \ln r + f(q) = 0, \text{ or}$$

$$V = e^{-\omega \tan \phi} e^{-\ln r} e^{-f(q)}, \text{ which reduces to}$$

$$V = \frac{e^{-\omega \tan \phi} e^{-f(q)}}{r} \quad (\text{III-23})$$

At the soil nose

$$V = \frac{V_p}{2 \cos\left(\frac{\pi}{4} - \frac{\phi}{2}\right)} \quad \text{for} \quad 0 \leq q \leq \frac{R_p}{\tan\left(\frac{\pi}{4} - \frac{\phi}{2}\right)} \quad (\text{III-24})$$

where $\omega = -\left(\frac{\pi}{4} - \frac{\phi}{2}\right)$

Then

$$\frac{V_p}{2 \cos\left(\frac{\pi}{4} - \frac{\phi}{2}\right)} = \frac{e^{\left(\frac{\pi}{4} - \frac{\phi}{2}\right) \tan \phi} e^{-f(q)}}{R_p - A q e^{-\left(\frac{\pi}{4} - \frac{\phi}{2}\right) \tan \phi} \sin\left(\frac{\pi}{4} - \frac{\phi}{2}\right)}, \text{ or}$$

$$\frac{V_p}{2 \cos\left(\frac{\pi}{4} - \frac{\phi}{2}\right)} = \frac{A e^{-f(q)}}{R_p - q \sin\left(\frac{\pi}{4} - \frac{\phi}{2}\right)}$$

$$e^{-f(q)} = \frac{V_p}{2 A \cos\left(\frac{\pi}{4} - \frac{\phi}{2}\right)} \left[R_p - q \sin\left(\frac{\pi}{4} - \frac{\phi}{2}\right) \right]$$

Then

$$V = \frac{e^{-\omega \tan \phi}}{r} \frac{V_p}{2 A \cos\left(\frac{\pi}{4} - \frac{\phi}{2}\right)} \left[R_p - q \sin\left(\frac{\pi}{4} - \frac{\phi}{2}\right) \right]$$

$$V = \frac{V_p h}{B e^{\omega \tan \phi} r} \quad (\text{III-25})$$

where $h = R_p - q \sin\left(\frac{\pi}{4} - \frac{\phi}{2}\right)$

$$B = 2 A \cos\left(\frac{\pi}{4} - \frac{\phi}{2}\right)$$

$$r = R_p + A q e^{\omega \tan \phi} \sin \omega$$

$$V_r = \frac{V_p h \cos(\omega - \phi)}{B e^{\omega \tan \phi} r} \quad (\text{III-26})$$

$$V_z = \frac{V_p h \sin \omega - \phi}{B e^{\omega \tan \phi} r} \quad (\text{III-27})$$

when the velocity of the projectile V_p is equal to the velocity after impact V_o

$$-\frac{\pi}{4} + \frac{\phi}{2} \leq \omega \leq \frac{\pi}{2}$$

By substituting V_o for V_p into Equation III-21 and allowing ω to vary between $-\pi/4 + \phi/2$ and $\pi/2$, the initial velocity field can be established. When $V_p = 0$ the projectile has stopped. The assumed log spiral deformation and velocity field require that V_r and V_z be zero at this time.

It is also observed from the two-dimensional studies that when ω is between $\pi/2 + \phi$ and $\pi/4 + 3\phi/2$ that the soil leaves the log spiral motion and moves upward and outward in an almost straight line parallel

to the side of the cavity. The above limits for ω correspond to β by being between π and $3\pi/4 + \phi/2$.

If the soil does move along lines in which β is constant, then the velocity field above the log spiral area can be calculated as follows.

Let

$$r = R_p + Q \cos (\phi - \alpha) + W \sin \alpha \quad (\text{III-28})$$

$$z = d - Q \sin (\phi - \alpha) - W \cos \alpha \quad (\text{III-29})$$

As shown in Figure 76, V_r and V_z then would be functions of Q and W and at an instant of time. Thus

$$\frac{\partial V}{\partial r} = \frac{\partial V}{\partial Q} \frac{\partial Q}{\partial r} + \frac{\partial V}{\partial W} \frac{\partial W}{\partial r}$$

and

$$\frac{\partial V}{\partial z} = \frac{\partial V}{\partial Q} \frac{\partial Q}{\partial z} + \frac{\partial V}{\partial W} \frac{\partial W}{\partial z}$$

Also

$$V_r = V \sin \beta = V \sin (\pi - \alpha) = V \sin \alpha$$

$$V_z = V \cos \beta = V \cos (\pi - \alpha) = -V \cos \alpha$$

where α is a constant between 0 and $\pi/4 - \phi/2$.

The continuity equation (II-19) can be rewritten

$$\sin \alpha \left(\frac{\partial V}{\partial Q} \frac{\partial Q}{\partial r} + \frac{\partial V}{\partial W} \frac{\partial W}{\partial r} \right) + \frac{V \sin \alpha}{r} - \cos \alpha \left(\frac{\partial V}{\partial Q} \frac{\partial Q}{\partial z} + \frac{\partial V}{\partial W} \frac{\partial W}{\partial z} \right) = 0$$

or

$$\frac{\partial V}{\partial Q} \left(\frac{\partial Q}{\partial r} - \cot \alpha \frac{\partial Q}{\partial z} \right) + \frac{\partial V}{\partial W} \left(\frac{\partial W}{\partial r} - \cot \alpha \frac{\partial W}{\partial z} \right) + \frac{V}{r} = 0 \quad (\text{III-30})$$

The partial derivative, $\partial Q/\partial r$, $\partial Q/\partial z$, $\partial W/\partial r$, $\partial W/\partial z$ can be evaluated as follows. Taking the partial derivative of Equations III-28 and III-29 with respect to r ,

$$\frac{\partial r}{\partial r} = 1 = \cos (\phi - \alpha) \frac{\partial Q}{\partial r} + \sin \alpha \frac{\partial W}{\partial r}$$

$$\frac{\partial z}{\partial r} = 0 = -\sin (\phi - \alpha) \frac{\partial Q}{\partial r} - \cos \alpha \frac{\partial W}{\partial r}$$

and solving simultaneously

$$\left. \begin{aligned} \frac{\partial Q}{\partial r} &= \frac{\cos \alpha}{\cos \phi} \\ \frac{\partial W}{\partial r} &= -\frac{\sin (\phi - \alpha)}{\cos \phi} \end{aligned} \right\} \quad (\text{III-31})$$

Taking the partial derivative of Equations III-28 and III-29 with respect to z ,

$$\frac{\partial r}{\partial z} = 0 = \cos(\phi - \alpha) \frac{\partial Q}{\partial z} + \sin \alpha \frac{\partial W}{\partial z}$$

$$\frac{\partial z}{\partial z} = 1 = -\sin(\phi - \alpha) \frac{\partial Q}{\partial z} - \cos \alpha \frac{\partial W}{\partial z}$$

and solving simultaneously

$$\left. \begin{aligned} \frac{\partial Q}{\partial z} &= \frac{\sin \alpha}{\cos \phi} \\ \frac{\partial W}{\partial z} &= -\frac{\cos \phi - \alpha}{\cos \phi} \end{aligned} \right\} \quad (\text{III-32})$$

Substitution of Equations III-31 and III-32 into Equation III-30 yields

$$\begin{aligned} & \frac{\partial V}{\partial Q} \left(\frac{\cos \alpha}{\cos \phi} - \frac{\cos \alpha \sin \alpha}{\sin \alpha \cos \phi} \right) \\ & - \frac{\partial V}{\partial W} \left(\frac{\sin(\phi - \alpha)}{\cos \phi} - \frac{\cos \alpha \cos(\phi - \alpha)}{\sin \alpha \cos \phi} \right) + \frac{V}{r} = 0 \end{aligned}$$

which reduces to

$$\frac{1}{\sin \alpha} \frac{\partial V}{\partial W} + \frac{V}{r} = 0$$

or

$$\frac{1}{V} \frac{\partial V}{\partial W} + \frac{\sin \alpha}{r} = 0 \quad (\text{III-33})$$

Since

$$r = R_p + Q \cos(\phi - \alpha) + W \sin \alpha$$

and

$$\frac{\partial r}{\partial W} = \sin \alpha$$

then Equation III-33 can be rewritten

$$\frac{1}{V} \frac{\partial V}{\partial W} + \frac{1}{r} \frac{\partial r}{\partial W} = 0 \quad (\text{III-34})$$

Integrating Equation III-34 with respect to W it is found that

$$\ln V + \ln r + f(Q) = 0$$

or

$$V = e^{-\ln r} \cdot e^{-f(Q)} = \frac{e^{-f(Q)}}{r} \quad (\text{III-35})$$

when $\omega = \pi/2 + \phi - \alpha$, Equation III-25 can be written

$$V = \frac{e^{-\left(\frac{\pi}{2} + \phi - \alpha\right) \tan \phi} V_p \left[R_p - q \sin\left(\frac{\pi}{4} - \frac{\phi}{2}\right) \right]}{2rA \left(\cos \frac{\pi}{4} - \frac{\phi}{2} \right)} \quad (\text{III-36})$$

where

$$Q = Aq e^{\left(\frac{\pi}{2} + \phi - \alpha\right)}$$

or

$$q = \frac{Q}{A e^{\left(\frac{\pi}{2} + \phi - \alpha\right)}}$$

Equation III-36 allows the evaluation of $e^{-f(Q)}$. When $\omega = \pi/2 + \phi - \alpha$

Equation III-36 must equal Equation III-35, thus

$$V = \frac{e^{-f(Q)}}{r} = \frac{e^{-\left(\frac{\pi}{2} + \phi - \alpha\right) \tan \phi} V_p \left[R_p - q \sin\left(\frac{\pi}{4} - \frac{\phi}{2}\right) \right]}{2rA \cos\left(\frac{\pi}{4} - \frac{\phi}{2}\right)}$$

and

$$e^{-f(Q)} = \frac{e^{-\left(\frac{\pi}{2} + \phi - \alpha\right) \tan \phi} V_p \left[R_p - q \sin\left(\frac{\pi}{4} - \frac{\phi}{2}\right) \right]}{2A \cos\left(\frac{\pi}{4} - \frac{\phi}{2}\right)} \quad (\text{III-37})$$

Substituting Equation III-37 into Equation III-35, the velocity is found for Area II where the soil is moving parallel to the cavity

$$V_{II} = \frac{e^{-\left(\frac{\pi}{2} + \phi - \alpha\right) \tan \phi} V_p \left[R_p - q \sin\left(\frac{\pi}{4} - \frac{\phi}{2}\right) \right]}{2rA \cos\left(\frac{\pi}{4} - \frac{\phi}{2}\right)} \quad (\text{III-38})$$

CHAPTER IV

SUMMARY OF GOVERNING DIFFERENTIAL EQUATIONS AND REQUIRED BOUNDARY CONDITIONS

I. SUMMATION OF EQUATIONS

Governing equations from continuum mechanics are as follows:

$$1. \quad (M_p + M_c) g - F = (M_p + M_c) \frac{dV_p}{dt} \quad (\text{Eq. I-1})$$

or

$$(M_p + M_c) g - F = (M_p + M_c) V_p \frac{dV_p}{dz}$$

which can be integrated from a small increment of time after impact when the velocity of the projectile is equal to V_0 and the depth z is equal to zero to the time when the velocity of the projectile is zero and the depth of penetration is a maximum.

$$2. \quad F = \int_S \bar{\rho} \, da \quad (\text{Eq. II-20})$$

$$3. \quad -\frac{\partial \sigma_r}{\partial r} - \frac{\partial \tau_{rz}}{\partial z} - \left(\frac{\sigma_r - \sigma_\psi}{r} \right) = \left(\frac{\partial V}{\partial t} + V_r \frac{\partial V}{\partial r} + V_z \frac{\partial V}{\partial z} \right) \rho \quad (\text{Eq. II-10})$$

$$4. \quad -\frac{\partial \tau_{rz}}{\partial r} - \frac{\partial \sigma_z}{\partial z} - \frac{\tau_{rz}}{r} + \rho g = \left(\frac{\partial V}{\partial t} + V_r \frac{\partial V}{\partial r} + V_z \frac{\partial V}{\partial z} \right) \rho \quad (\text{Eq. II-11})$$

$$5. \quad \frac{d\rho}{dt} + \rho \left(\frac{\partial V}{\partial r} + \frac{V}{r} + \frac{\partial V}{\partial z} \right) = 0 \quad (\text{Eq. II-18})$$

Constitutive equations are as follows:

$$6. \quad \sigma_z = \sigma_s + \left[C + \sigma_s \tan \phi + K \left(\frac{\partial V}{\partial z} + \frac{\partial V}{\partial r} \right) \right] \left[\frac{2 \cos \beta \sin(\beta + \phi)}{\cos \phi} \right]$$

(Eq. II-34)

$$7. \quad \sigma_r = \sigma_s - \left[C + \sigma_s \tan \phi + K \left(\frac{\partial V}{\partial z} + \frac{\partial V}{\partial r} \right) \right] \left[\frac{2 \sin \beta \cos(\beta + \phi)}{\cos \phi} \right]$$

(Eq. II-35)

$$8. \quad \tau_{rz} = - \left[C + \sigma_s \tan \phi + K \left(\frac{\partial V}{\partial z} + \frac{\partial V}{\partial r} \right) \right] \left[\frac{\cos(2\beta + \phi)}{\cos \phi} \right]$$

(Eq. II-36)

$$9. \quad \tan \beta = \frac{V_r}{V_z} \quad (\text{Eq. II-39})$$

$$10. \quad \rho = \text{constant} \quad (\text{Eq. II-42})$$

$$11. \quad \sigma_{\psi} = \sigma_s + \left[C + \sigma_s \tan \phi + K \left(\frac{\partial V_r}{\partial z} + \frac{\partial V_z}{\partial r} \right) \right] \left[\frac{\sin \phi - 1}{\cos \phi} \right]$$

(Eq. II-40)

Equations from the mechanism studies are as follows:

$$12. \quad M_c = \rho \frac{\pi}{3} \frac{R_p^3}{\tan(45^\circ - \frac{\phi}{2})} \quad (\text{Eq. III-2b})$$

$$13. \quad F = 2\pi \int_{r=0}^{r=R_p} \left\{ \sigma_s + \left[C + \sigma_s \tan \phi + K \left(\frac{\partial V_r}{\partial z} + \frac{\partial V_z}{\partial r} \right) \right] \cot \left(\frac{\pi}{4} - \frac{\phi}{2} \right) \right\} r \, dr$$

(Eq. III-6)

II. BOUNDARY AND INITIAL CONDITIONS

There are 13 equations with 13 unknowns. The initial velocity condition when $d = 0$, and $V_p = V_0$ for the soil outside the nose and above the shear front discontinuity is

$$V = \frac{V_p h}{B e^{\omega \tan \phi}} \quad (\text{Eq. III-21})$$

and

$$V_r = V \sin \beta$$

$$V_z = V \cos \beta$$

from Equation II-39. For the soil inside the soil nose, $V_z = V_0$ and $V_r = 0$. The soil nose is described by the equation

$$Z = \frac{R_p - r}{\tan \left(45^\circ - \frac{\phi}{2} \right)} + d \quad (\text{Eq. III-2a})$$

The final velocity condition is when $d = d_{\max}$ and $V_p = 0$.

The state of stress and velocity before impact is:

$$\left. \begin{aligned} \sigma_z &= z \\ \sigma_r &= z \\ \tau_{rz} &= 0 \\ V_r &= V_z = V = 0 \end{aligned} \right\} \quad (\text{Eq. III-1})$$

For all time during the event the boundary conditions for

a. the surface $z = 0$

$$\tau_{rz} = \sigma_z = 0$$

$$\sigma_r = \sigma_\psi$$

and

V_r , V_z and σ_r are unknown.

b. Along the cavity described by

$$r = R_p + (d - z) k \quad (\text{Eq. III-10})$$

$$\tau_{ns} = \sigma_n = V_n = 0 \quad (\text{Eq. III-9})$$

and

V_s and σ_s are unknown on this boundary.

c. Along the nose when the projectile is at depth d and velocity V_p , the velocity is uniform and given by

$$V = \frac{V_p h}{B e^{\omega \tan \phi}} \quad (\text{Eq. III-21})$$

where

$$\omega = -\frac{\pi}{4} + \frac{\phi}{2}$$

and

184

$$V_r = V \sin\left(\frac{\pi}{4} - \frac{\phi}{2}\right)$$

$$V_z = V \cos\left(\frac{\pi}{4} - \frac{\phi}{2}\right)$$

σ_s is unknown on this boundary.

d. There is a shear front which travels with the projectile; the equation for the shear front is unknown theoretically, but outside this front where $V_r = V_z = 0$, the boundary stresses along the front can be obtained from Equations II-34, II-35, II-36, and II-41.

$$\sigma_z = \sigma_s + (C + \sigma_s \tan \phi) \frac{2 \cos \beta \sin (\beta + \phi)}{\cos \phi}$$

$$\sigma_r = \sigma_s - (C + \sigma_s \tan \phi) \frac{2 \sin \beta \cos (\beta + \phi)}{\cos \phi}$$

$$\sigma_\psi = \sigma_s + (C + \sigma_s \tan \phi) \left[\frac{\sin \phi - 1}{\cos \phi} \right]$$

$$\tau_{rz} = -(C + \sigma_s \tan \phi) \frac{\cos (2\beta + \phi)}{\cos \phi}$$

$$V_r = V_z = 0 \quad .$$

The above 13 equations, the one initial condition, and the four boundary conditions completely describe the problem.

Outside the boundaries where the soil is at rest, i. e., when r or z is large, the initial conditions before impact prevail.

III. COMBINATION OF EQUATIONS

By differentiating Equation II-35 with respect to r , differentiating Equation II-34 with respect to z , and differentiating Equation II-36 once with respect to r and once with respect to z , the following equations are obtained.

$$\begin{aligned} \frac{\partial \sigma_r}{\partial r} = & \frac{\partial \sigma_s}{\partial r} - \frac{2 \sin \beta \cos (\beta + \phi)}{\cos \phi} \left[\tan \phi \frac{\partial \sigma_s}{\partial r} + K \left(\frac{\partial^2 V_r}{\partial r \partial z} + \frac{\partial^2 V_z}{\partial r^2} \right) \right] \\ & - \frac{2 \cos (2\beta + \phi)}{\cos \phi} \left[C + \sigma_s \tan \phi + K \left(\frac{\partial V_r}{\partial z} + \frac{\partial V_z}{\partial r} \right) \right] \left(\frac{\partial \beta}{\partial r} \right) \end{aligned}$$

(Eq. IV-1)

$$\begin{aligned} \frac{\partial \sigma_z}{\partial z} = & \frac{\partial \sigma_s}{\partial z} + \frac{2 \cos \beta \sin (\beta + \phi)}{\cos \phi} \left[\tan \phi \frac{\partial \sigma_s}{\partial z} + K \left(\frac{\partial^2 V_r}{\partial z^2} + \frac{\partial^2 V_z}{\partial r \partial z} \right) \right] \\ & + \frac{2 \cos (2\beta + \phi)}{\cos \phi} \left[C + \sigma_s \tan \phi + K \left(\frac{\partial V_r}{\partial z} + \frac{\partial V_z}{\partial r} \right) \right] \left[\frac{\partial \beta}{\partial z} \right] \end{aligned}$$

(Eq. IV-2)

$$\begin{aligned} \frac{\partial \tau_{rz}}{\partial z} = & - \frac{\cos (2\beta + \phi)}{\cos \phi} \left[\tan \phi \frac{\partial \sigma_2}{\partial z} + K \left(\frac{\partial^2 V_2}{\partial z^2} + \frac{\partial^2 V_2}{\partial_r \partial_z} \right) \right] \\ & + \frac{2 \sin (2\beta + \phi)}{\cos \phi} \left[C + \sigma_s \tan \phi + K \left(\frac{\partial V_r}{\partial z} + \frac{\partial V_z}{\partial_r} \right) \right] \frac{\partial \beta}{\partial z} \end{aligned}$$

(Eq. IV-3)

$$\begin{aligned} \frac{\partial \tau_{rz}}{\partial r} = & - \frac{\cos(2\beta + \phi)}{\cos \phi} \left[\tan \phi \frac{\partial \sigma_s}{\partial r} + K \left(\frac{\partial^2 V_r}{\partial r \partial z} + \frac{\partial^2 V_z}{\partial r^2} \right) \right] \\ & + \frac{2 \sin(2\beta + \phi)}{\cos \phi} \left[C + \sigma_s \tan \phi + K \left(\frac{\partial V_r}{\partial z} + \frac{\partial V_z}{\partial r} \right) \right] \frac{\partial \beta}{\partial r} \end{aligned}$$

(Eq. IV-4)

Subtracting Equation II-40 from Equation II-34 and dividing by $(-r)$ the following equation is obtained.

$$- \left(\frac{\sigma_r - \sigma_\psi}{r} \right) = \frac{1}{r} \left[C + \sigma_s \tan \phi + K \left(\frac{\partial V_r}{\partial z} + \frac{\partial V_z}{\partial r} \right) \right] \left[\frac{\sin(2\beta + \phi) - 1}{\cos \phi} \right]$$

(Eq. IV-5)

Substituting Equation IV-1, Equation IV-3 and Equation IV-5 into Equation II-10, the following equation of motion is obtained.

$$\begin{aligned} & - \frac{\partial \sigma_s}{\partial r} + \frac{2 \sin \beta \cos(\beta + \phi)}{\cos \phi} \left[\tan \phi \frac{\partial \sigma_s}{\partial r} + K \left(\frac{\partial^2 V_r}{\partial r \partial z} + \frac{\partial^2 V_z}{\partial r^2} \right) \right] \\ & + \frac{2}{\cos \phi} \cos(2\beta + \phi) \left[C + \sigma_s \tan \phi + K \left(\frac{\partial V_r}{\partial z} + \frac{\partial V_z}{\partial r} \right) \right] \frac{\partial \beta}{\partial r} \\ & + \frac{\cos(2\beta + \phi)}{\cos \phi} \left[\tan \phi \frac{\partial \sigma_s}{\partial z} + K \left(\frac{\partial^2 V_r}{\partial z^2} + \frac{\partial^2 V_z}{\partial r \partial z} \right) \right] \\ & - \frac{2 \sin(2\beta + \phi)}{\cos \phi} \left[C + \sigma_s \tan \phi + K \left(\frac{\partial V_r}{\partial z} + \frac{\partial V_z}{\partial r} \right) \right] \frac{\partial \beta}{\partial z} \end{aligned}$$

$$\begin{aligned}
& - \left[\frac{1 - \sin(2\beta + \phi)}{r \cos \phi} \right] \left[C + \sigma_s \tan \phi + K \left(\frac{\partial V_r}{\partial z} + \frac{\partial V_z}{\partial r} \right) \right] \\
& = \left(\frac{\partial V_r}{\partial t} + V_r \frac{\partial V_r}{\partial r} + V_z \frac{\partial V_r}{\partial z} \right) \rho \quad (\text{Eq. IV-6})
\end{aligned}$$

Substituting Equation IV-4, Equation IV-2, Equation II-36 into Equation II-11, the other equation of motion is obtained.

$$\begin{aligned}
& \frac{\cos(2\beta + \phi)}{\cos \phi} \left[\tan \phi \frac{\partial \sigma_s}{\partial r} + K \left(\frac{\partial^2 V_r}{\partial r \partial z} + \frac{\partial^2 V_z}{\partial r^2} \right) \right] \\
& - \frac{2 \sin(2\beta + \phi)}{\cos \phi} \left[C + \sigma_s \tan \phi + K \left(\frac{\partial V_r}{\partial z} + \frac{\partial V_z}{\partial r} \right) \right] \frac{\partial \beta}{\partial r} \\
& - \frac{\partial \sigma_s}{\partial z} - \frac{2 \cos \beta \sin(\beta + \phi)}{\cos \phi} \left[\tan \phi \frac{\partial \sigma_s}{\partial z} + K \left(\frac{\partial^2 V_r}{\partial z^2} + \frac{\partial^2 V_z}{\partial r \partial z} \right) \right] \\
& - \frac{2 \cos(2\beta + \phi)}{\cos \phi} \left[C + \sigma_s \tan \phi + K \left(\frac{\partial V_r}{\partial z} + \frac{\partial V_z}{\partial r} \right) \right] \frac{\partial \beta}{\partial z} \\
& + \frac{\cos(2\beta + \phi)}{r \cos \phi} \left[C + \sigma_s + K \left(\frac{\partial V_r}{\partial z} + \frac{\partial V_z}{\partial r} \right) \right] \\
& + \rho g = \left(\frac{\partial V_z}{\partial t} + V_r \frac{\partial V_z}{\partial r} + V_z \frac{\partial V_z}{\partial r} \right) \rho \quad (\text{Eq. IV-7})
\end{aligned}$$

By substituting Equations III-2b and III-6 into Equation I-1, the

$$\left[M_p + \rho \frac{\pi}{z} \frac{R_p^3}{\tan \frac{\pi}{4} - \frac{\phi}{2}} \right] \left[g - V_p \frac{dV_p}{dz} \right]$$

$$= 2\pi \int_{r=0}^{r=R_p} \left[\sigma_s \left(1 + \tan \phi \cot \left(\frac{\pi}{4} - \frac{\phi}{2} \right) \right) + C' \cot \left(\frac{\pi}{4} - \frac{\phi}{2} \right) \right] r \, dr$$

Eq. IV-8)

substituting into Equation II-18 to obtain Equation II-42

$$\frac{\partial V_r}{\partial r} + \frac{V_r}{r} + \frac{\partial V_z}{\partial z} = 0 \quad (\text{Eq. II-19})$$

Taking the five equations, II-38, II-19, IV-8, IV-6, and IV-7, it can be seen that the five unknowns are σ_s , V_r , V_z , β and V_p ; and the three independent variables are r , z and t . β can be eliminated, leaving four unknowns: This leaves the equation of motion of the projectile which requires the initial condition for a solution, the two second order equations of motion which require two boundary conditions, and the continuity condition which requires one boundary condition.

Theoretically no assumptions must be made concerning the velocity field in order to obtain a solution, but a closed form solution to four simultaneous partial differential equations, two of which are second order and two of which are first order, is difficult to obtain.

It may be possible to obtain a numerical solution to the governing differential equations using the "marker and cell" technique³⁸ on a high speed computer. This technique has been successfully used for plane strain incompressible viscous fluid problems, and has just recently been extended to axially symmetric problems.

³⁸Francis H. Harlow and J. Eddie Welch, "Numerical Study of Large Amplitude Free Surface Motions." This paper has been submitted for publication in The Physics of Fluids, authors are employed at Los Alamos Scientific Laboratory, Los Alamos, New Mexico.

CHAPTER V

CONCLUSIONS AND RECOMMENDATIONS

Analysis and experimental observations support the following conclusions regarding axially symmetric vertical penetration into a half space of particulate medium:

1. The Euler and Poncelet assumptions concerning the soil force resisting motion do not seem to be valid.
2. Equations can be written to describe the whole process of penetration. The experiments seem to validate those equations. The boundary and initial conditions for the problem can be delineated.
3. The process of penetration is primarily one of shear deformation of the soil when it is in a dense condition.
4. Approximations can be made for the velocity and deformation fields that will contribute to the solution of the various vertical penetration problems.

It is recommended that these studies should be extended in the following ways:

1. A numerical solution to the governing differential equations should be attempted using the "marker and cell" technique on a high speed computer.

2. The photo-plastic two dimensional studies should be extended, using more sophisticated equipment to evaluate the effects of boundary conditions.
3. Three dimensional laboratory studies should be continued using the instrumentation developed by Division 9226 of Sandia Corporation in order to study vertical penetration into real materials.
4. The constant velocity tests into steel needle bearing rollers were most helpful in reaching an understanding of the penetration process. This work should be continued using higher velocities, various penetration attitudes, different boundary conditions and possibly even with the use of a semi-flexible penetrator. The effect of cohesion could also be studied by filling the voids with a viscous cohesive material.

SELECTED BIBLIOGRAPHY

- Backman, M. E., and H. L. Morrison. The Fracture of Aggregates of Brittle Particles. U. S. Naval Ordnance Test Station, China Lake, California, NOTS TM No. 1582, November 1953.
- Casagrande, Arthur. "Characteristics of Cohesionless Soils Affecting the Stability of Slopes and Earth Fills," Contributions to Soil Mechanics: 1925-1940. Boston Society of Civil Engineers.
- _____, and S. D. Wilson. "Effect of Rate of Loading on the Strength of Clays and Shales at Constant Water Content," Geotechnique, II (1951).
- Cauchy, A. L. Ex. de Math 3 (1828), Oeuvres (2) 8, pp. 195-226.
- Colp, J. L. An Experimental Investigation of the Continuous Penetration of a Blunt Body Into a Simulated Cohesionless Soil. Sandia Corporation, Albuquerque, New Mexico, SC-RR-65-260.
- Drucker, D. C., and W. Prager. "Soil Mechanics and Plastic Limit Design," The Quarterly of Applied Mathematics, X (1952).
- Eskinazi, Salamon. Principles of Fluid Mechanics. Boston: Allyn and Bacon, Inc., 1962.
- Euler, L. Principes General due Movement des Fluids. Hist. Acad. Berlin, 1755, (opera omnia II, 12).
- Freudenthal, A. M. The Inelastic Behavior of Engineering Materials and Structures. New York: John Wiley & Sons, 1950.
- Goldsmith, Werner. Analytical Versions of Penetration Processes. NAVWEPS Report 7812, NOTS TP 2811, February 1962.
- Harlow, Francis H., and J. Eddie Welch. "Numerical Study of Large Amplitude Free Surface Motions." Paper submitted for publication in The Physics of Fluids.
- Healy, Kent A. Undrained Strength of Saturated Clayey Silt. M. I. T. Report No. 15, March 1963.

- Hendron, A. J., R. E. Fulton, and Bijan Mohraz. The Energy Absorption Capacity of Granular Materials in One-Dimensional Compression. Air Force Special Weapons Center, Kirtland Air Force Base, New Mexico, January 1963.
- Hultgren, R. O., L. J. Thompson, and D. G. Kitzinger. State of Stress in an Elastic Earth Target Resting on a Rigid Half-Space. Sandia Corporation, Albuquerque, New Mexico, Research Report SC-RR-64-1734, May 1965.
- Hvorslev, M. J. Discussion at Session II—Shallow Foundations, Symposium on Bearing Capacity and Settlement of Foundations. Duke University, April 1965.
- Jumikis, A. R. Mechanics of Soils. Princeton, N. J.: D. Van Nostrand Co., 1964.
- Kerisel, J. "Deep Foundations Basic Experimental Facts," Deep Foundations Conference. Mexico D. F., Mexico. December 1964.
- Meyerhof, G. G. "The Ultimate Bearing Capacity of Foundations," Geotechnique, II (1951).
- Mises, R. V. "Mechanik der Plastischen Formaenderung von Krestallen," Z. Angew. Math. Mech, VIII, (1928).
- Morrison, H. L., and W. A. Allen. Projectile Energy Expended in Commintion of the Target. U. S. Naval Ordnance Test Station, China Lake, California, NOTS 1181, NAVORD Report 4885, July 1955.
- Prager, William. Introduction to Mathematics of Continua. New York: Ginn and Company, 1961.
- Reiner, Markus. Deformation, Strain and Flow. London: H. K. Lewis & Co., Ltd., 1960.
- Robertson, H. P. Terminal Ballistics. National Research Council, 2101 Constitution Avenue, Washington, D. C. Committee on Passive Protection Against Bombing (January 1941).
- Roscoe, K. H., A. N. Schofield, and C. P. Wroth. "On the Yielding of Soils," Geotechnique, VIII (1958).

- Serrin, James. "Mathematical Principles of Classical Fluid Mechanics," Handbuch der Physik (Springer, Berlin), VIII (1959).
- Shield, R. T. "Mixed Boundary Value Problem in Soil Mechanics," The Quarterly of Applied Mathematics, X (1952).
- Sobotka, Zdenek. "The Slip Lines and Slip Surfaces in the Theory of Plasticity and Soil Mechanics," Applied Mechanics Reviews, XIV (1961).
- Sokolnikoff, J. S. Mathematical Theory of Elasticity. New York: McGraw-Hill Co., 1956.
- Taylor, Donald. Fundamentals of Soil Mechanics. New York: John Wiley & Sons, 1948.
- Terminal Ballistics and Explosive Effects. National Research Council, 2101 Constitution Avenue, Washington, D. C. Committee on Passive Protection Against Bombing. Vol. II, Appendix to Final Report (1943).
- Terzaghi, Karl. Theoretical Soil Mechanics. New York: John Wiley & Sons, 1943.
- Timoshenko, S., and J. N. Goodier. Theory of Elasticity. New York: McGraw-Hill Co., 1951.
- Whitman, Robert V., and Kent A. Healy. Shearing Resistance of Sands During Rapid Loading. M.I.T. Report No. 9, May 1962.
- Wu, T. H. Soil Mechanics. Boston: Allyn and Bacon, Inc., 1966.

DISTRIBUTION:

U. S. Atomic Energy Commission
 Director, Space Nuclear Systems
 Space Electric Power Office
 Washington, D. C. 20545
 Attn: G. P. Dix, Chief, Safety Branch

U. S. Atomic Energy Commission
 Director, Space Nuclear Systems
 Space Electric Power Office
 Washington, D. C. 20545
 Attn: R. S. Decker, Jr., Chief, Safety Branch

U. S. Atomic Energy Commission
 Director, Space Nuclear Systems
 Space Electric Power Office
 Washington, D. C. 20545
 Attn: W. A. Yingling

U. S. Atomic Energy Commission
 Director, Space Nuclear Systems
 Space Electric Power Office
 Washington, D. C. 20545
 Attn: R. T. Carpenter
 Chief, Isotope Power Systems Branch

U. S. Atomic Energy Commission
 Director, Space Nuclear Systems
 Space Electric Power Office
 Washington, D. C. 20545
 Attn: H. Specter
 Reactor Power Systems Branch

U. S. Atomic Energy Commission
 Space Nuclear Propulsion Office
 Albuquerque Extension
 Albuquerque Operations Office
 P. O. Box 5400
 Albuquerque, New Mexico
 Attn: H. P. Smith

U. S. Atomic Energy Commission
 Division of Isotope Development
 Washington, D. C. 20545
 Attn: W. K. Kern

U. S. Atomic Energy Commission
 Division of Safety Standards (Beth 010)
 Washington, D. C. 20545
 Attn: J. J. Dinunno
 Assistant Director, Reactors

U. S. Atomic Energy Commission
 Division of Biology and Medicine
 Washington, D. C. 20545
 Attn: J. Z. Holland, Chief
 Fallout Studies Branch

U. S. Atomic Energy Commission
 Division of Biology and Medicine
 Washington, D. C. 20545
 Attn: Dr. Roger McClellan
 Medical and Health Research

U. S. Atomic Energy Commission
 Division of Biology and Medicine
 Washington, D. C. 20545
 Attn: H. D. Bruner, Asst. Director
 Medical and Health Research

U. S. Atomic Energy Commission (3)
 Division of Technical Information
 Headquarters Library G-017
 Washington, D. C. 20545

U. S. Atomic Energy Commission
 Albuquerque Operations Office
 P. O. Box 5400
 Albuquerque, New Mexico 87115
 Attn: S. A. Upson, Director
 Research and Classification Division

U. S. Atomic Energy Commission
 Albuquerque Operations Office
 P. O. Box 5400
 Albuquerque, New Mexico
 Attn: V. C. Vespe, Director
 Operational Safety Division

U. S. Atomic Energy Commission
 Canoga Park Area Office
 P. O. Box 591
 Canoga Park, California
 Attn: C. R. Malmstrom

U. S. Atomic Energy Commission
 Chicago Operations Office
 9800 South Cass Avenue
 Argonne, Illinois 60439
 Attn: Chief, Office Services Branch

U. S. Atomic Energy Commission
 Oak Ridge Operations Office
 Mail and Document Accountability Section
 P. O. Box E
 Oak Ridge, Tennessee 37831
 Attn: Director, Research and Development Division

Headquarters
 Air Force Systems Command (SCIZN)
 Washington, D. C. 20331
 Attn: Nuclear Safety Branch

Air Force Weapons Laboratory
 Kirtland Air Force Base, New Mexico
 Attn: Lt. Col. H. L. Harris (WLAS)

Air University Library
 Maxwell Air Force Base, Alabama
 Attn: Elizabeth C. Pittman

Atomics International (2)
 P. O. Box 309
 Canoga Park, California 91304
 Attn: R. L. Detterman

DISTRIBUTION (cont)

Battelle Memorial Institute
505 King Avenue
Columbus, Ohio 43201
Attn: J. E. Davis, Projects Administrator

Battelle Memorial Institute
Pacific Northwest Laboratory
P. O. Box 999
Richland, Washington 99352
Attn: E. A. Coppinger

Battelle Memorial Institute
Pacific Northwest Laboratory
P. O. Box 999
Richland, Washington 99352
Attn: Dr. Roy Thompson

Battelle Memorial Institute
Pacific Northwest Laboratory,
P. O. Box 999
Richland, Washington 99352
Attn: M. T. Walling

The Boeing Company
Aerospace Group
P. O. Box 3707
Seattle, Washington 98124
Attn: T. L. Smith, Mail Stop 23-82

Brookhaven National Laboratory
Technical Information Division
Upton, Long Island, New York 11973
Attn: Research Library

Director, Defense Atomic Support Agency
P. O. Box 2610
Washington, D. C. 20301
Attn: Document Library Branch

Douglas Aircraft Company, Inc.
Missile and Space Systems Division
3000 Ocean Park Boulevard
Santa Monica, California
Attn: Sig Gronich
Advanced Space Technology

E. I. Du Pont De Nemours and Company
Savannah River Laboratory
Aiken, South Carolina 29802
Attn: W. B. Scott, Document Division

General Atomic Division
General Dynamics Corporation
P. O. Box 608
San Diego, California 92112
Attn: Library

General Electric Company
Nuclear Materials and Propulsion Operation
P. O. Box 15132
Cincinnati, Ohio 45215
Attn: J. W. Stephenson
For: W. Briskin

General Electric Company
Valley Forge Space Technology Center
P. O. Box 8555
Philadelphia, Pennsylvania 19101
Attn: S. M. Scala, Room M9539
Space Sciences Laboratory

General Electric Company
Valley Forge Space Technology Center
P. O. Box 8555
Philadelphia, Pennsylvania 19101
Attn: Carl Gamertsfelder
Advanced Requirements Planning Dept.

General Electric Company
570 Lexington Avenue
New York, New York 10022
Attn: Richard W. Porter, Consultant
Aerospace Science and Technology

Hittman Associates, Inc.
P. O. Box 2685
4715 East Wabash Avenue
Baltimore, Maryland, 21215

Deputy I. G. for Insp. and Safety, USAF
Kirtland Air Force Base, New Mexico
87117
Attn: Col. D. C. Jameson (AFINSR)

Deputy I. G. for Insp. and Safety, USAF
Kirtland Air Force Base, New Mexico
87117
Attn: Lt. Col. G. H. Ogburn (AFINSR)

Institute for Defense Analyses
400 Army Navy Drive
Arlington, Virginia 22200
Attn: Richard Briceland

Lockheed Missiles and Space Company
P. O. Box 504
Sunnyvale, California
Attn: H. H. Greenfield, Manager
Nuclear Power Development

Lockheed Missiles and Space Company
P. O. Box 504
Sunnyvale, California
Attn: R. F. Hausman (Dept. 30-63)
Cryogenic and Nuclear Stage Programs

Lockheed Missiles and Space Company
P. O. Box 504
Sunnyvale, California
Attn: Harold F. Plank

Los Alamos Scientific Laboratory
P. O. Box 1663
Los Alamos, New Mexico 87544
Attn: Dr. L. D. P. King

DISTRIBUTION (cont)

Los Alamos Scientific Laboratory
P. O. Box 1663
Los Alamos, New Mexico 87544
Attn: Dr. Wright Langham

Lovelace Foundation for Medical Education
and Research
5200 Gibson Blvd., SE
Albuquerque, New Mexico
Attn: Dr. C. S. White, President-Director

Martin Company
Nuclear Programs
Middle River, Maryland 21203
Attn: D. G. Harvey, Mail No. 801

Minnesota Mining and Manufacturing Co.
2501 Hudson Road, Maplewood
St. Paul, Minnesota 55119
Attn: J. P. Ryan, TCAAP 675
Nuclear Products Department

Monsanto Research Corporation
Mound Laboratory
P. O. Box 32
Miamisburg, Ohio 45342
Attn: G. R. Grove

Administrator
National Aeronautics and Space Administration
Washington, D. C. 20545
Attn: T. B. Kerr (RNS)

National Aeronautics and Space Administration
Ames Research Center
Moffet Field, California
Attn: Glenn Goodwin

National Aeronautics and Space Administration
Goddard Space Flight Center
Glenn Dale Road
Greenbelt, Maryland 20771
Attn: A. W. Fihelly, Nimbus Project

National Aeronautics and Space Administration
Lewis Research Center
21000 Brookpark Road
Cleveland, Ohio 44135
Attn: Library

National Aeronautics and Space Administration
Manned Spacecraft Center
Houston, Texas 77058
Attn: Technical Information Dissemination
Branch (Code BM6)

National Aeronautics and Space Administration (2)
Scientific and Technical Information Facility
P. O. Box 33
College Park, Maryland 20740
Attn: Acquisitions Branch (S-AK/DL)

NUS Corporation
Environmental Safeguards Division
Suite 1100
1730 M Street, N. W.
Washington, D. C. 20036
Attn: M. S. Goldman, Vice President

Phillips Petroleum Company
NRTS Technical Library
P. O. Box 2067
Idaho Falls, Idaho 83401

Radio Corporation of America
Astro Electronics Division
P. O. Box 800
Princeton, New Jersey 08540
Attn: S. H. Winkler
Ldr. Adv. Power

Director, USAF Project RAND
via Air Force Liaison Office
The Rand Corporation
1700 Main Street
Santa Monica, California 90406
Attn: Library

Space Nuclear Propulsion Office
Lewis Research Center
21000 Brookpark Road
Cleveland, Ohio 44135
Attn: L. Nichols

TRW Systems
P. O. Box 287
Redondo Beach, California 9027
Attn: Dr. Donald Jortner

U. S. Naval Radiological Defense Laboratory
Commanding Officer and Director
San Francisco, California 94135
Attn: P. E. Zigman

Union Carbide Corporation (2)
Nuclear Division
P. O. Box X
Oak Ridge, Tennessee 37831
Attn: R. A. Robinson, Isotope Dev. Center

Union Carbide Research Institute
P. O. Box 278
Tarrytown, New York
Attn: Joseph Agresta
Space Sciences Group

University of California
Lawrence Radiation Laboratory
P. O. Box 808
Livermore, California 94551
Attn: Dr. James Hadley
Chief, R. Division

DISTRIBUTION (cont)

University of California
Lawrence Radiation Laboratory
P. O. Box 808
Livermore, California 94551
Attn: Technical Information Division

Westinghouse Electric Company
Astronuclear Laboratory
P. O. Box 10864
Pittsburgh 30, Pennsylvania
Attn: Joanne M. Bridges, Supervisor
Flight Safety Analysis Group

Division of Technical Information Ext. (70)
U. S. Atomic Energy Commission
P. O. Box 62
Oak Ridge, Tennessee 37831

Clearinghouse for Federal Scientific and
Technical Information (75)
5285 Port Royal Road
Springfield, Virginia 22151

R. L. McNeill
Woodward-Clyde-Sherard & Associates
Oakland, California

F. J. Benson, Dean of Engineering
Texas A & M University
College Station, Texas

Dr. H. G. Larew
Department of Civil Engineering
University of Virginia
Charlottesville, Virginia

R. W. Cunny
U. S. Waterways Experimental Station
Vicksburg, Mississippi

C. R. White
U. S. Navy Civil Engineering Laboratory
Port Hueneme, California

Don A. Linger
University of Arizona
Tucson, Arizona

Ralph Peck
Civil Engineering Department
University of Illinois
Urbana, Illinois

Frank Richart, Head, Civil Engineering Department
University of Michigan
Ann Arbor, Michigan

G. A. Leonards
Civil Engineering Department
Purdue University
Lafayette, Indiana

G. A. Young, Head, Department of Civil Engineering
Michigan College of Mining & Technology
Houghton, Michigan

R. V. Whitman
Massachusetts Institute of Technology
Cambridge, Massachusetts

C. E. Stoneking
Georgia Institute of Technology
Atlanta, Georgia

N. M. Newmark, Head, Civil Engineering Department
University of Illinois
Urbana, Illinois

A. S. Vesic
Civil Engineering Department
Duke University
Durham, North Carolina

M. J. Hvorslev
U. S. Waterways Experimental Station
Vicksburg, Mississippi

L. J. Thompson
Texas A & M University
College Station, Texas (10)

Harry Seed
Department of Civil Engineering
University of California
Berkeley, California

Major John P. Thomas, Deputy Director
Civil Engineering Branch
USAF, AFSWC
Kirtland AFB, New Mexico

S. P. Schwartz, 1
W. J. Howard, 1000
L. A. Hopkins, 1300
J. H. Findlay, 1400
S. A. Moore, 1540
R. J. Hansen, 4200
R. S. Claassen, 5100
J. R. Banister, 5120
T. B. Cook, 5200
J. D. Shreve, 5234
J. H. Scott, 5610, Attn: D. E. Henry, 5613
R. G. Clem, 5630
W. T. Moffat, 7220
H. E. Viney, 7250
L. E. Lamkin, 7300
G. H. Roth, 7320
G. A. Fowler, 9000
D. B. Shuster, 9200
M. L. Kramm, 9220, Attn: V. K. Smith, 9226
A. E. Bentz, 9232
A. Y. Pope, 9300
V. E. Blake, 9310

DISTRIBUTION (cont)

H. E. Hansen, 9311 (3)
S. L. Jeffers, 9312
S. McAlees, 9314
R. J. Everett, 9315
J. D. Appel, 9319
R. C. Maydew, 9320
H. R. Vaughn, 9321
W. H. Curry, 9322
E. C. Rightley, 9323
W. R. Barton, 9324
J. K. Cole, 9325
K. J. Touryan, 9326
W. N. Caudle, 9327 (5)
W. N. Caudle, 9327, Attn: J. Colp
A. J. Clark, 9330
J. W. McKiernan, 9331
J. L. Tischhauser, 9420
B. S. Biggs, 8000
B. F. Hefley, 8232
T. B. Heaphy, 3411
R. S. Gillespie, 3413 (4)
B. R. Allen, 3421
B. W. Scott, 3428-1 (Acting)
C. Sproul, 3415-3 (10)